



저작자표시-비영리-변경금지 2.0 대한민국

이용자는 아래의 조건을 따르는 경우에 한하여 자유롭게

- 이 저작물을 복제, 배포, 전송, 전시, 공연 및 방송할 수 있습니다.

다음과 같은 조건을 따라야 합니다:



저작자표시. 귀하는 원 저작자를 표시하여야 합니다.



비영리. 귀하는 이 저작물을 영리 목적으로 이용할 수 없습니다.



변경금지. 귀하는 이 저작물을 개작, 변형 또는 가공할 수 없습니다.

- 귀하는, 이 저작물의 재이용이나 배포의 경우, 이 저작물에 적용된 이용허락조건을 명확하게 나타내어야 합니다.
- 저작권자로부터 별도의 허가를 받으면 이러한 조건들은 적용되지 않습니다.

저작권법에 따른 이용자의 권리와 책임은 위의 내용에 의하여 영향을 받지 않습니다.

이것은 [이용허락규약\(Legal Code\)](#)을 이해하기 쉽게 요약한 것입니다.

[Disclaimer](#)



공학박사학위논문

**A study on the nonlinear stress of
complex fluids under large amplitude oscillatory
shear (LAOS) flow in the perspective of
symmetry and energy**

대칭성과 에너지 관점에서 본 대변형 진동 전단
(LAOS) 유동 조건에서의 복잡유체의 비선형
응력에 관한 연구

2018년 2월

서울대학교 대학원

화학생물공학부

박 찬 형

Abstract

A study on the nonlinear stress of complex fluids
under large amplitude oscillatory shear (LAOS) flow
in the perspective of symmetry and energy

Chan Hyung Park

School of Chemical and Biological Engineering

The Graduate School

Seoul National University

Large amplitude oscillatory shear (LAOS) test is widely applied to characterize complex fluids. Various analysis methods for LAOS stress in time domain or strain and strain rate domain had been suggested. However, their interpretation or physical meaning was not fully understood. For example, one of the analysis methods, stress decomposition, is under disputes due to the discordance in stress profile and structural characteristics. One of the purposes of this thesis is to explore the proper interpretation of stress decomposition analysis.

Stress decomposition is an analysis method that decomposes total oscillatory stress into elastic and viscous stress by using mathematical symmetry of oscillation. In this thesis, stress decomposition is applied to oscillatory stress, which is calculated by Brownian dynamics (BD) simulation for both hard and soft sphere systems. Double peaks, which are experimentally observed only in the elastic stress of hard sphere systems, are observed only in the hard sphere systems in accordance with experiments.

To find out the structural origin of double peaks, the structure of the particulate system is analyzed in terms of the softness of the particles and strain amplitude, which determine the presence of double peaks. In hard and soft sphere comparison, there is a significant difference in structure between two systems. However, the structures do not have the one-to-one match with the elastic stresses for hard spheres. The intensive investigation leads to the conclusion that it is necessary to consider the structures and the elastic stress in the whole cycle rather than them at each time step. We also suggest structural characteristics which make double peaks in the simulation.

The other purpose of this thesis is to suggest a new method for analyzing oscillatory shear stress. To achieve this goal, the concept of work and stored energy, which has rarely been considered in the past, is adopted. The inner area in the strain-stress Lissajous curve throughout one cycle is known to be related to work or viscous characteristic of the material, and that of the strain rate-stress Lissajous with stored energy or elastic characteristic of the

material. These relationships also work on nonlinear stress, and only areas throughout one full cycle are spotlighted until now.

However, to precisely analyze the nonlinear stress, it helps to consider work and energy not only throughout a complete cycle but also during the cycle. We trace the work and energy during the oscillation. Firstly, we apply this concept to perfectly elastic solid and purely viscous liquid with different rheological behaviors. They are classified by tracing work and energy variation in the subdivided sections. This concept is also applied to viscoelastic fluid and Bingham fluid. The symmetry of work and energy with respect to flow reversal point disappears in these fluids, which leads to the conclusion that the extent of asymmetry needs to be considered. The oscillatory stress from Brownian dynamics simulation is also analyzed. Work is correlated to rheological property, oscillatory stress, and particle structure in this analysis. By these approaches, the possibility is shown that the systems with different rheological properties can be characterized by work or energy during the cycle.

This thesis provides a new insight on the analysis of nonlinear oscillatory shear stress. This study is expected to provide an extendable framework for further understanding of the nonlinear oscillatory shear stress in the perspective of symmetry and energy.

Keywords: large amplitude oscillatory shear (LAOS), hard sphere, soft sphere, Brownian dynamics (BD) simulation, stress decomposition, work, stored energy

Student Number: 2010-20993

Contents

Abstract.....	i
List of Figures.....	ix
I . Introduction.....	1
1.1 Small amplitude oscillatory shear (SAOS) flow.....	1
1.2 Large amplitude oscillatory shear (LAOS) flow.....	2
1.2.1 Basic mathematical description for LAOS.....	3
1.2.2 Analysis method for LAOS.....	5
1.3 Complex fluids.....	9
1.3.1 Particle suspension systems.....	9
1.4 Outline of the thesis.....	11
II. Backgrounds.....	13
2.1 Brownian dynamics (BD) simulation.....	13
2.1.1 General description of BD.....	13

2.1.2 Application of BD.....	16
2.2 Simulation systems.....	18
III . Stress decomposition analysis in hard and soft sphere suspensions.....	20
3.1 Motivation and objectives.....	20
3.2 Analysis of hard and soft sphere systems.....	22
3.2.1 Strain sweep.....	22
3.2.2. Lissajous curve.....	24
3.2.3 Fourier transform (FT).....	28
3.3 Stress decomposition and double peaks.....	30
3.3.1 Total, elastic, and viscous shear stresses of hard and soft spheres.....	30
3.3.2 Double peaks characteristics.....	34
3.4 Stress and structural analysis.....	38
3.4.1 Soft and hard spheres.....	38
3.4.2 Hard sphere at different strain amplitude.....	48
3.5 Conclusions	56

Appendix 3A.....	58
Appendix 3B.....	62
IV. Path-dependent work and stored energy in LAOS flow.....	64
4.1 Motivation and objectives.....	64
4.2 Work and stored energy under oscillatory shear.....	65
4.3 Work and stored energy of model stress.....	68
4.4 Application to constitutive equations.....	74
4.4.1 Purely viscous liquid and perfectly elastic solid.....	74
4.4.2 Giesekus model.....	80
4.4.3 Bingham model.....	88
4.5 Application to BD simulation.....	94
4.6 Conclusions.....	102
Appendix 4A.....	104
V. Conclusions	107
Bibliography.....	110

국문 초록.....	119
------------	-----

List of Figures

Fig. 3-1 G' and G'' of soft hard sphere systems as a function of γ_0 at $\Gamma/\Gamma_{freezing} = 0.61$ and $De = 80$. G' and G'' are normalized by G'_0 at each system.	23
Fig. 3-2 $x - \sigma$ Lissajous curves of a) soft, b) hard sphere systems at $\Gamma/\Gamma_{freezing} = 0.61$. Each trajectory is positioned in a Pipkin space according to the imposed values of γ_0 and De	26
Fig. 3-3 $y - \sigma$ Lissajous curves of a) soft, b) hard sphere systems at $\Gamma/\Gamma_{freezing} = 0.61$. Each trajectory is positioned in a Pipkin space according to the imposed values of γ_0 and De	27
Fig. 3-4 I_3/I_1 of a) soft, b) hard sphere systems as a function of γ_0 at $De = 50, 80$, and 100	29
Fig. 3-5 a) The total, elastic, and viscous stresses at $De = 80$; b) elastic stresses from $De = 20$ to 100 for PF at $\Gamma/\Gamma_{freezing} = 0.61$	31

Fig. 3-6 The total, elastic, and viscous stresses for a) $n = 8$ (soft sphere), b) $n = 54$ (quasi-hard sphere) for IPP method, at $\Gamma/\Gamma_{freezing} = 0.61$ and $De = 80$33

Fig. 3-7 The definition of depth and width when double peaks appear. The elastic stress is plotted at $\Gamma/\Gamma_{freezing} = 0.61$, $De = 80$, and $\gamma_0 = 3$34

Fig. 3-8 Double peaks a) depth and b) width at $De = 50, 80$, and 100 as a function of γ_0 for PF and IPP with $n = 54$ at $\Gamma/\Gamma_{freezing} = 0.61$36

Fig. 3-9 The total and elastic stresses of soft sphere (S, IPP; $n = 8$) and hard sphere (H, PF) systems when $\Gamma/\Gamma_{freezing} = 0.61$, $De = 80$, and $\gamma_0 = 3$39

Fig. 3-10 PDF of a) point A of soft sphere, b) point A of hard sphere, c) point B of soft sphere, and d) point B of hard sphere.41

Fig. 3-11 RDF at points A and B for hard sphere (H, PF) and soft sphere (S, IPP; $n = 8$) systems.43

Fig. 3-12 The location of the first peak in RDF during a half cycle in both soft (S, IPP; $n = 8$) and hard sphere (H, PF) systems. 44

Fig. 3-13 Total (solid line) and elastic stresses (dashed line) at a) $\gamma_0 = 0.8$ and 1 and b) $\gamma_0 = 5$ and 8. Double peaks are not observed at $\gamma_0 = 0.8$ and 8, but double peaks are observed at $\gamma_0 = 1$ and 5. 49

Fig. 3-14 PDF for a) $\gamma_0 = 0.8$, point C, b) $\gamma_0 = 1$, point C, c) $\gamma_0 = 0.8$, point D, d) $\gamma_0 = 1$, point D, e) $\gamma_0 = 5$, point E, f) $\gamma_0 = 8$, point E, g) $\gamma_0 = 5$, point F, h) $\gamma_0 = 8$, point F. 51

Fig. 3-15 Normalized total stress (solid line) and excess entropy (dashed line) during half cycle at a) $\gamma_0 = 0.8$ and 1 and b) $\gamma_0 = 5$ and 8. 53

Fig. 3-16 The difference in the maximum and minimum of excess entropy as a function of γ_0 55

Fig. 3A-1 Normalized total stress with time in Pipkin space for a) soft and b) hard sphere systems at $\Gamma/\Gamma_{freezing} = 0.61$ 59

Fig. 3A-2 Normalized elastic stress with time in Pipkin space for a) soft and b) hard sphere systems at $\Gamma/\Gamma_{freezing} = 0.61$ 60

Fig. 3A-3 Normalized viscous stress with time in Pipkin space for a) soft and b) hard sphere systems at $\Gamma/\Gamma_{freezing} = 0.61$ 61

Fig. 3B-1 The difference in the maximum and minimum of excess entropy as a function of γ_0 at $\Gamma/\Gamma_{freezing} = 0.61, 0.71$ and 0.81 62

Fig. 3B-2 Double peaks a) depth and b) width at $De = 80$ as a function of γ_0 for PF at $\Gamma/\Gamma_{freezing} = 0.61, 0.71$ and 0.81 63

Fig. 4-1 The shape change of $x(\gamma) - \sigma$ and $y(\dot{\gamma}/\omega) - \sigma$ Lissajous with varying δ_3 in Eq. (4-5). 68

Fig. 4-2 Areas of a) $x(\gamma) - \sigma$ Lissajous, b) $y(\dot{\gamma}/\omega) - \sigma$ Lissajous vs. time as δ_3 changes. 71

Fig. 4-3 Areas of a) $x(\gamma) - \sigma$ Lissajous, b) $y(\dot{\gamma}/\omega) - \sigma$ Lissajous vs. time as k changes.73

Fig. 4-4 Normalized W at each section in half cycle for a) shear thickening, b) shear thinning liquid. n in the horizontal axis means the time interval $(n-1)/24$ cycle $< t/(2\pi/\omega) < n/24$ cycle.77

Fig. 4-5 Normalized E at each section in half cycle for a) strain stiffening, b) strain softening solid. n in the horizontal axis means the time interval $(n-1)/24$ cycle $< t/(2\pi/\omega) < n/24$ cycle.79

Fig. 4-6 a) Normalized W , b) normalized E at $\omega=1$. n in the horizontal axis means the time interval $(n-1)/24$ cycle $< t/(2\pi/\omega) < n/24$ cycle.81

Fig. 4-7 a) Normalized W , b) normalized E at $\gamma_0=0.01$, which is included in the linear region. n in the horizontal axis means the time interval $(n-1)/24$ cycle $< t/(2\pi/\omega) < n/24$ cycle.83

Fig. 4-8 a) W_{FR}/W_{full} , b) E_{FR}/E_{full} as a function of γ_0 at three ω85

Fig. 4-9 a) $x(\gamma) - \sigma$, b) $y(\dot{\gamma}/\omega) - \sigma$ Lissajous plot of Bingham model as a function of γ_0 .	89
Fig. 4-10 a) W/W_{full} , b) E/E_{full} of Bingham model as time proceeds.	.91
Fig. 4-11 Normalized W and E in the elastic and viscous σ parts as a function of γ_0 .	93
Fig. 4-12 Strain sweep results of a) $De = 20$, b) $De = 80$ for PF at $\Gamma/\Gamma_{freezing} = 0.61$. When $De = 20$, strain thinning is shown, and when $De = 80$ weak strain overshoot is shown.	95
Fig. 4-13 Normalized a) W_{A1} , W_{B1} , and W_{FR} by W_{full} at $De = 20$, b) W_{A1} , W_{B1} , and W_{FR} by W_{full} at $De = 80$ as a function of γ_0 for PF at $\Gamma/\Gamma_{freezing} = 0.61$.	97
Fig. 4-14 Normalized a) W_{B2} , W_{A2} , and $W_{A2} + W_{B2}$ at $De = 20$, d) W_{B2} , W_{A2} , and $W_{A2} + W_{B2}$ by W_{full} at $De = 80$ as a function of γ_0 for PF at $\Gamma/\Gamma_{freezing} = 0.61$.	98

Fig. 4-15 $x - \sigma$ Lissajous curves for PF at $De = 20$ and 80 , $\Gamma/\Gamma_{freezing} = 0.61$. The red section indicates section A1.99

Fig. 4-16 The normalized average excess entropy as a function of γ_0 for PF at $De = 20$ and 80 , $\Gamma/\Gamma_{freezing} = 0.61$101

I . Introduction

1.1 Small amplitude oscillatory shear (SAOS) flow

When materials undergo a flow with small strain and strain rate, they show linear stress response which means that rheological property of materials can be evaluated by a single value (viscosity or elastic modulus). This linear response is also observed in stress under small amplitude oscillatory shear (SAOS) flow. Strain and strain rate can be defined as Eq. (1-1) and (1-2) respectively, in the oscillatory shear flow

$$\gamma(t) = \gamma_0 \sin(\omega t) \quad (1-1)$$

$$\dot{\gamma}(t) = \gamma_0 \omega \cos(\omega t) \quad (1-2)$$

where γ_0 , ω , and t are strain amplitude, frequency and time, respectively. For a perfectly elastic material, stress has the same phase with strain, whereas, for a purely viscous material, stress has the same phase with strain rate. Thus, generally, an oscillatory shear stress of the viscoelastic material is expressed as Eq. (1.3),

$$\begin{aligned} \tau(t) &= \tau_0 \cos \delta \sin(\omega t) + \tau_0 \sin \delta \cos(\omega t) \\ &= G' \gamma_0 \sin(\omega t) + G'' \gamma_0 \cos(\omega t) \end{aligned} \quad (1-3)$$

where τ_0 , δ , G' , and G'' are stress amplitude, phase angle ($0 \leq \delta \leq \pi/2$), storage modulus (elastic modulus), and loss modulus (viscous modulus),

respectively. As storage and loss moduli are calculated under the assumption that stress response is linear, these moduli are called as linear viscoelastic properties [Bird *et al.* (1987)]. These linear viscoelastic properties allow the extent of elastic or viscous characteristics in various material systems to be evaluated.

Small amplitude oscillatory shear (SAOS) test is widely used due to its advantages. It is non-destructive technique, which means that structural breakage is prevented after measuring. γ_0 and ω (time scale) can be varied independently in this flow [Dealy and Wissbrun (1990)]. The sudden change of the displacement or speed is not required because the strain is varied smoothly [Giacomin and Dealy (1993)].

However, in the real processes, flow and deformation are large and rheological properties are varied from the linear regime to the this nonlinear regime. Under large amplitude oscillatory shear (LAOS) flow, oscillatory shear stress is no longer sinusoidal shaped and has high harmonic contributions.

1.2 Large amplitude oscillatory shear (LAOS) flow

LAOS test also shares advantages of SAOS test except for non-destructive technique. And materials can be classified according to the shape of G' and G'' under LAOS from both experiment and simulation studies [Hyun *et al.* (2002), Sim *et al.* (2003)]. It implies that rheological and structural differences

of various materials, which are concealed in SAOS test, can be observed in LAOS test. Though it is not easy to deal with nonlinear behaviors, it is necessary to focus on stress and rheological properties under LAOS regime to fully understand behaviors and structures of materials.

1.2.1 Basic mathematical description for LAOS

Oscillatory shear stress in the nonlinear regime can be expanded by a polynomial or Taylor expansion with respect to the strain and strain rate as Eq. (1-4),

$$\sigma = \sum_{i=0} \sum_{j=0} C_{ij} \gamma^i(t) \dot{\gamma}^j(t) \quad (1-4)$$

where C_{ij} are mathematical constants for the expansion of nonlinear stress and are related to material functions. By using symmetric characteristics of oscillatory shear stress and putting Eq. (1-1) and Eq. (1-2) into Eq. (1-4), Eq. (1-5) is obtained,

$$\sigma = \sum_{p,odd} \sum_{q,odd}^p \gamma_0^q \left[a_{pq} \sin q\omega t + b_{pq} \cos q\omega t \right] \quad (1-5)$$

where a_{pq} and b_{pq} are also related to material functions. Thus, under LAOS flow, total oscillatory shear stress can be expressed by the sum of odd harmonics with phase angles as described in Eq. (1-6) [Wilhelm (2002)].

$$\begin{aligned}\sigma &= \sum_{n=1, odd}^{\infty} \sigma_n \sin(n\omega t + \delta_n) \\ &= \sum_{n=1, odd}^{\infty} \sigma_n (\sin n\omega t \cos \delta_n + \cos n\omega t \sin \delta_n)\end{aligned}\quad (1-6)$$

where σ_n indicates the intensity of n^{th} harmonic and δ_n means n^{th} phase angle. This equation can be expressed differently as in Eq. (1-7), which is similar to Eq. (1-5), with respect to γ_0 [Pearson and Rochfort (1982)].

$$\begin{aligned}\sigma &= \gamma_0 \left[G'_1 \sin \omega t + G''_1 \cos \omega t \right] + \\ &\quad \gamma_0^3 \left[G'_{31} \sin \omega t + G''_{31} \cos \omega t + G'_{33} \sin 3\omega t + G''_{33} \cos 3\omega t \right] \\ &\quad + O(\gamma_0^5) + \dots\end{aligned}\quad (1-7)$$

Trigonometric terms with fundamental frequency (ω) in Eq. (1-7) are defined as the first harmonics and they are expressed as follows:

$$\begin{aligned}1^{\text{st}} \text{ harmonic} &= \left[G'_{11} \gamma_0 + G'_{31} \gamma_0^3 + O(\gamma_0^5) + \dots \right] \sin \omega t + \\ &\quad \left[G''_{11} \gamma_0 + G''_{31} \gamma_0^3 + O(\gamma_0^5) + \dots \right] \cos \omega t \\ &= \gamma_0 \left[G'_1 \sin \omega t + G''_1 \cos \omega t \right]\end{aligned}\quad (1-8)$$

where $G'_{11}(\omega)$, $G'_{31}(\omega)$, $G''_{11}(\omega)$, and $G''_{31}(\omega)$ are the nonlinear coefficient from power series, and G'_1 and G''_1 are the first harmonic moduli. Similar to equation Eq. (1-8), odd harmonics of higher order can be arranged, and these terms are defined as higher harmonics.

1.2.2 Analysis method for LAOS

To exactly analyze nonlinear stress, it is necessary to consider not only the first harmonic, which corresponds to fundamental frequency but also higher harmonics contributions. When considering only G'_1 and G''_1 from the fundamental frequency, the stress is easy to handle but fruitful results embedded in nonlinear stress cannot be utilized because higher harmonics are neglected. On the other hand, when higher harmonics are included, it is not easy to consider all the harmonics in oscillatory shear stress because it is mathematically complicated.

Several methods have been developed to analyze nonlinear oscillatory shear stress [Hyun *et al.* (2011)]. One approach is to analyze stress in strain or strain rate domain, and the other in a time domain. Stress decomposition is a well-known method that analyzes oscillatory shear stress in strain or strain rate domain [Cho *et al.* (2005)]. If strain and strain rate are defined as $x = \gamma = \gamma_0 \sin \omega t$ and $y = \dot{\gamma}/\omega = \gamma_0 \cos \omega t$, respectively, then,

$$\begin{aligned}\sigma(x, y) &= \frac{\sigma(x, y) + \sigma(x, -y)}{2} + \frac{\sigma(x, y) + \sigma(-x, y)}{2} \\ &= \sigma_e(x, y) + \sigma_v(x, y)\end{aligned}\quad (1-9)$$

where σ_e indicates the elastic stress and σ_v the viscous stress. This method can be expanded by using the Chebyshev polynomial [Ewoldt *et al.* (2008)],

$$\sigma_e(x) = \gamma_0 \sum_{n=odd} e_n(\omega, \gamma_0) T_n(x) \quad (1-10)$$

$$\sigma_v(y) = \dot{\gamma}_0 \sum_{n=odd} v_n(\omega, \gamma_0) T_n(y) \quad (1-11)$$

where $e_n(\omega, \gamma_0)$, $v_n(\omega, \gamma_0)$, and T_n refer elastic Chebyshev coefficients, viscous Chebyshev coefficients, and n^{th} order Chebyshev polynomial, respectively. The properties of the system can also be predicted by checking the convexity of elastic or viscous stress [Ewoldt and Bharadwaj (2013)]. Stress analysis in the strain or strain rate domain makes it easier to obtain parameters with physical meaning than that in the time domain.

It is controversial on the validity of stress decomposition method, in which there is no direct relationship between elastic/viscous stress and structure formation [Rogers and Lettinga (2012), Poulos *et al.* (2013)]. Contradicting results were also reported between the rheological properties obtained from the total stress and that from the stress at each time step [Mermet-Guyenet *et al.* (2015)]. Even though these disputes, there are many studies on the nonlinear stress of various systems using elastic/viscous stress and the coefficients of Chebyshev polynomial [Ahirwal *et al.* (2014), Salehiyan *et al.* (2015), Ptaszek (2015), Lee *et al.* (2015), Lee *et al.* (2015), Park *et al.* (2015), Khandavalli *et al.* (2016), Huang *et al.* (2017), Goudoulas and Germann (2017)]. These studies indicate that stress decomposition is still useful for analyzing oscillatory shear stress and that the meaning and limitation of this method need to be explored. In chapter III, we focus on results from stress decomposition and suggest the interpretation of this analysis.

Different from stress decomposition, Fourier transform (FT) is a well-known

method to transform oscillatory shear stress in a time domain to frequency domain [Wilhelm *et al.* (1998), Wilhelm *et al.* (1999), Wilhelm (2002)]. In this method, the ratio of the higher harmonic intensity against first harmonic, I_n/I_1 , is obtained as a function of strain amplitude γ_0 and is used to evaluate the degree of nonlinearity. In Eq. (1-12), I_3/I_1 is calculated by using Eq. (1-7).

$$\begin{aligned} \frac{I_3}{I_1} &= \frac{\sqrt{\left(G_{33}'\gamma_0^3 + G_{53}'\gamma_0^5 + \dots\right)^2 + \left(G_{33}''\gamma_0^3 + G_{53}''\gamma_0^5 + \dots\right)^2}}{\sqrt{\left(G_{11}'\gamma_0 + G_{31}'\gamma_0 + \dots\right)^2 + \left(G_{11}''\gamma_0 + G_{31}''\gamma_0 + \dots\right)^2}} \\ &= \frac{\sqrt{G_{33}'^2 + G_{33}''^2 + O(\gamma_0^2)\dots}}{\sqrt{G_{11}'^2 + G_{11}''^2 + O(\gamma_0^2)\dots}} \times \gamma_0^2 \end{aligned} \quad (1-12)$$

It is known that I_3/I_1 , the ratio of the third harmonic against the first harmonic, shows the relationship $I_3/I_1 \sim \gamma_0^2$ at small γ_0 [Neidhöfer *et al.* (2003)]. In addition, Q parameter, which is defined as $(I_3/I_1)/\gamma_0^2$, is known to reflect the structural characteristics of the branched polymer very well [Hyun and Wilhelm (2009)]. When conducting FT, not only intensity but also phase angle of each harmonic can be obtained. The change in third phase angle can be related to the change in stress shape [Wilhelm (2002), Hyun *et al.* (2003), Hyun *et al.* (2006)] and the third phase angle or the sign of Chebyshev coefficient can be used to classify the material system [Ewoldt *et al.* (2008)]. Though FT is useful as a data processing protocol, it simply decomposes stress signal, and the parameters do not have any physical significance in principle. They (analysis in a time domain/strain or strain rate domain) can be used complementarily, and it is recommended that both

methods to be applied to analyze nonlinear stress properly.

Another analysis method is relating work and stored energy with areas of the Lissajous curve. The first attempt to analyze nonlinear oscillatory shear stress in terms of work seems to go back to 1973 [Matsumoto *et al.* (1973)]. In their study, the work generated during the cycle was obtained as a sum of odd harmonics. The work was expressed by the sum of works, each of which is related to stored energy or dissipated energy. However, in their study, there was no discussion on the meaning of the work nor any analysis of the systems with different rheological properties. Although tracking the work during the cycle did not gain much attention since then, it has revived using various model equations [Giacomin *et al.* (2012), Giacomin *et al.* (2013)]. In these studies, by calculating work and viscous energy, the highest temperature of the system during the cycle was obtained. However, they neither concentrated on the meaning of the work nor considered the relationship between nonlinearity and the work generated during the cycle. In chapter IV, we focus on work and stored energy during the cycle and apply these concepts to constitutive equations and simulation results.

1.3 Complex fluids

The denotative definition of complex fluids is binary mixtures which have a coexistence between two phases. These fluids include suspensions or polymers (solid-liquid), granular (solid-gas), foams (liquid-gas), and emulsions (liquid-liquid). Complex fluids exist ubiquitously in our real life: foods, biofluids, personal care products, electronic and optical materials, plastic products, and so on [Larson (1999)]. Generally, complex fluids show a nonlinear relationship between stress and deformation. Under steady or oscillatory shear flow, complex fluids show interesting behaviors such as shear thinning, strain softening, shear thickening, strain hardening, yielding, rheopexy or thixotropy, and so on. In this thesis, particle suspension system is focused on.

1.3.1 Particle suspension systems

Systems with micrometer- or nanometer-sized particles suspended in a viscous liquid are defined as particle suspensions. Types of particles include not only monodisperse particle but also polydisperse, bimodal, and anisotropic particles. They are commonly used in industrial applications, such as slurries, paints, pastes, and functional materials, such as electrorheological fluids.

As it is relatively easy to deal with hard sphere systems theoretically, there are many studies in modeling, experiments, and simulations under simple

shear. The behaviors of hard sphere systems under oscillatory shear flow have also been studied extensively, both experimentally and via simulation [Petekidis *et al.* (2003), McMullan and Wagner (2009), Besseling *et al.* (2012), Koumakis *et al.* (2013), Koumakis *et al.* (2016)]. However, most studies concentrate on a system with the volume fraction near the freezing point where interesting rheological behaviors such as yielding or ordering are observed under oscillatory shear flow, and there exist only a few studies at intermediate volume fractions.

In soft particle systems, there are many reports, especially experimental studies, in which soft particle systems are analyzed by adopting a hard sphere model [Mason *et al.* (1997), Senff *et al.* (1999), Fuchs and Ballauff (2005), Siebenbürger *et al.* (2009)]. In simulations, soft sphere systems tend to be described by using inverse power potential (IPP), which controls the slope of the potential [Heyes and Braňka (2005), Heyes and Braňka (2008), Pieprzyk *et al.* (2014)].

Comparisons of soft and hard sphere systems are also reported, however, they concentrate on yielding behavior at high volume fractions [Grand and Petekidis (2008), Koumakis *et al.* (2012), Poulos *et al.* (2015)] or concentrate on the rheological properties of simple shear flow [Nzockdast and Morris (2012), Ding and Mittal (2015)]. Thus, characteristics at an intermediate volume fraction, which is lower than the freezing point, need to be investigated further under the oscillatory shear flow.

1.4 Outline of the thesis

In chapter II, description for Brownian dynamics (BD) simulation, and simulation systems are contained. In BD section, each term of Langevin equation, which is governing equation of BD, and used potentials in this thesis are described. In simulation systems section, information for the number of particles, volume fraction, and frequency range are included.

In chapter III, BD simulations under large amplitude oscillatory shear flow at an intermediate volume fraction in both hard and soft sphere systems have been carried out. First, two systems are compared by using strain sweep, Lissajous plot, and Fourier transform (FT). Then, elastic and viscous stresses for the two systems are calculated by using the stress decomposition method. Careful investigation of “double peaks”, which are experimentally observed only in the elastic stress of hard sphere systems, has been conducted. To know the structural origin of double peaks, a comparison of the structures of hard and soft sphere systems and the structures of hard sphere systems at different strain amplitudes, where double peaks appear and not, are compared. Excess entropy concept is adopted to evaluate the extent of particle alignment during the cycle. Finally, we suggest the structural characteristics which make double peaks in a simulation.

In chapter IV, the concept of work and stored energy, which has been rarely been considered in the past, is exploited to analyze the oscillatory shear stress. The inner area in the strain-stress Lissajous curve throughout one

cycle is known to be related to work, and that of the strain rate-stress Lissajous with stored energy. To precisely analyze the nonlinear stress helps to consider work and energy not only throughout a complete cycle but also during the cycle. In this chapter, we trace the work and energy during the oscillation. We apply this concept to perfectly elastic solid, purely viscous liquid, viscoelastic fluid, Bingham fluid, and particle simulation results. By this approach, the usefulness of this concept and the method for application are studied.

II Background

2.1 Brownian dynamics (BD) simulation

2.1.1 General description of BD

There are many simulation methods for colloidal dispersions such as Brownian dynamics (BD), Stokesian dynamics (SD), Multi-particle collision dynamics (MPCD), etc. [Foss and Brady (2000a), Foss and Brady (2000b), Gompper *et al.* (2009)]. In this thesis, due to plenty of reliable references, applicability to various systems, and relatively low computational cost, a BD simulation technique is used. Hydrodynamic, potential, and Brownian forces affect the motion of the particles. The governing equation is the Langevin equation, as given in Eq. (2-1),

$$m \frac{d\mathbf{v}_i}{dt} = \mathbf{F}_i^H + \mathbf{F}_i^P + \mathbf{F}_i^B \quad (2-1)$$

where m , \mathbf{v}_i , \mathbf{F}_i^H , \mathbf{F}_i^P , and \mathbf{F}_i^B are the mass of a particle, velocity vector, hydrodynamic force, potential force, and Brownian force of i^{th} particle, respectively. The left-hand side term can be neglected when the time scale is sufficiently long to relax particle momentum. When the particle is a sphere, hydrodynamic force is expressed as given in Eq. (2-2),

$$\mathbf{F}_i^H = -6\pi\eta a (\mathbf{v}_i - \mathbf{v}_i^\infty) \quad (2-2)$$

where η , a , and \mathbf{v}_i^∞ are the medium viscosity, radius of a particle, and imposed flow velocity at i^{th} particle, respectively. In this simulation, oscillatory shear flow $\mathbf{v}_i^\infty = \dot{\mathbf{r}}_0 \cdot \mathbf{x} \cos \omega t$ is imposed, where $\dot{\mathbf{r}}_0$, \mathbf{x} , and ω are the velocity gradient tensor, the position of particle and frequency, respectively.

Brownian force is defined by Eq. (2-3) and (2-4),

$$\langle \mathbf{F}_i^B(t) \rangle = 0 \quad (2-3)$$

$$\langle \mathbf{F}_i^B(t) \mathbf{F}_i^B(t') \rangle = 12k_B T \pi \eta a \delta(t - t') \mathbf{I} \quad (2-4)$$

where bracket indicates an ensemble average. Here, k_B , T , $\delta(t)$, and \mathbf{I} are the Boltzmann constant, temperature, Dirac delta function and unit tensor, respectively. It can be expressed by Wiener process as in Eq. (2-5),

$$\mathbf{F}_i^B(t) \Delta t = \sqrt{12k_B T \pi \eta a} \Delta \mathbf{W}_i(t) \quad (2-5)$$

where $\langle \Delta \mathbf{W}_i(t) \rangle = 0$ and $\langle \Delta \mathbf{W}_i(t) \Delta \mathbf{W}_i(t') \rangle = \delta(t - t') \mathbf{I} \Delta t$ are satisfied.

Langevin equation can be rearranged as Eq. (2-6) by using previous equations, and particle positions are updated by using this equation at each time step (Δt).

$$\Delta \mathbf{x}_i = \left[\mathbf{v}^\infty(\mathbf{x}_i) + \frac{1}{6\pi\eta a} \mathbf{F}_i^p \right] \Delta t + \sqrt{2k_B T / 6\pi\eta a} \Delta \mathbf{W}_i \quad (2-6)$$

One method used to describe hard sphere system is the potential-free (PF) method [Heyes and Melrose (1993), Foss and Brady (2000a), Wang and Swan (2016)]. In this method, the particles are moved by the force from the imposed flow and Brownian motion, and overlapped particles are relocated

to non-overlapped states. The moving distance of the overlapped particle is determined by Eq. (2-7),

$$\Delta x^{HS} = k\hat{\mathbf{r}}(\Delta r - 2a)H(2a - \Delta r) \quad (2-7)$$

where Δx^{HS} , Δr , H , and k indicate hard sphere displacement, the center-to-center distance between overlapped particles, Heaviside step function, and a constant that defines how far the overlapped particles are moved to the non-overlapped state, respectively. Moreover, $\hat{\mathbf{r}}$ denotes a unit vector \mathbf{r}/r . To prevent overlap, k should be larger than 0.5. When it is 0.5, the overlapped particles are relocated to contact distance, and when k is 1, the overlapped particle are relocated to a non-overlapped state as much as their overlapped distance. In this simulation, k is set as 1 [Heyes and Melrose (1993)]. Interparticle force in PF method is given as Eq. (2-8).

$$\mathbf{F}_i^P = 6\pi\eta a \frac{\Delta x^{HS}}{\Delta t} \quad (2-8)$$

In PF method, the particle stress from the interparticle force is calculated by using the radial distribution function (RDF) at contact distance ($2a$) as in Eq. (2-9) [Foss and Brady (2000a)],

$$\langle \Sigma_p \rangle = -N^2 k_B T a \int_{r=2a} \hat{\mathbf{r}} \hat{\mathbf{r}} g(\mathbf{r}) dS \quad (2-9)$$

where $g(\mathbf{r})$ and N indicate RDF and the number of particles, respectively. To change particle softness, the inverse-power potential (IPP) method is used, as presented in Eq. (2-10) [Mitchell *et al.* (1995)].

$$\varepsilon(r) = k_B T \left(\frac{2a}{r} \right)^n \quad (2-10)$$

where $\varepsilon(r)$ stands for potential between two particles. When the slope n is smaller than or equal to 12, it shows soft sphere characteristics. On the contrary, when n is larger than or equal to 18, it shows hard sphere characteristics [Brańka and Heyes (2006), Lange *et al.* (2009)]. When n is larger than 72, transport coefficients are hardly distinguishable at different n , and this potential describes true hard sphere systems as n goes to infinity. [Heyes and Brańka (2005)]. Interparticle in IPP method is given in Eq. (2-11).

$$\mathbf{F}_i^P = -\sum_{i \neq j} \frac{d}{d\mathbf{x}} \varepsilon(|\mathbf{x}_i - \mathbf{x}_j|) \quad (2-11)$$

Stress is obtained from the distance between two particles and the interparticle force in IPP as in Eq. (2-12).

$$\langle \Sigma_p \rangle = -n \langle \mathbf{x} \mathbf{F}^P \rangle \quad (2-12)$$

2.1.2 Application of BD

By using different interparticle forces, Brownian dynamics (BD) simulation can be easily applied to various particle systems from repulsive to attractive particles. Due to this extensibility, BD is widely used for understanding the dynamics of various systems, although BD does not consider near field hydrodynamic interaction accurately. BD has the advantage for describing colloidal glass and colloidal gel systems, where hydrodynamic interaction is

less important. In the colloidal glass system, due to highly packed particles, hydrodynamic interaction is screened out and the particles are mostly affected by direct contact of the particles. In the colloidal gel, non-hydrodynamic interaction, such as van der Waals attraction dominates particle dynamics.

As BD can readily track particle position as time proceeds, it is useful to observe microstructures and to calculate the properties of various systems in diverse flow conditions. One of monumental BD studies in simple shear flow was carried by Foss and Brady (2000a). In their paper, to get the diffusivity along the flow direction, hopping mechanism was suggested by relating information from rheological properties and microstructure. Another main subject in simple shear flow is transient start-up of shear. In BD simulation, stress overshoot is also observed as seen in the experiment and structural characteristic of this overshoot is also explored [Park *et al.* 2015]]. In oscillatory shear flow, by relating the total stress and structure one-to-one or by concentrating on structure variation as time proceeds, rheological behaviors such as yielding can be explained [Koumakis *et al.* (2013); Lee *et al.* (2015)]. Although hydrodynamic force is not considered precisely, there are many studies that report structures from BD simulation of intermediate volume fraction, which correspond to experimental results at least qualitatively [Nzockdast and Morris (2012), Ding and Mittal (2015), Wang and Swan (2016)]. These studies indicate that BD simulation of intermediate volume fraction may be reasonable when microstructure is mainly focused.

2.2 Simulation systems

The number of particles is 25^3 . All particles are allocated in the lattice and the initial configuration is obtained after an equilibration step. Subsequently, simulations are conducted at every γ_0 and frequency (ω) from this initial configuration. The stress in each oscillatory shear test is obtained by averaging the stresses during the 10 cycles after the stress is stabilized. The Lees-Edwards periodic boundary condition is used when shearing [Lees and Edwards (1972)]. ω is normalized by multiplying it by the particle characteristic time ($6\pi a^3 \eta / k_B T$). Normalized ω can be defined as the Deborah number (Eq. 2-13).

$$De = 6\pi a^3 \omega \eta / k_B T \quad (2-13)$$

To revise the volume fraction of systems with different particle softness, a reduced coupling parameter ($\Gamma/\Gamma_{freezing}$) is used. The effective volume fraction (Γ) is normalized by the volume fraction at the freezing point ($\Gamma_{freezing}$) of each system. It is reported that reduced transport coefficients at equilibrium or in simple shear can be plotted on a master curve when plotting as a function of the reduced coupling parameter [Lange *et al.* (2009), Ding and Mittal (2015)]. As this value indicates how far the system is away from the freezing point, it is a useful parameter when comparing systems with different particle softness. The freezing point at specific slope n can be found in the previous paper [Agrawal and Kofke (1995)]. For example, the freezing point corresponds to volume fractions 0.494, 0.493, and 0.827 for the PF,

IPP with $n = 54$, and IPP with $n = 8$, respectively.

In chapter III, soft (IPP with a slope of 8) and hard sphere (PF, IPP with a slope of 54) systems are analyzed. The range of De is from 20 to 100 (mostly $De = 80$) and $\Gamma/\Gamma_{freezing} = 0.61, 0.71$, and 0.81 (mostly 0.61). In section 4.4 (section of Application to BD simulation), hard sphere (PF) system at $De = 20$ and 80 , $\Gamma/\Gamma_{freezing} = 0.61$ is analyzed.

III. Stress decomposition analysis in hard and soft sphere suspensions

3.1 Motivation and objectives

Small amplitude oscillatory shear (SAOS) flow is widely used due to its simplicity and ease of analysis. Fundamental rheological properties, such as storage modulus (G') and loss modulus (G''), are obtained through SAOS analysis, allowing the extent of elastic or viscous characteristics in various material systems to be evaluated. However, when strain amplitude (γ_0) is large, shear stress is no longer linear and has high harmonic contributions. Though it is not easy to deal with nonlinear behaviors, it is useful and informative to know the response of a material in the large amplitude oscillatory shear (LAOS) regime [Hyun *et al.* (2011)].

One of analysis method for LAOS stress is the stress decomposition method [Cho *et al.* (2005)]. This method decomposes total oscillatory shear stress into elastic and viscous stress by using symmetric characteristic of oscillatory shear flow. Nam *et al.* (2011) applied this method to hard sphere systems and observed double peaks in elastic stress near the flow reversal (FR) point. These double peaks are observed only in hard sphere systems as far as we know. Thus, understanding their structural origin will give an insight into the behavior of hard sphere systems under oscillatory shear flow.

Also, double peaks themselves may be used for characterizing hard sphere systems. However, the double peaks have not been reported further, and their structural origin has never been explored.

Moreover, as mentioned in section 1.2.2 (analysis method for LAOS), stress decomposition is under disputes due to a disagreement between structure or rheological state and the stress calculated from the stress decomposition at each time [Poulos *et al.* (2013)]. Thus, before suggesting the structural origin of double peaks, it needs to answer the question of how to relate structure and elastic stress properly.

In this chapter, we first try to reproduce double peaks of elastic stress by simulation, which are reported to be observed only in hard sphere experiments. We compare and analyze the hard and soft sphere systems by using the stress decomposition method. Second, to find a method that relates elastic stress and structure, the elastic stress and structure are carefully inspected by using the concept of excess entropy. Finally, we try to suggest the structural origin of double peaks, which is not revealed yet, by exploring particle microstructure and the characteristic of the elastic stress during the whole cycle.

3.2 Analysis of hard and soft sphere systems

3.2.1 Strain sweep

Comparison of two systems is carried out by using analysis of their oscillatory shear stress. At first, strain sweep results at $\Gamma/\Gamma_{freezing} = 0.61$ and $De = 80$ for two systems are shown (Fig. 3-1). Here, G'_0 means G' of the linear regime at each system, and G' and G'' are the first harmonic moduli (G'_1 and G''_1).

At small γ_0 (linear regime, $\gamma_0 \leq 0.2$), normalized G' and G'' are not varied much with an increase of γ_0 . When γ_0 exceeds the linear regime, nonlinear characteristics are shown in both systems.

In soft sphere system, G' is about 2.5 times higher than G'' in linear regime, and crossover of G' and G'' is observed at near $\gamma_0 = 1$. Strain thinning or softening (both G' and G'' decreasing as γ_0 increases) behavior is observed [Hyun *et al.* (2002)]. These results indicate that the elastic property is more dominant in small γ_0 regime, whereas the viscous property is more dominant in large γ_0 regime in soft sphere system.

In hard sphere systems, G' is similar to G'' in the linear regime, and weak strain overshoot (G' decreasing, G'' increasing followed by decreasing as γ_0 increases) behavior is observed. Weak strain overshoot behavior is also shown in hard sphere system in an experiment [Mason and Weitz (1995)]. The viscous and elastic moduli are similar at small γ_0 regime, whereas, the

viscous property is more dominant at large γ_0 regime. When $\gamma_0 \leq 3$, decreasing rate of G' for hard sphere system is lower than that for soft sphere system, and it is higher when $\gamma_0 > 3$. Though hard and soft sphere systems have the same reduced volume fraction and frequency, their rheological characteristics differ significantly.

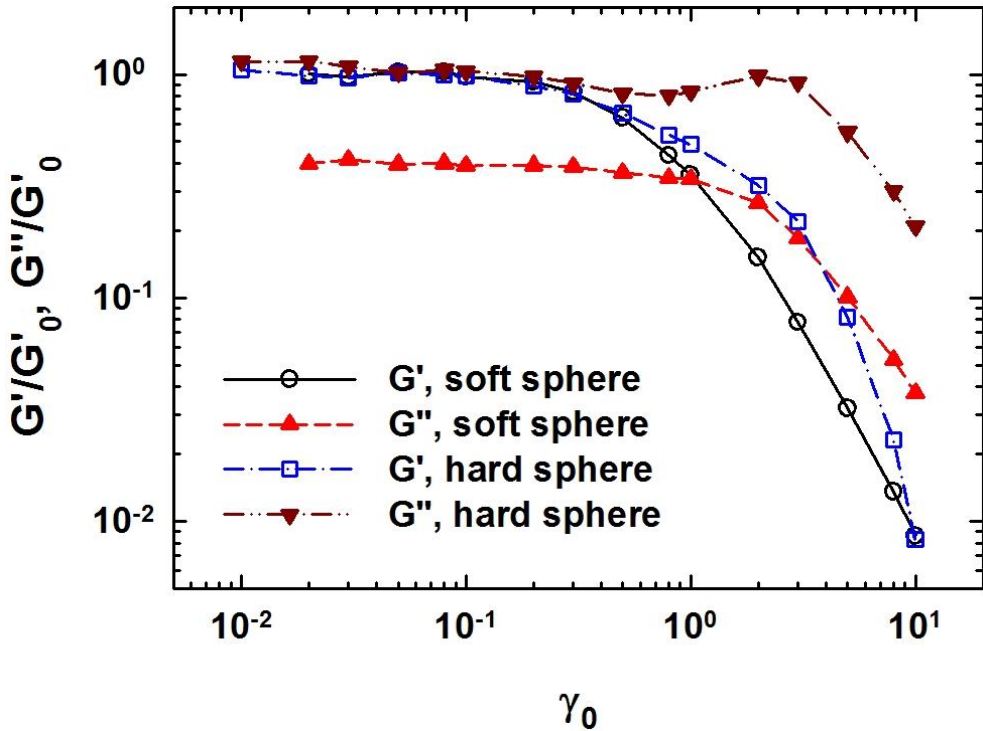


Fig. 3-1 G' and G'' of soft hard sphere systems as a function of γ_0 at $\Gamma/\Gamma_{freezing} = 0.61$ and $De = 80$. G' and G'' are normalized by G'_0 at each system.

3.2.2 Lissajous curve

Strain ($x - \sigma$) – σ and strain rate ($y - \sigma$) Lissajous curves of soft and hard sphere systems are plotted (Fig. 3-2, 3-3). All stresses are normalized by their maxima at each condition (γ_0 and De). Inner areas of $x - \sigma$ and $y - \sigma$ Lissajous are related to the viscous and elastic characteristics of the materials, respectively. Thus, by checking the areas of $x - \sigma$ and $y - \sigma$ Lissajous at the same γ_0 and De , the viscous and elastic characteristics can be compared simply.

In the both systems, when γ_0 is small, curves show ellipses, and as γ_0 increases, curves are distorted. As De increases, elastic characteristic increases, and as γ_0 increases, viscous characteristic increases. The variation of the curve for soft sphere system is more significant than that for hard sphere system. These curves have a correspondence with strain sweep results.

In soft sphere system, at $\gamma_0 = 1$, $x - \sigma$ Lissajous show lozenge-like shape, at $\gamma_0 = 3$, they show almost quadrangle shape, and at $\gamma_0 = 8$, they show quadrangle shape with pointy edges. In hard sphere system, the variation trend is similar to soft sphere system but curves show a much rounder shape.

For $y - \sigma$ Lissajous, soft sphere system clearly shows inner intersection point at $\gamma_0 = 8$, whereas hard sphere system shows dumbbell-like shape at $\gamma_0 = 3$, and the intersection is not clearly shown. The inner area of $y - \sigma$ narrows down much at large γ_0 and the elastic characteristic is less

pronounced in this condition. This results can be related to strain sweep result of hard sphere system, which shows G'' over 10 times higher than G' .

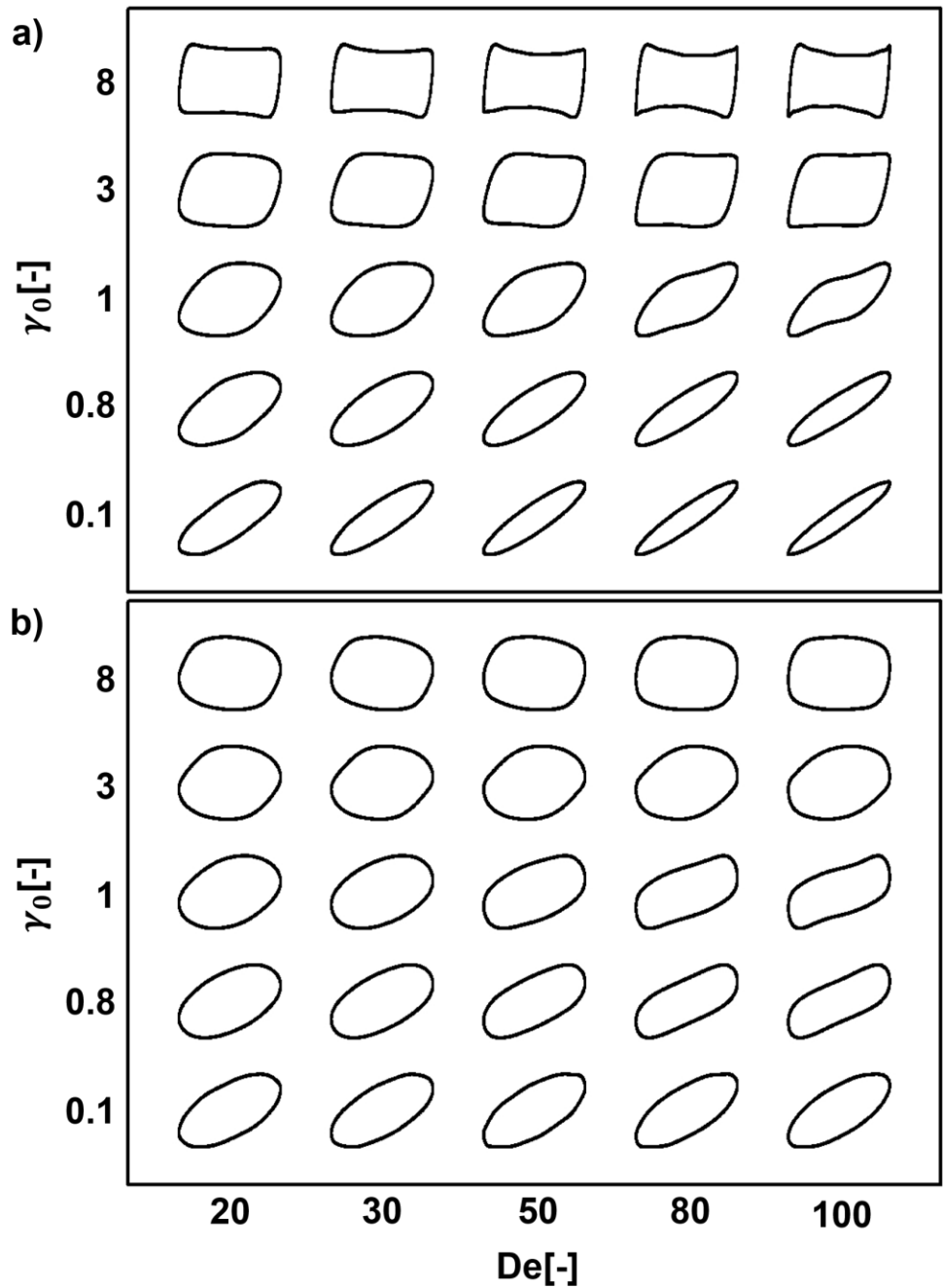


Fig. 3-2 $x - \sigma$ Lissajous curves of a) soft, b) hard sphere systems at $\Gamma/\Gamma_{freezing} = 0.61$. Each trajectory is positioned in a Pipkin space according to the imposed values of γ_0 and De .

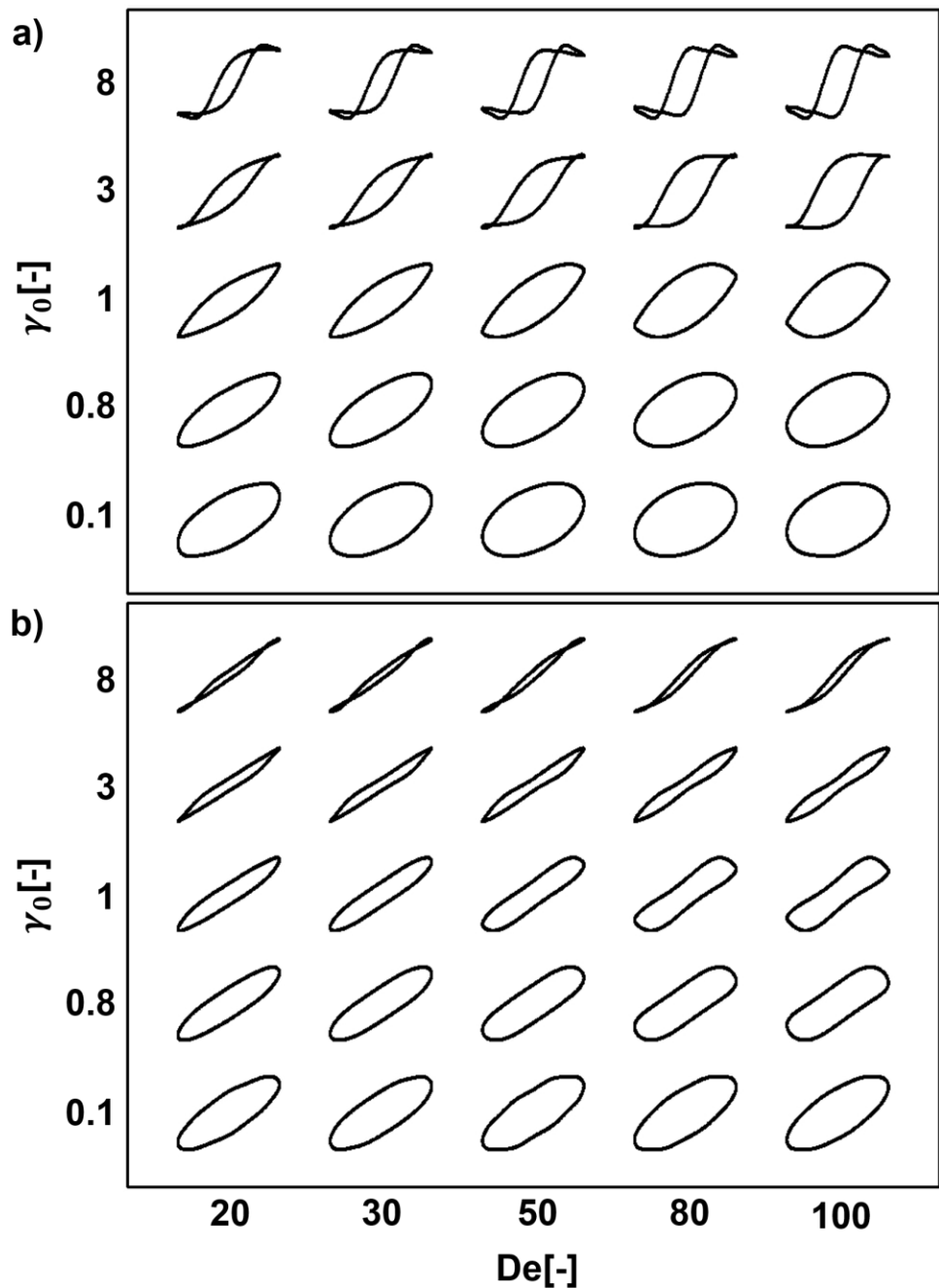


Fig. 3-3 $y - \sigma$ Lissajous curves of a) soft, b) hard sphere systems at $\Gamma/\Gamma_{freezing} = 0.61$. Each trajectory is positioned in a Pipkin space according to the imposed values of γ_0 and De .

3.2.3 Fourier transform (FT)

Fourier transform rheology is widely used for analyzing nonlinear oscillatory shear stress. As mentioned in section 1.2.2, I_3/I_1 is an important factor in this method. I_3/I_1 of soft and hard sphere systems are plotted as a function of γ_0 at $De = 50, 80$, and 100 in Fig. 3-4.

In the both systems, slopes are about 2 at small γ_0 regime regardless of De , which leads to Q parameter $((I_3/I_1)/\gamma_0^2)$ being constant. As De increases, I_3/I_1 becomes higher at small γ_0 regime. In soft sphere system, I_3/I_1 shows a monotonical increase as γ_0 increases, resulting in higher value than that of hard sphere system at high γ_0 regime. In hard sphere system, it shows maximum at $\gamma_0 = 0.8$, then it decreases. Minimum of I_3/I_1 is observed at about $\gamma_0 = 2$ or 3 followed by an increase. These I_3/I_1 characteristic difference in two systems was also reported in the previous experimental paper [Grand and Petekidis (2008)].

It is notable that a decrease in hard sphere system is observed in similar regime to overshoot peak of strain sweep. It implies that the difference in rheological properties can be mainly induced by stress or structural characteristic difference in this regime. Careful investigation of this regime is required to compare two systems.

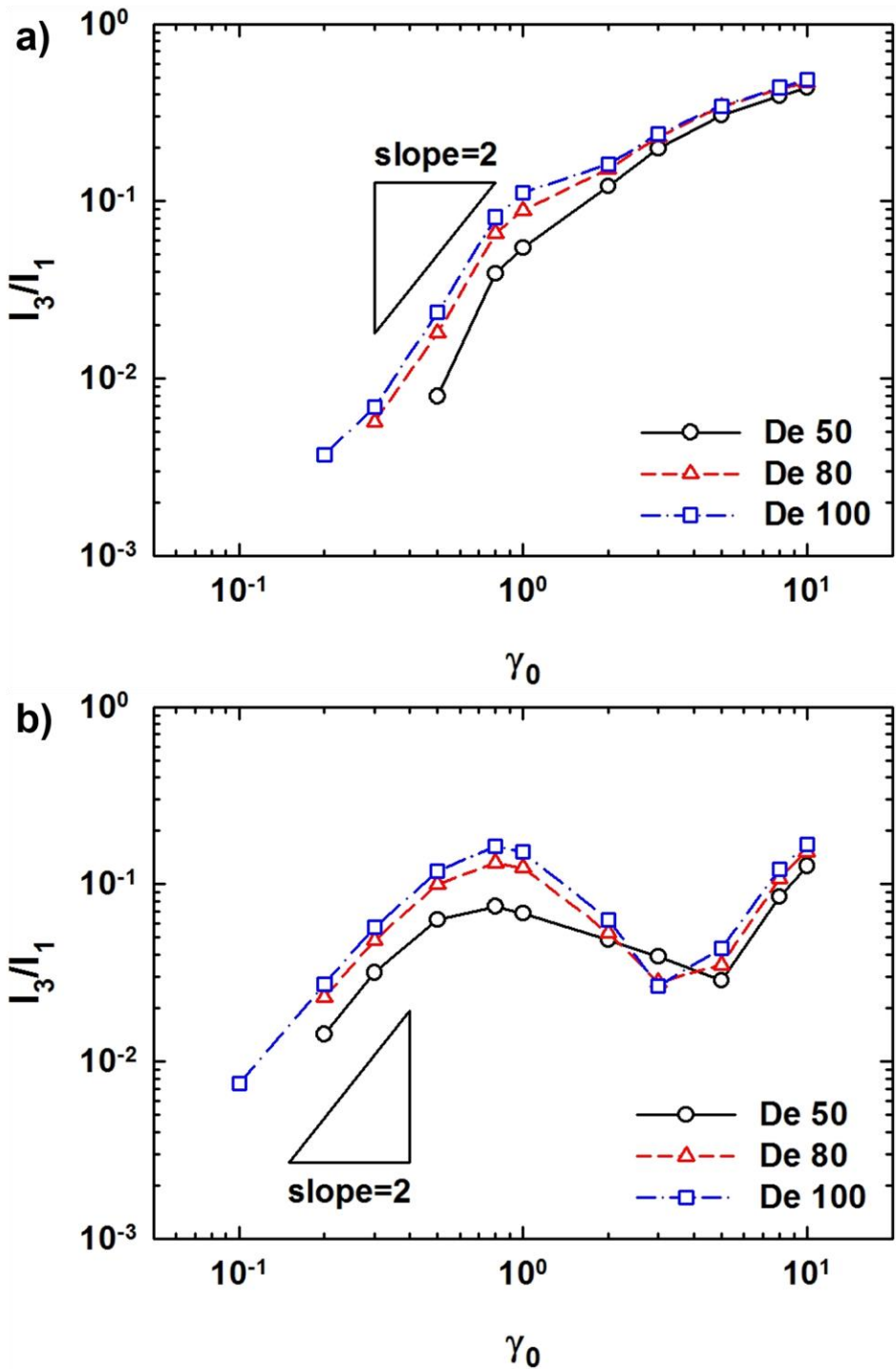


Fig. 3-4 I_3/I_1 of a) soft, b) hard sphere systems as a function of γ_0 at $De = 50, 80$, and 100 .

3.3 Stress decomposition and double peaks

3.3.1 Total, elastic, and viscous shear stresses of hard and soft spheres

In this section, comparison of total, elastic and viscous stress for two systems are carried out by using stress decomposition method. Fig. 3-5 a) shows the total, elastic and viscous stresses in a wide range of γ_0 at $\Gamma/\Gamma_{freezing} = 0.61$ and $De = 80$ from the PF, which describes a hard sphere system. Fig. 3-5 b) shows the elastic stresses for De from 20 to 100. Here, all stresses are normalized by their maxima.

As γ_0 increases, the total stress is no longer sinusoidal shape and becomes distorted, which leads to a shape change in the elastic and viscous stresses. It is to be noted that double peaks are observed in the elastic stress near flow reversal point when γ_0 is large, and this has rarely been reported. The double peaks are also observed in experimental with hard spheres [Nam *et al.* 2011]. As seen in Fig. 3-5 b), the double peaks appear over a wide range of De values at intermediate γ_0 in this simulation.

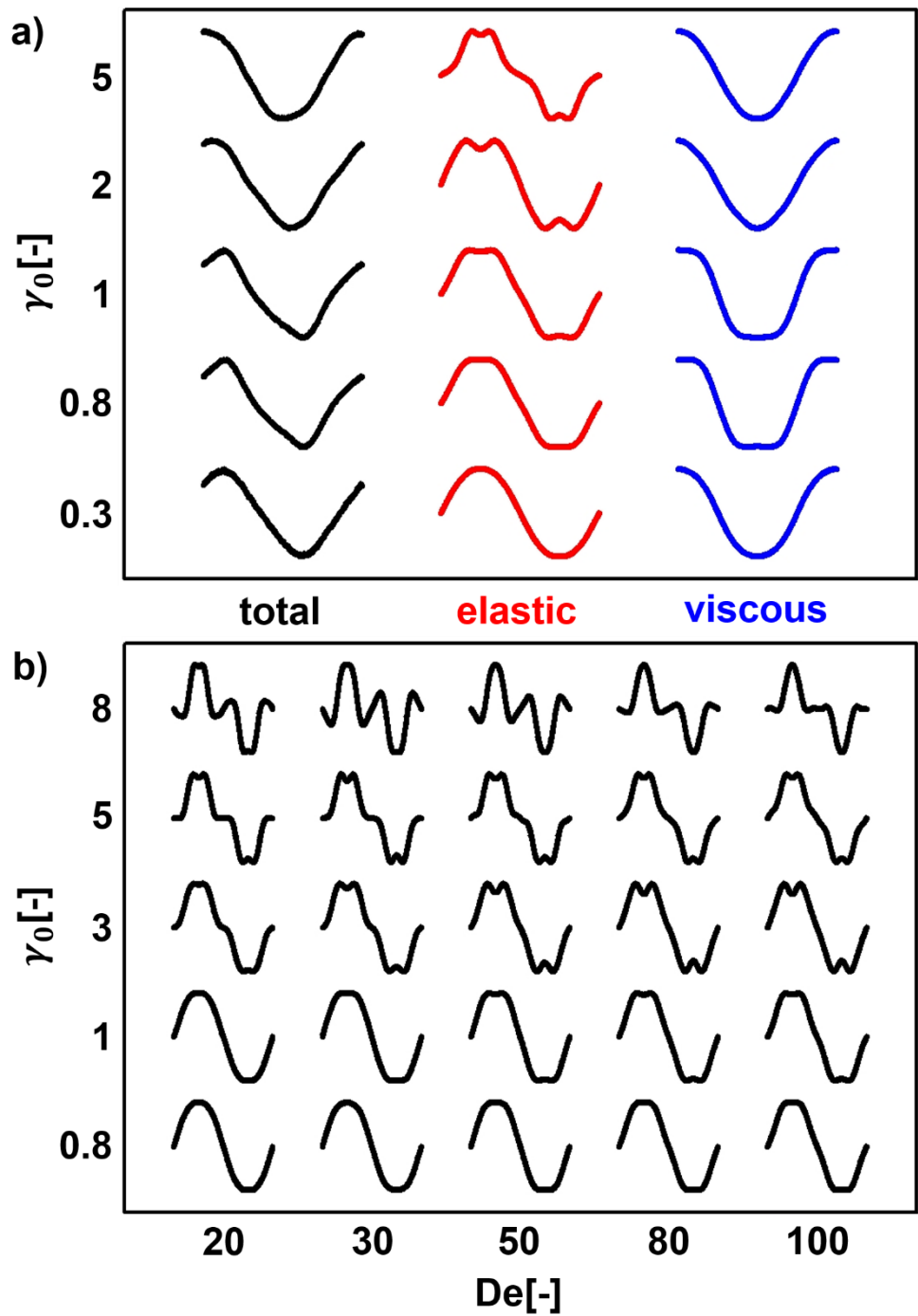


Fig. 3-5 a) The total, elastic, and viscous stresses at $De = 80$; b) elastic stresses from $De = 20$ to 100 for PF at $\Gamma/\Gamma_{freezing} = 0.61$.

By increasing the slope of IPP, the particles change from soft to hard spheres. The total, elastic, and viscous stresses of two IPP sets are shown in Fig. 3-6. In this simulation, the particles are soft when the slope of IPP is 8, and hard when the slope of IPP is 54. As the $\Gamma/\Gamma_{freezing}$ is fixed to 0.61 in the PF case, the $\Gamma/\Gamma_{freezing}$ is also fixed to 0.61. It is to be noted that the actual volume fractions are different in hard and soft sphere systems.

For soft spheres, although the shape of the total, elastic, and viscous stresses changes as γ_0 is varied, double peaks are not observed in elastic stress (Fig. 3-6 a)). In contrast, in Fig. 3-6 b), which describes a quasi-hard sphere system, double peaks are observed in elastic stress and the shape of each stress is similar to that presented in Fig. 3-5 a) which uses PF. From these results, it can be inferred that double peaks appear only in simulations that describe hard sphere system.

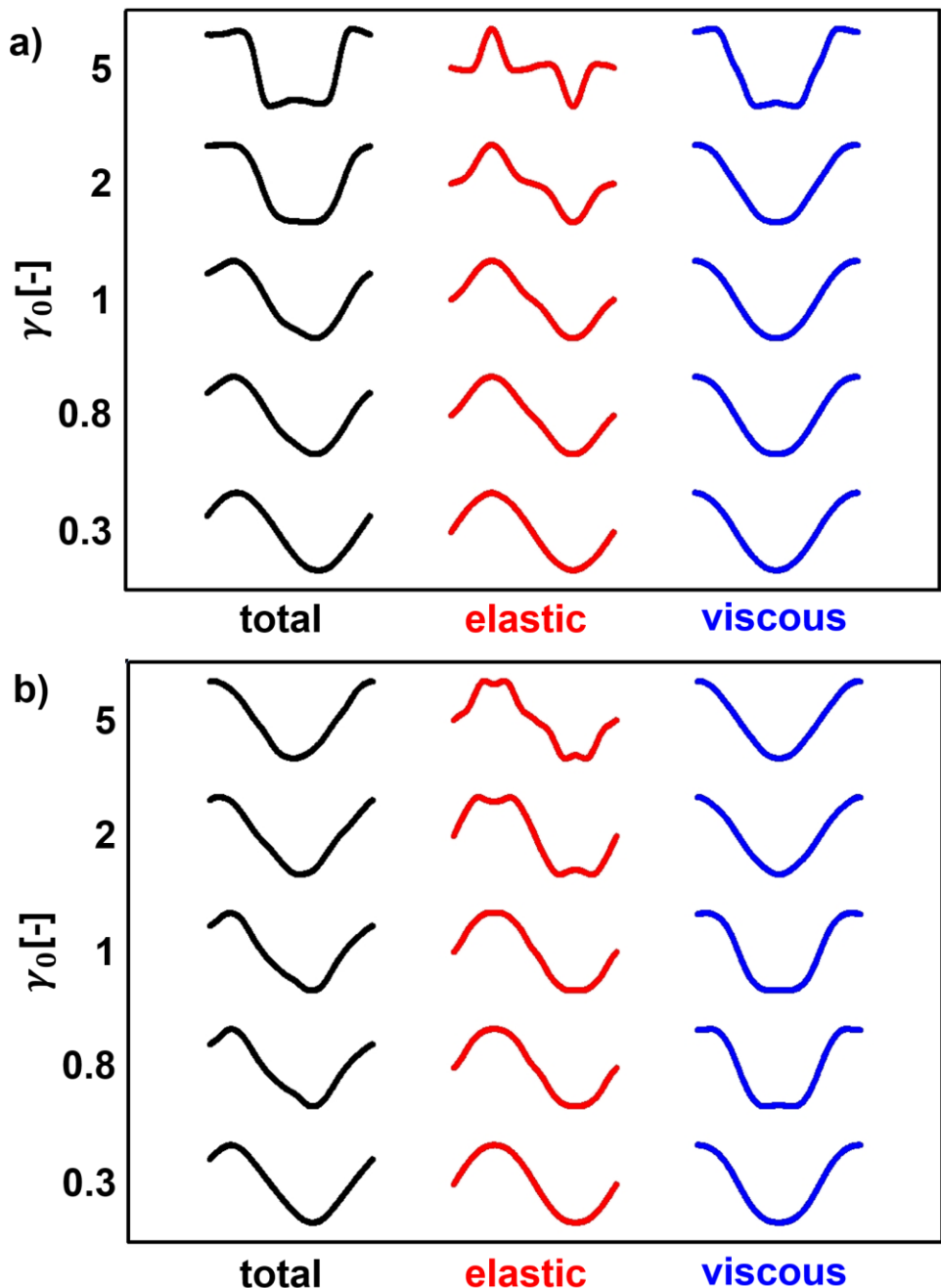


Fig. 3-6 The total, elastic, and viscous stresses for a) $n = 8$ (soft sphere), b) $n = 54$ (quasi-hard sphere) for IPP method, at $\Gamma/\Gamma_{freezing} = 0.61$ and $De = 80$.

3.3.2 Double peaks characteristics

To quantify the characteristics of the double peaks, both depth and width are defined as shown in Fig. 3-7, in which the elastic stress is plotted at $\Gamma/\Gamma_{freezing} = 0.61$, $De = 80$, and $\gamma_0 = 3$. The horizontal axis is time, which is normalized by the duration of one cycle. The vertical axis is the elastic stress, which is normalized by its maximum. The depth is defined as the gap between the normalized elastic stress at peak and that at the local minimum (at the normalized time of 0.25). The width is the normalized time interval between the two peaks. The maximum of depth and width are 1 and 0.5, respectively.

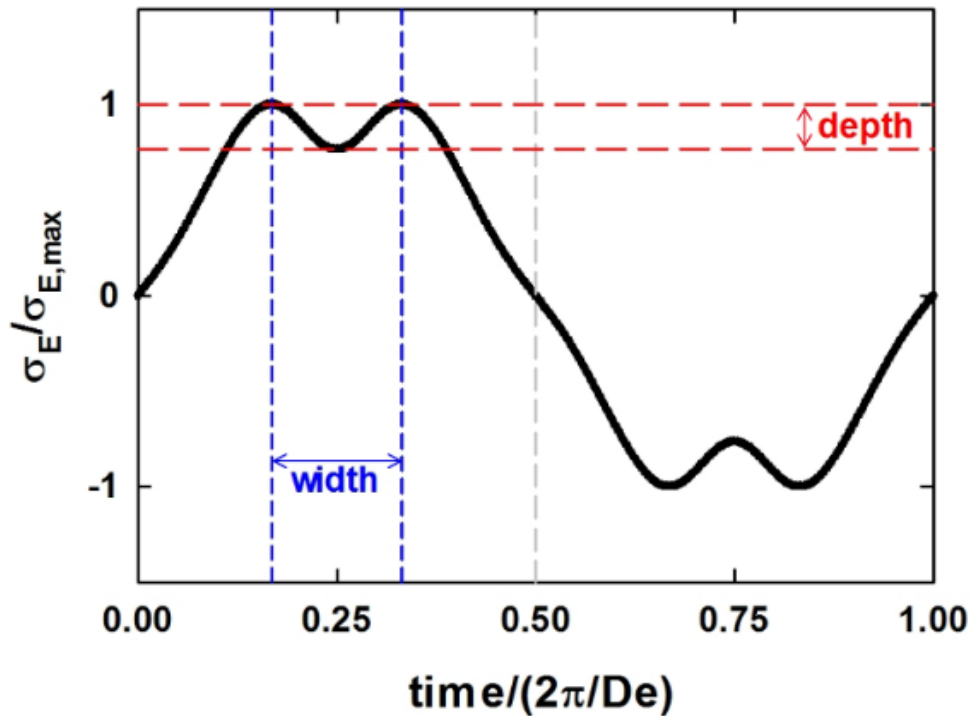


Fig. 3-7 The definition of depth and width when double peaks appear. The elastic stress is plotted at $\Gamma/\Gamma_{freezing} = 0.61$, $De = 80$, and $\gamma_0 = 3$.

In this simulation, double peaks are observed only in the hard sphere system (i.e., PF or IPP; $n = 54$). The γ_0 range in which double peaks appear is wider when using PF, which better describes a hard sphere, than for the case of IPP with a slope of 54 (referring the number of points in Fig. 3-8). In Fig. 3-8, the open symbols connected with black solid lines represent the results from PF, while the filled symbols connected by red dashed lines represent the results from IPP.

As γ_0 increases, both depth and width increases followed by decreases. The depth from PF, which has better hard sphere characteristics, is larger than that obtained from IPP. The maximum locates at $\gamma_0 = 3$. For width, the variation is less pronounced, and the maximum is observed at $\gamma_0 = 2$.

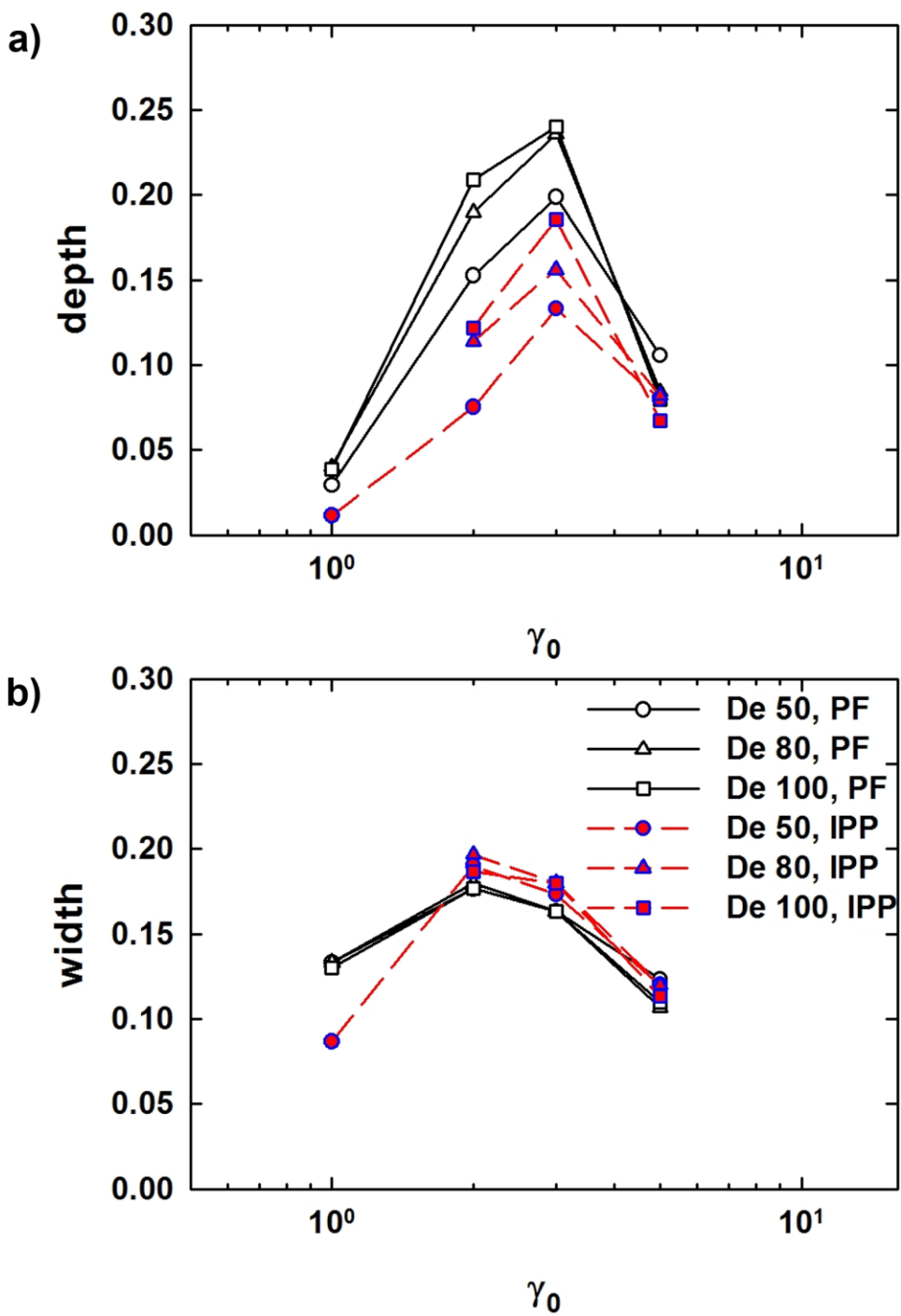


Fig. 3-8 Double peaks a) depth and b) width at $De = 50, 80$, and 100 as a function of γ_0 for PF and IPP with $n = 54$ at $\Gamma/\Gamma_{freezing} = 0.61$.

3.4 Stress and structural analysis

3.4.1 Soft and hard spheres

The stress and structure of a hard sphere system, which shows double peaks, and a soft sphere system, which does not show double peaks, are compared when $\Gamma/\Gamma_{freezing}$, De , and γ_0 are 0.61, 80, and 3, respectively. In this section, the hard sphere system is simulated using PF, and soft sphere system using IPP with $n=8$. In Fig. 3-9, the solid curves indicate total stress, and the dashed curves indicate elastic stress. The black curve is for the soft sphere system (IPP; $n=8$) and the red one is for the hard sphere system (PF). The total and elastic stresses are normalized by the maximum value of the total stress for each system. The blue columns indicate the regime between two peaks. Point A represents the first peak before flow reversal (FR), and point B represents the second peak after FR.

In Fig. 3-9, shape differences between the total stress of soft and hard spheres may be clearly observed in the regime where double peaks appear. Whereas, the shape differences are not significant in the rest of the time domain. The differences in total stress in the blue regime also affect the differences in elastic stress. Based on the shape of the stress, double peaks appear when the total stress decreases rapidly before FR, which is followed by a gradual decrease after FR. To obtain more information on the origin of two peaks, the structures of the hard and soft spheres at points A and B, which represent the two peak points, are compared.

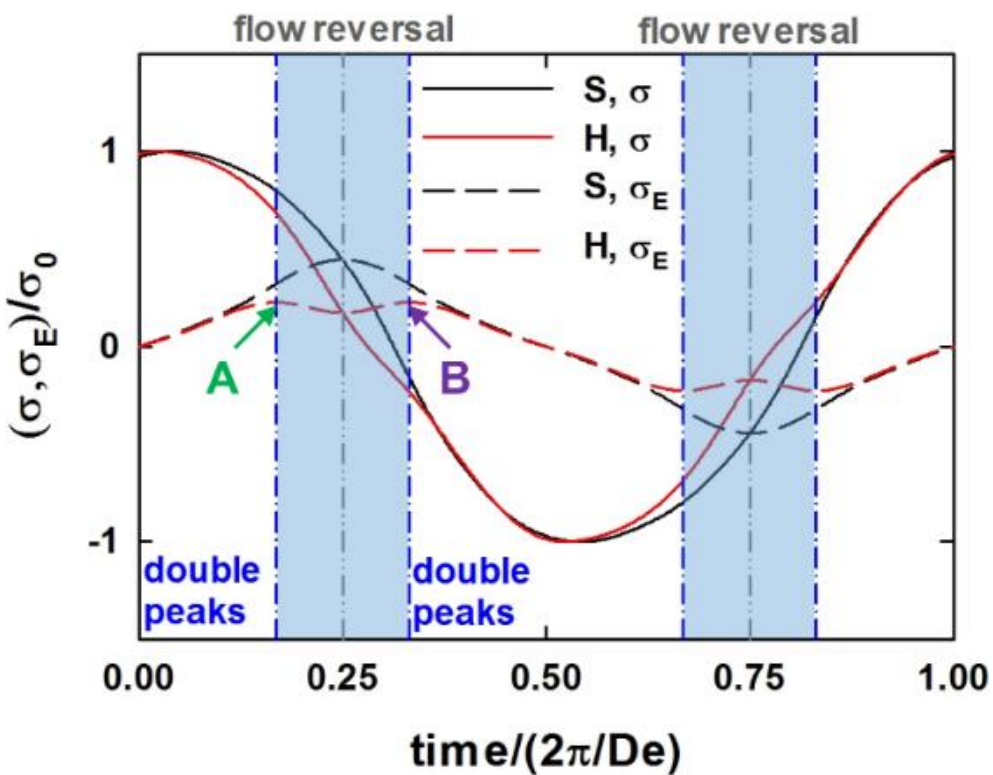


Fig. 3-9 The total and elastic stresses of soft sphere (S, IPP; $n = 8$) and hard sphere (H, PF) systems when $\Gamma/\Gamma_{freezing} = 0.61$, $De = 80$, and $\gamma_0 = 3$.

Initially, the pair distribution function (PDF) is inspected. The particles within a distance $\pm 5a$ on the velocity-velocity gradient plane ($-5a < x, y < 5a$) and $\pm 0.05a$ ($-0.05a < z < 0.05a$) to the vorticity direction relative to the reference particle are analyzed. Note that two systems have the same $\Gamma/\Gamma_{freezing}$. Fig. 3-10 a) and 3-10 c) show the results for soft spheres, while Fig. 3-10 b) and 3-10 d) show results for hard spheres. Fig. 3-10 a) and 3-10 b) show the results obtained at point A in Fig. 3-9, while Fig. 3-10 c) and 3-10 d) are the results obtained at point B. In Fig. 3-10 the more reddish the PDF is, the more possibility that there is a particle at that point. Likewise, the more bluish the PDF is, the less possibility that there is a particle at that point. The circle at the center indicates double of the particle size. At point A in Fig. 3-9, the flow direction is from left to right, and at point B, the flow direction is from right to left.

In both cases, the particles are aligned to the compressional axis and are scarcely aligned along the extensional axis. A lot of particles are in touch for hard spheres (as evidenced by red color at contact), while particle density at contact is small (a red point is not observed at contact) and alignment to the flow direction is insignificant for soft spheres. Though not included in this thesis, the differences in alignment are observed not only at points A and B but also during the whole cycle.

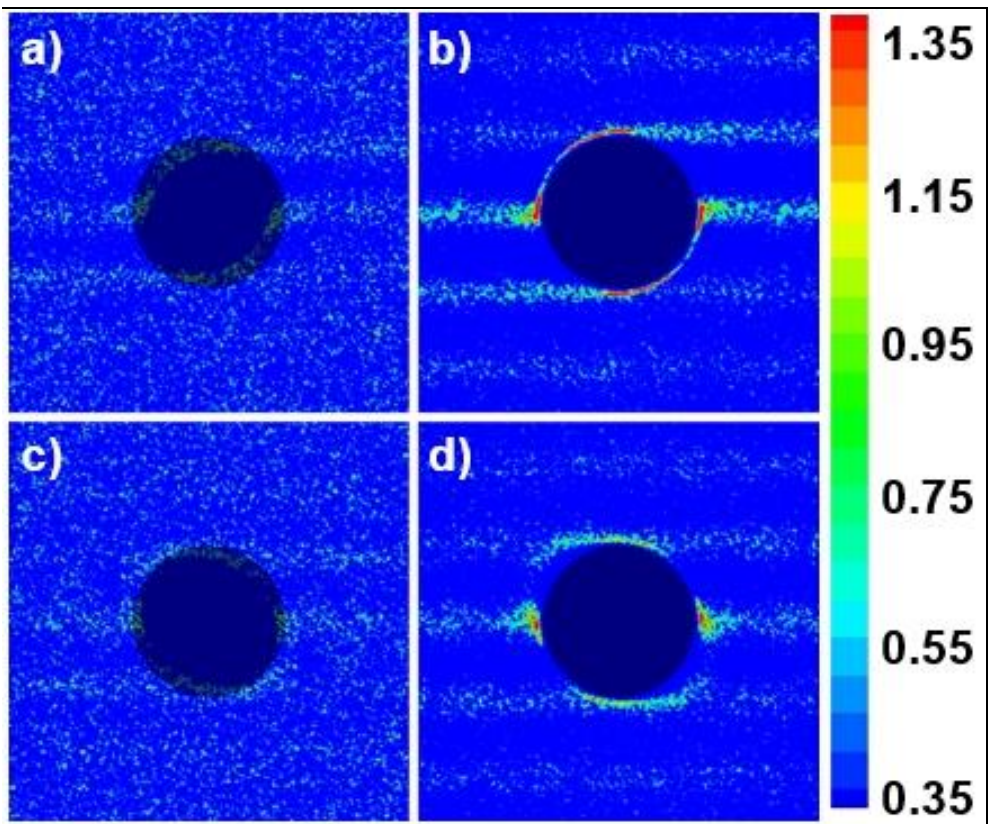


Fig. 3-10 PDF of a) point A of soft sphere, b) point A of hard sphere, c) point B of soft sphere, and d) point B of hard sphere.

Next, the radial distribution function (RDF) $g(\mathbf{r})$ at the two points are inspected. As the effective radius r in RDF can vary with particle softness, it is necessary to amend the radius. In this study, r is revised according to $\Gamma_{rel}^{1/3} = (\Gamma/\Gamma^{HS,freezing})^{1/3}$ [Lange et al. 2009]. Here, $\Gamma^{HS,freezing}$ indicates the volume fraction at the freezing point of the hard sphere system. The RDF at points A and B in Fig. 3-9 are plotted in Fig. 3-11. The black curve is for hard spheres and the red curve is for soft spheres. The solid curve is the result at point A and the dash-dot curve is the result at point B. The filled circle indicates the location of the first peak, which represents the maximum in each case.

The peak is sharp and tall for hard spheres, while it is broad and short for soft spheres. The $g(\mathbf{r})$ at long-range ($r\Gamma_{rel}^{1/3} > 2.5$) is similar to each other. In the hard sphere system, when proceeding from point A to point B, the value of r at the peak does not change much; however, $g(\mathbf{r})$ changes significantly. In the soft sphere system, the value of r at the peak changes a lot and $g(\mathbf{r})$ increases by only a small amount.

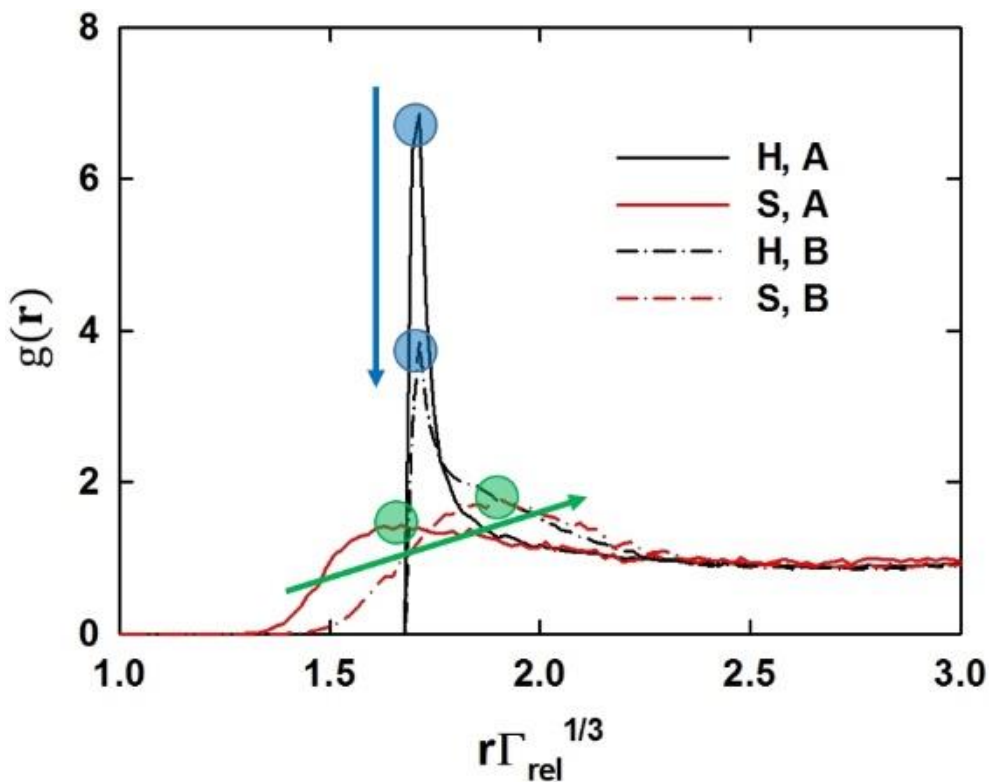


Fig. 3-11 RDF at points A and B for hard sphere (H, PF) and soft sphere (S, IPP; $n = 8$) systems.

Concentrating on the values of r and $g(r)$ at the first peak, their values during the cycle are tracked in Fig. 3-12. The black symbols are for the soft sphere system, while the red symbols for the hard sphere system. The open symbols represent the results before FR, while the filled symbols are the results after FR. Only the results during a half cycle are plotted because the results after half cycle are the same as before half cycle. The solid arrows are guidelines that show the path before FR, while the dashed arrows are the guidelines that show the path after FR.

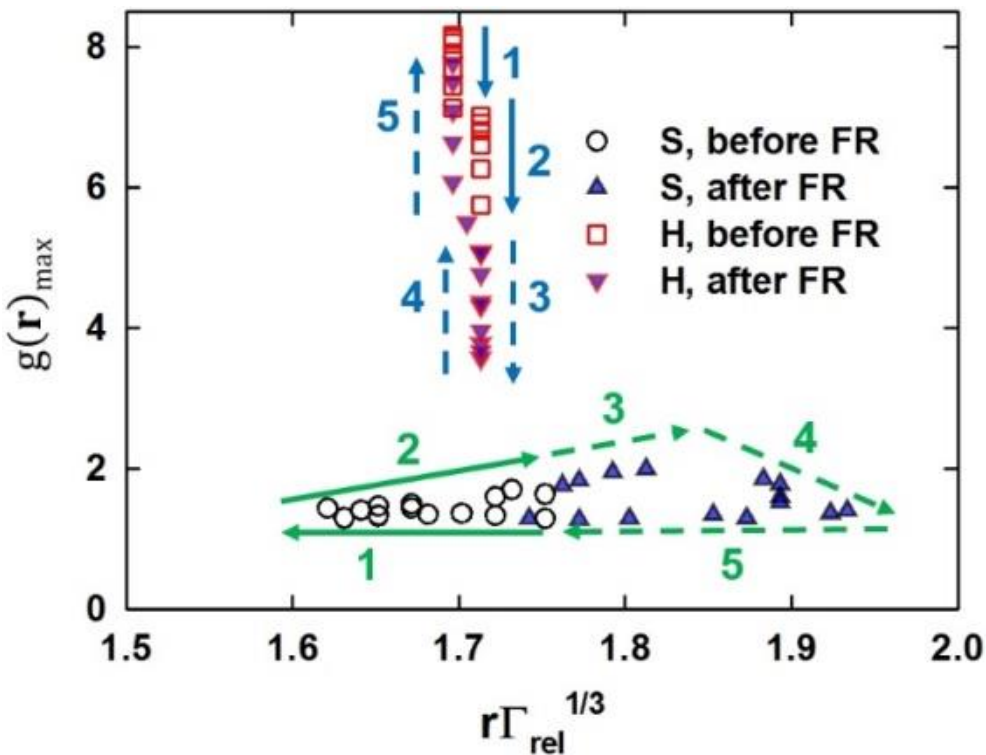


Fig. 3-12 The location of the first peak in RDF during a half cycle in both soft (S, IPP; $n = 8$) and hard sphere (H, PF) systems.

For soft spheres, the variation of r is more pronounced than that of $g(\mathbf{r})$ at the first peak. In contrast, for hard spheres, the variation of $g(\mathbf{r})$ is more pronounced than that of r . This difference is triggered depending on whether overlapping is permitted or not. When the compressive force is imposed to hard spheres, most particles are located in near contact ($2a, r\Gamma_{rel}^{1/3} \approx 1.69$) because a hard sphere cannot be overlapped. In contrast, soft spheres can overlap, which may cause particle distribution around $r\Gamma_{rel}^{1/3}$. Note that the direction of force from the flow field and the interparticle force is opposite to the compressional axis. When the flow is weakened, compressed particles are pushed away as the interparticle force becomes comparatively stronger.

For a hard sphere system, which is indicated by red symbols in Fig. 3-12, the value of $g(\mathbf{r})$ at contact is quite large at the initial stage of the cycle. As time proceeds and approaches FR, the flow velocity is reduced, which reduces compressive forces so that the particles are pushed away from each other, in a manner similar to relaxation in an equilibrium state. Therefore, r increases slightly and $g(\mathbf{r})$ decreases significantly. These processes are represented by the arrows 1 and 2 in the figure, which indicates the change of RDF before FR. As the flow changes direction after FR, the particles, which are aligned to the compressional axis before FR, become realigned in the opposite direction for a while, and shortly after FR, the value of $g(\mathbf{r})$ near the contact point decreases continuously. As the flow becomes stronger away from FR, the particles are compressed again at the contact point. Therefore, the value of r is the same as that at contact location and $g(\mathbf{r})$

increases. These processes correspond the arrows 3, 4, and 5 in the figure, which indicate the change of RDF after FR.

For soft spheres, which are indicated by the black symbols in Fig. 3-12, at the initial stage of the cycle where the flow is strong, the $g(r)$ does not change much and the particles are compressed to each other. At the latter stage before FR, as the flow is weakened, the closely located particles are moved away from each other. Therefore, $g(r)$ increases only slightly and r increases a lot. These processes are represented by arrows 1 and 2 in the figure, which indicate the change of RDF before FR. Shortly after FR, though flow direction is reversed, the structure formed in the previous compressional axis is maintained. As time proceeds, this maintained structure is pushed away to the extensional axis of reversed flow field (previous compressional axis), which makes both $g(r)$ and r increase. Then the particles are spread out and no significant structure is formed. Thus, $g(r)$ increases followed by a decrease while r increases. Long after FR, as the particles are affected continuously by the flow, the particles begin to compress again and, as a result, r continuously decreases. These processes correspond the arrows 3, 4, and 5 in the figure, which indicate the change of RDF after FR.

Due to the differences in overall structural alignment of the particles as seen in PDF and the differences in structure formation and deformation mechanism during the cycle as can be seen in RDF, soft sphere systems do not show double peaks, but they appear in hard sphere system.

3.4.2 Hard sphere at different strain amplitude

In this section, the stress and structure of the hard sphere system at two γ_0 , one with double peaks and the other without, are compared. The simulation is performed with PF condition at $\Gamma/\Gamma_{freezing} = 0.61$ and $De = 80$. In this condition, double peaks are observed in the range of γ_0 from 1 to 5. To compare cases in which double peaks appear and not, $\gamma_0 = 0.8$ and $\gamma_0 = 1$ are selected as low γ_0 boundary. Likewise, $\gamma_0 = 5$ and $\gamma_0 = 8$, are selected as high γ_0 boundary. The stresses at those four γ_0 are compared by pairing two by two. Fig. 3-13 a) shows the total and elastic stress at $\gamma_0 = 0.8$ and 1, and points C and D indicate the first and second peak, respectively, at $\gamma_0 = 1$. Fig. 3-13 b) shows the total and elastic stress at $\gamma_0 = 5$ and 8, and points E and F indicate the first and the second peak, respectively, at $\gamma_0 = 5$. The black curves indicate a condition in which double peaks do not appear, while the red curves indicate a condition in which double peaks appear. The solid lines represent total stress, and the dashed lines represent elastic stress. All stresses are normalized by the maximum of the total stress at each γ_0 .

The total stress shows little differences than differences between hard and soft sphere systems in the regimes represented by the blue columns. Thus, it is hard to draw some description about the appearance of double peaks from total stress shape and to do that structural analysis is needed.

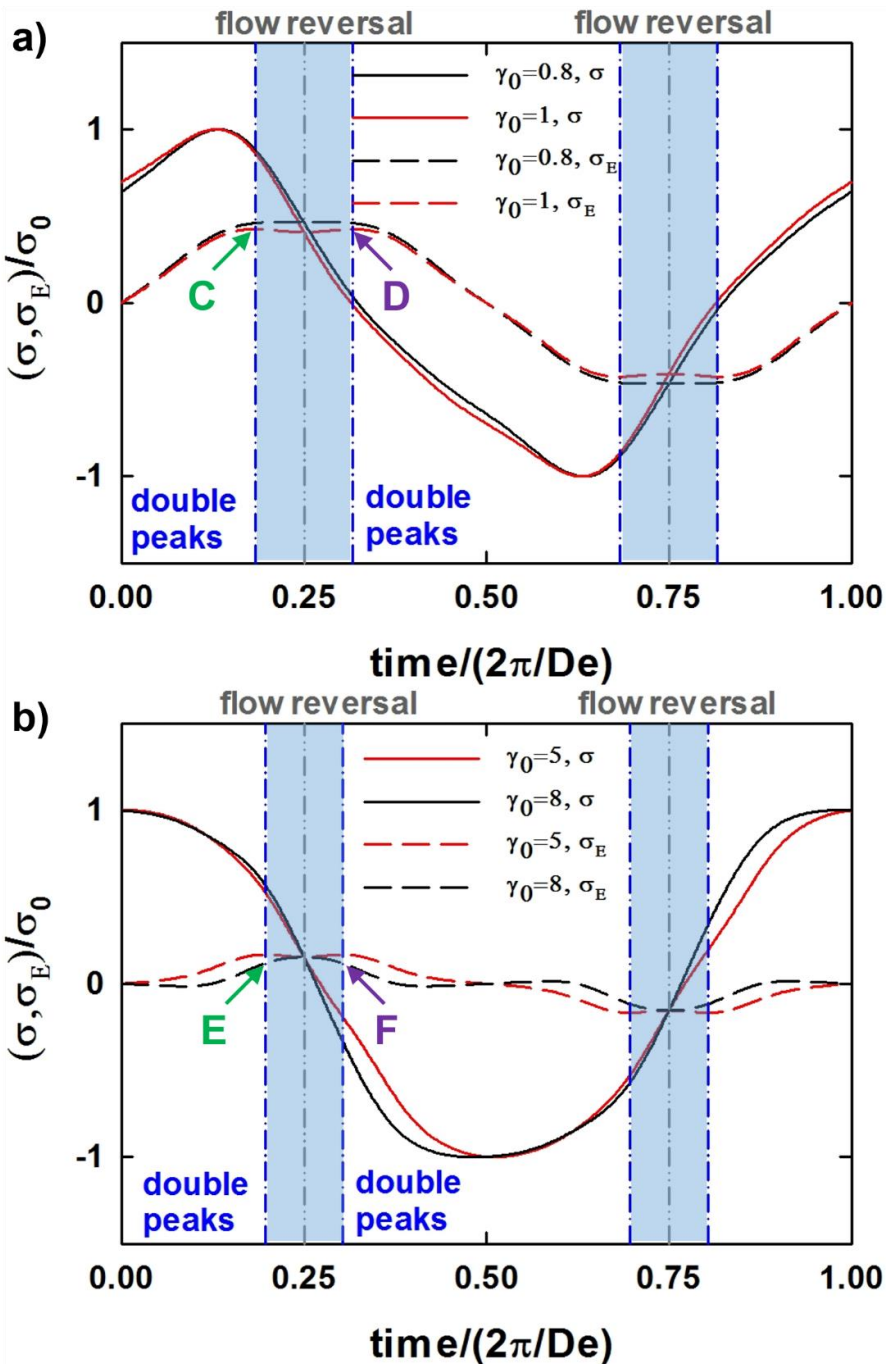


Fig. 3-13 Total (solid line) and elastic stresses (dashed line) at a) $\gamma_0 = 0.8$ and 1 and b) $\gamma_0 = 5$ and 8. Double peaks are not observed at $\gamma_0 = 0.8$ and 8, but double peaks are observed at $\gamma_0 = 1$ and 5.

The PDF obtained at peak points are illustrated in Fig. 3-14. As γ_0 increases, more particles are aligned to the compressional axis or flow direction. The structures, whether double peaks appear ($\gamma_0 = 1$ or 5) or not ($\gamma_0 = 0.8$ or 8), are not much different. It is notable that the PDF at points C and D and that at points E and F are clearly different, even though the elastic stresses are the same. Thus, it is hard to match elastic stress and structure one-to-one at each time. This discordance is also pointed out in previous papers [Rogers and Letinga (2012), Poulos *et al.* (2013)]. So it will be necessary to adopt a different structure analysis tool to correlate elastic stress and structure.

To quantify the extent of particle ordering, the concept of two-body excess entropy is adopted [Truskett *et al.* (2000), Ding and Mittal (2015)]. Two-body excess entropy s_2 represents full excess entropy of the whole system [Dzugutov 1996]. This approach has advantages because the structure under oscillatory shear flow, whose structure varies as time proceeds, can be quantified as a single value at a given time as in Eq. (3-1),

$$s_2 = -\frac{\rho}{2} \int \{g(\mathbf{r}) \ln g(\mathbf{r}) - [g(\mathbf{r}) - 1]\} d\mathbf{r} \quad (3-1)$$

where $g(\mathbf{r})$ is RDF and ρ is number density. When $-s_2$ goes to infinity, it implies a perfect crystal structure. When it is near zero, it implies a totally disordered system. The extent of particle alignment during the cycle is evaluated by using this value.

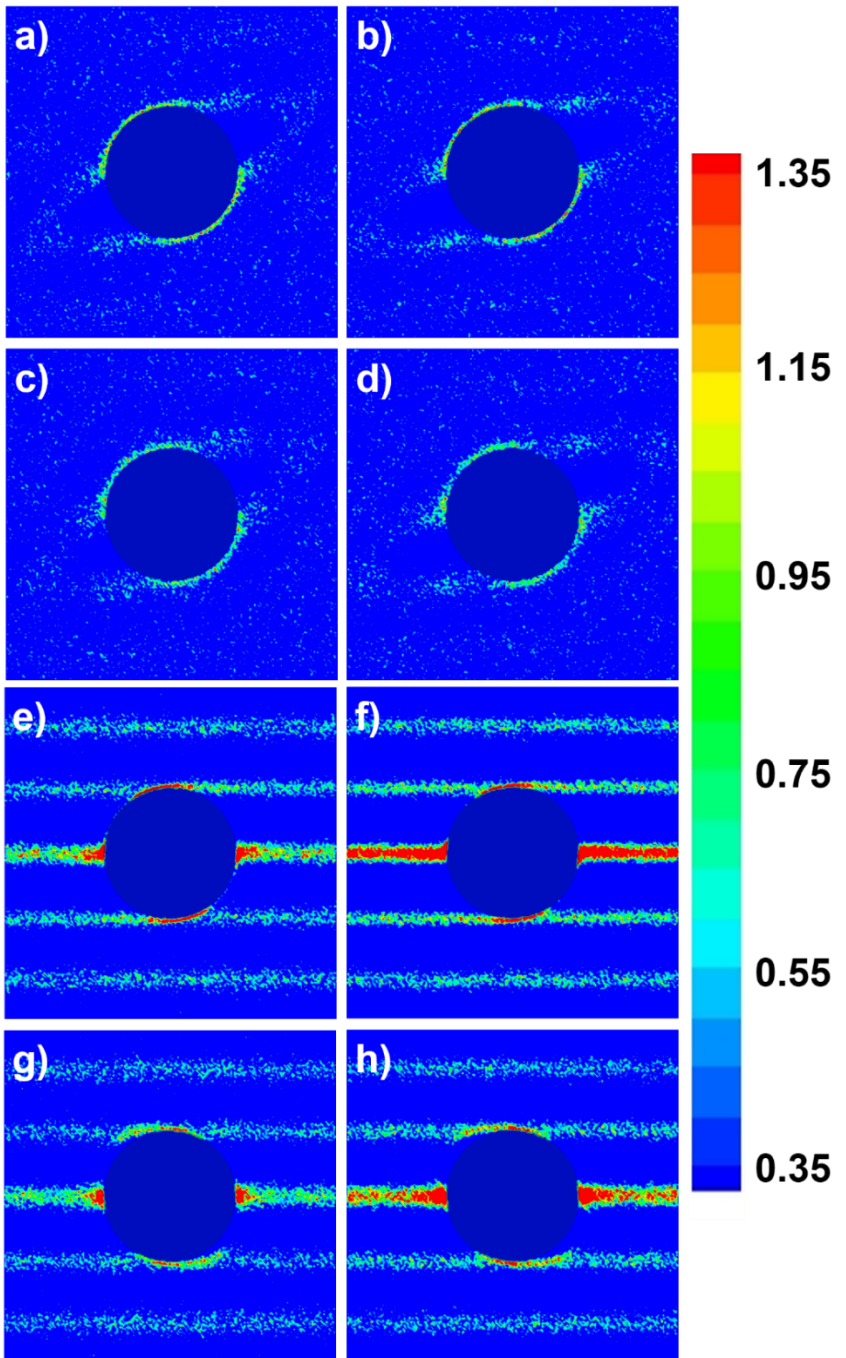


Fig. 3-14 PDF for a) $\gamma_0 = 0.8$, point C, b) $\gamma_0 = 1$, point C, c) $\gamma_0 = 0.8$, point D, d) $\gamma_0 = 1$, point D, e) $\gamma_0 = 5$, point E, f) $\gamma_0 = 8$, point E, g) $\gamma_0 = 5$, point F, h) $\gamma_0 = 8$, point F.

Fig. 3-15 a) is the total stress and excess entropy for $\gamma_0 = 0.8$ and 1, while Fig. 3-15 b) presents those for $\gamma_0 = 5$ and 8. The solid lines represent the total stress, and the dashed lines represent the excess entropy. The red curves show the results with double peaks and the black curves show the results without double peaks. The total stress and excess entropy are normalized by their maxima. At maximum excess entropy, the particles are well-packed along the compressional axis and the structure is highly ordered. In contrast, the structure is poorly ordered at minimum excess entropy.

Excess entropy shows a maximum before FR and minimum after FR. The moment of minimum excess entropy is observed earlier as γ_0 increases. This indicates that the rate of realignment to the opposite direction after FR becomes larger as γ_0 increases. Although the total stress or other structural analysis are not so much different between the two γ_0 , the difference in excess entropy is notable in the double peaks regime. The differences between the maximum and minimum of excess entropy are larger when double peaks appear (Fig. 3-15, red curves) than in the absence of double peaks (Fig. 3-15, black curves).

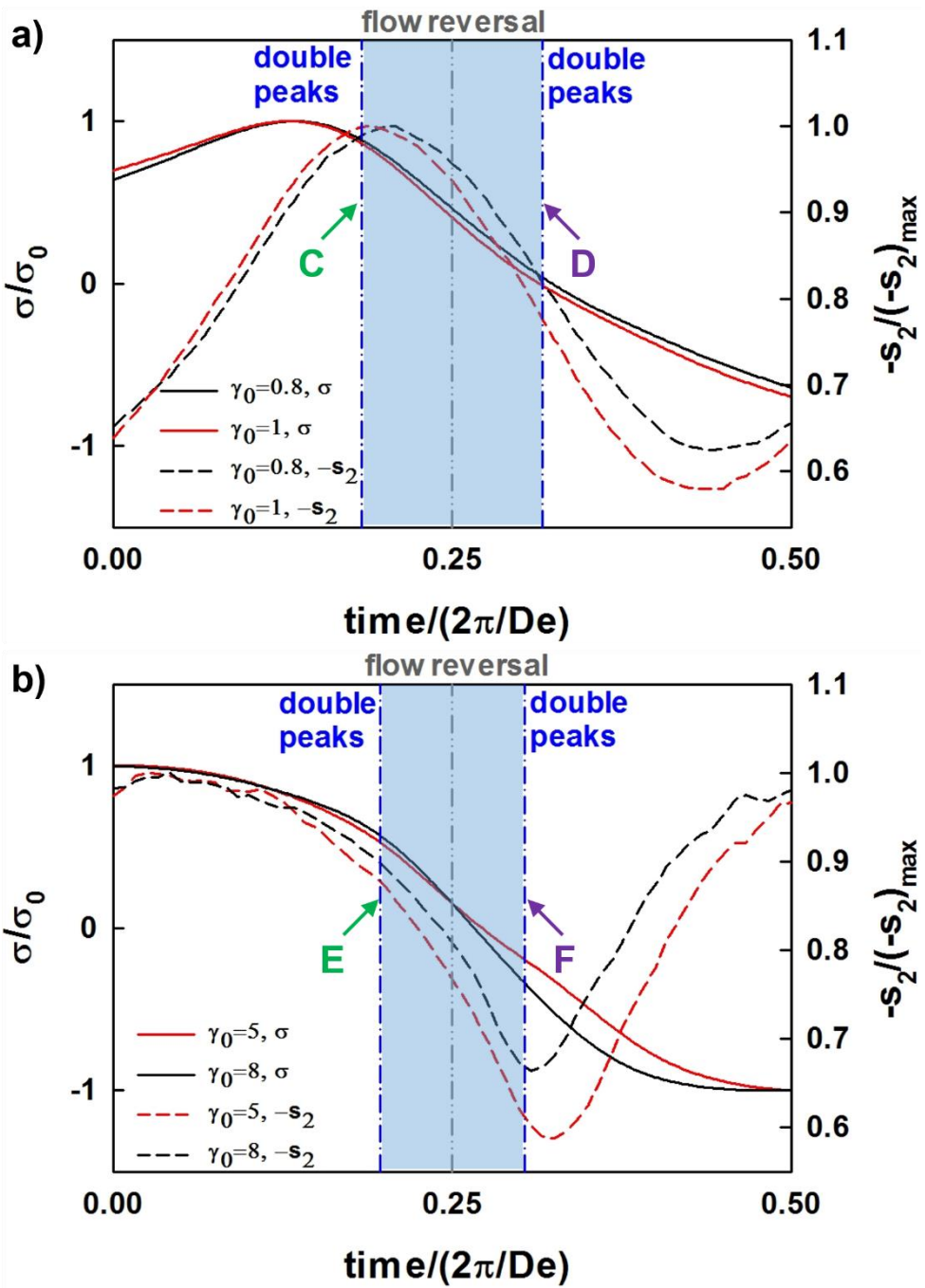


Fig. 3-15 Normalized total stress (solid line) and excess entropy (dashed line) during half cycle at a) $\gamma_0 = 0.8$ and 1 and b) $\gamma_0 = 5$ and 8.

The difference between the maximum and minimum of the normalized excess entropy is plotted as a function of γ_0 in Fig. 3-16. When this value is large, there exists a significant structural difference between two.

The difference between maximum and minimum excess entropy increases with the increase in γ_0 , and the maximum is observed at $\gamma_0 = 3$, after which it decreases. In this simulation, double peaks are observed in the range of γ_0 from 1 to 5, as indicated in the red column of Fig. 3-16. When the difference between maximum and minimum exceeds a critical value (~0.4), double peaks appear. Thus, double peaks are observed only when the structural difference between the maximum-ordered state and the minimum-ordered state is large during the cycle. The subtracted excess entropy shows a similar curve with depth (Fig. 3-8 a)), which is one of the characteristic values of double peaks. Depth increases as γ_0 increases, and the maximum depth is observed at $\gamma_0 = 3$, after which it decreases. These characteristics (i.e., maxima at $\gamma_0 = 3$ and curve shape) are observed in both the depth of the elastic stress curve and in the results of the quantitative structural analysis (excess entropy). And the extent of the difference between the maximum- and minimum-aligned states is closely related to the depth of the double peaks.

From the excess entropy results, double peaks are created when the structural difference is large during the oscillation. In the previous section (3.3.1, Soft and hard spheres), the variation of $g(\mathbf{r})$ at contact is significant for hard sphere systems, which can lead double peaks to appear. This result

also supports the observation that double peaks are observed when the structural difference during the cycle is large. Therefore, it can be concluded that double peaks appear at the systems that the difference between maximum- (before FR) and minimum-ordered states (after FR) is significant during the cycle. Moreover, the structural origin of double peaks is revealed when considering the structure and the elastic stress of the whole cycle together. This result can be inferred by considering the structures and the elastic stress in the whole cycle rather than them at each time step.

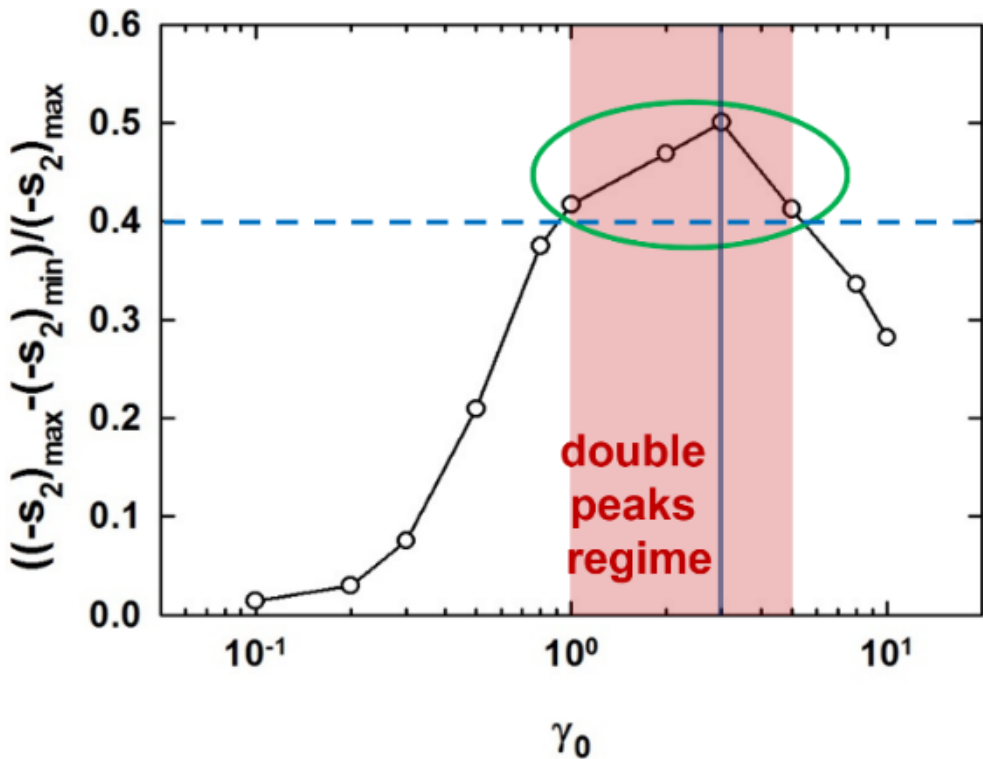


Fig. 3-16 The difference in the maximum and minimum of excess entropy as a function of γ_0 .

3.5 Conclusions

It has been reported that double peaks are observed in elastic stress in experiments for hard sphere suspensions. However, the structural origin of those double peaks has not been reported and no quantification of the double peaks has been conducted. In this chapter, to quantify the double peaks, their depth and width are defined. The depth and widths of the double peaks were found to exhibit maxima with increased γ_0 .

To investigate the structural origin of double peaks, PDF and the first peak of RDF for both soft and hard spheres were compared at the same $\Gamma/\Gamma_{freezing}$, ω , and γ_0 . As a result, an overall structural difference during the cycle, a difference in structural formation before FR, and a deformation mechanism after FR were observed. These differences were found to determine the appearance of double peaks.

Structures of hard sphere systems at two γ_0 , one that shows double peaks and the other does not were compared at the same $\Gamma/\Gamma_{freezing}$ and ω . The structures at the same time but different γ_0 are not much different, but the structures at two peaks at the same γ_0 are clearly different. Thus, it was hard to correlate the elastic stress and structure one-to-one at each time.

To correlate elastic stress with structure and to quantify the structure during a cycle, the concept of excess entropy was applied to the hard sphere system. By applying this concept, it was concluded that double peaks are observed when the structural difference between the maximum- and minimum-ordered

states is large.

By inspecting the structure of hard and soft spheres and the structure of hard sphere system at different γ_0 , the interpretation method for stress decomposition results and the conditions for the presence of double peaks are suggested. To relate elastic or viscous stress from stress decomposition with structure, it is necessary to consider them of the whole cycle rather than them at each time step. Double peaks were observed when there is a large difference between the structure before FR, in which the particles are aligned to the compressional axis, and after FR, in which particle structure on previous compressional axis is broken.

Appendix 3A

Total (Fig. 3A-1), elastic (Fig. 3A-2), and viscous (Fig. 3A-3) stresses with time in Pipkin space for soft sphere (IPP with a slope of 8) and hard (PF) systems at $\Gamma/\Gamma_{freezing} = 0.61$ are plotted. All stresses are normalized by their maxima.

Description for total and elastic stresses are partially included in section 3.1.2 (section of Lissajous curve) and 3.2.1 (section of Total, elastic, and viscous shear stresses of hard and soft spheres). Stress shapes in viscous stress are not varied much for hard sphere system, whereas double peaks with respect to half cycle are observed in large γ_0 for soft sphere system. This double peaks in viscous stress for soft sphere system is clearly affected by total stress shape (Fig. 3A-1a).

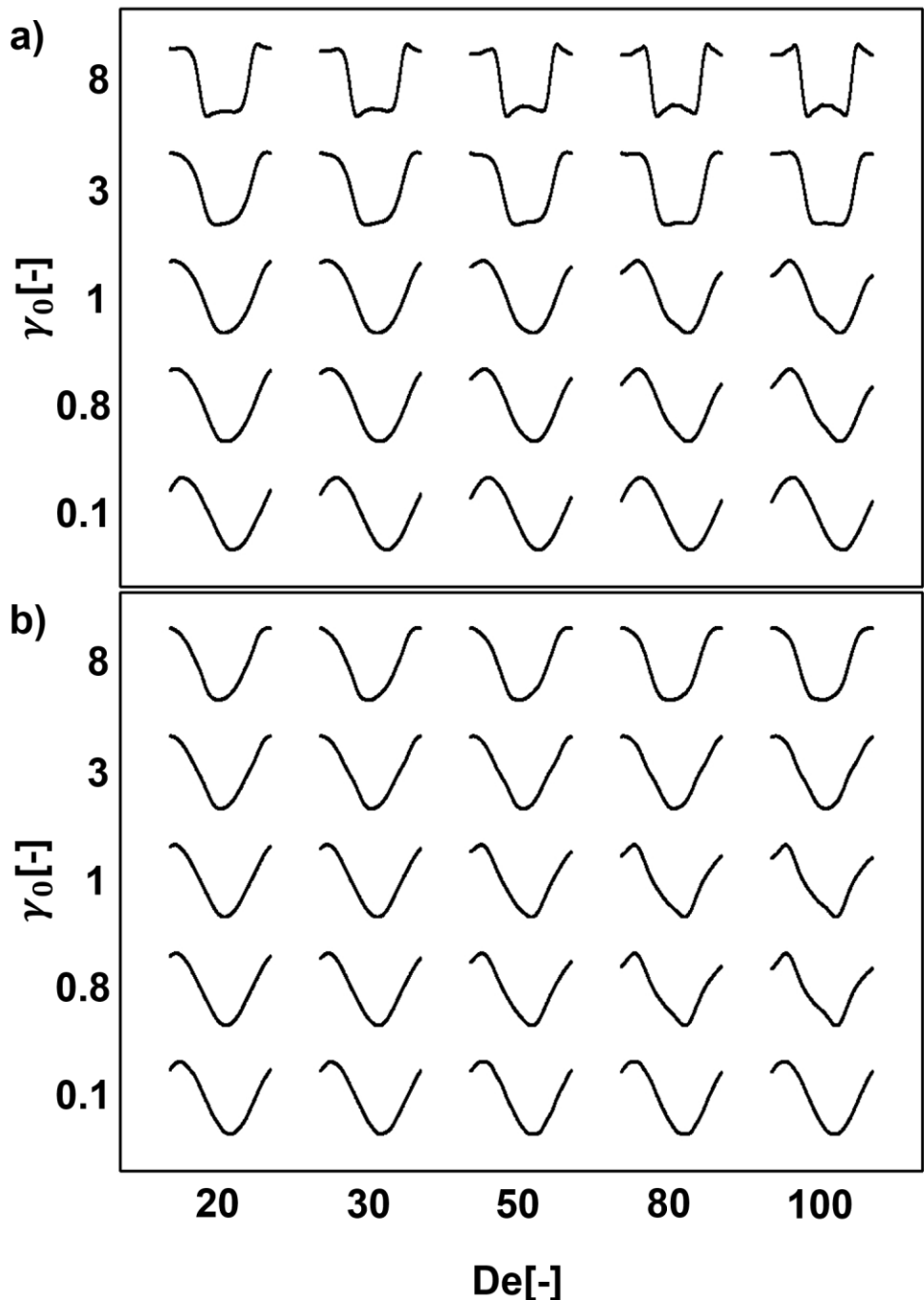


Fig. 3A-1 Normalized total stress with time in Pipkin space for a) soft and b) hard sphere systems at $\Gamma/\Gamma_{freezing} = 0.61$.

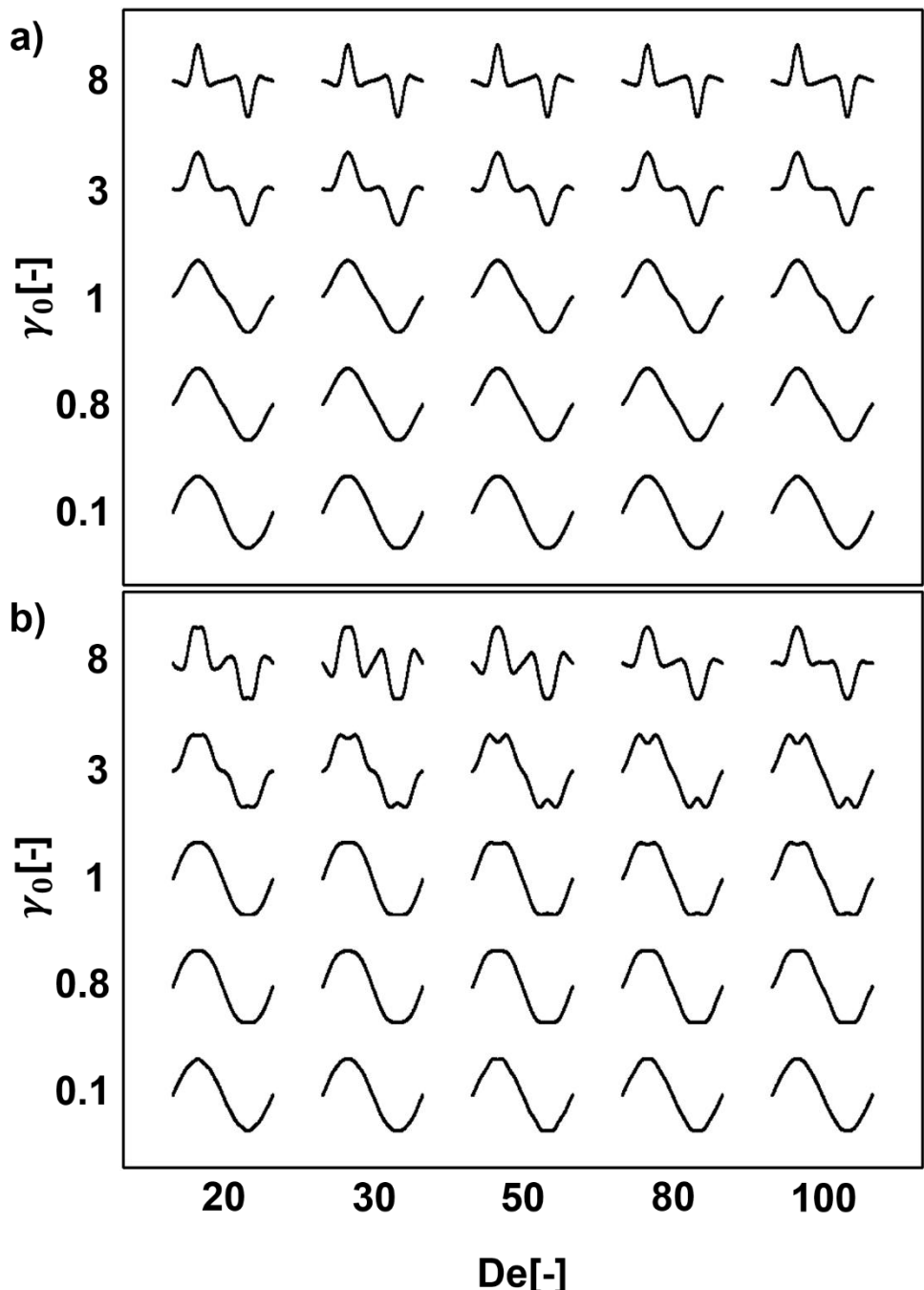


Fig. 3A-2 Normalized elastic stress with time in Pipkin space for a) soft and b) hard sphere systems at $\Gamma/\Gamma_{freezing} = 0.61$.

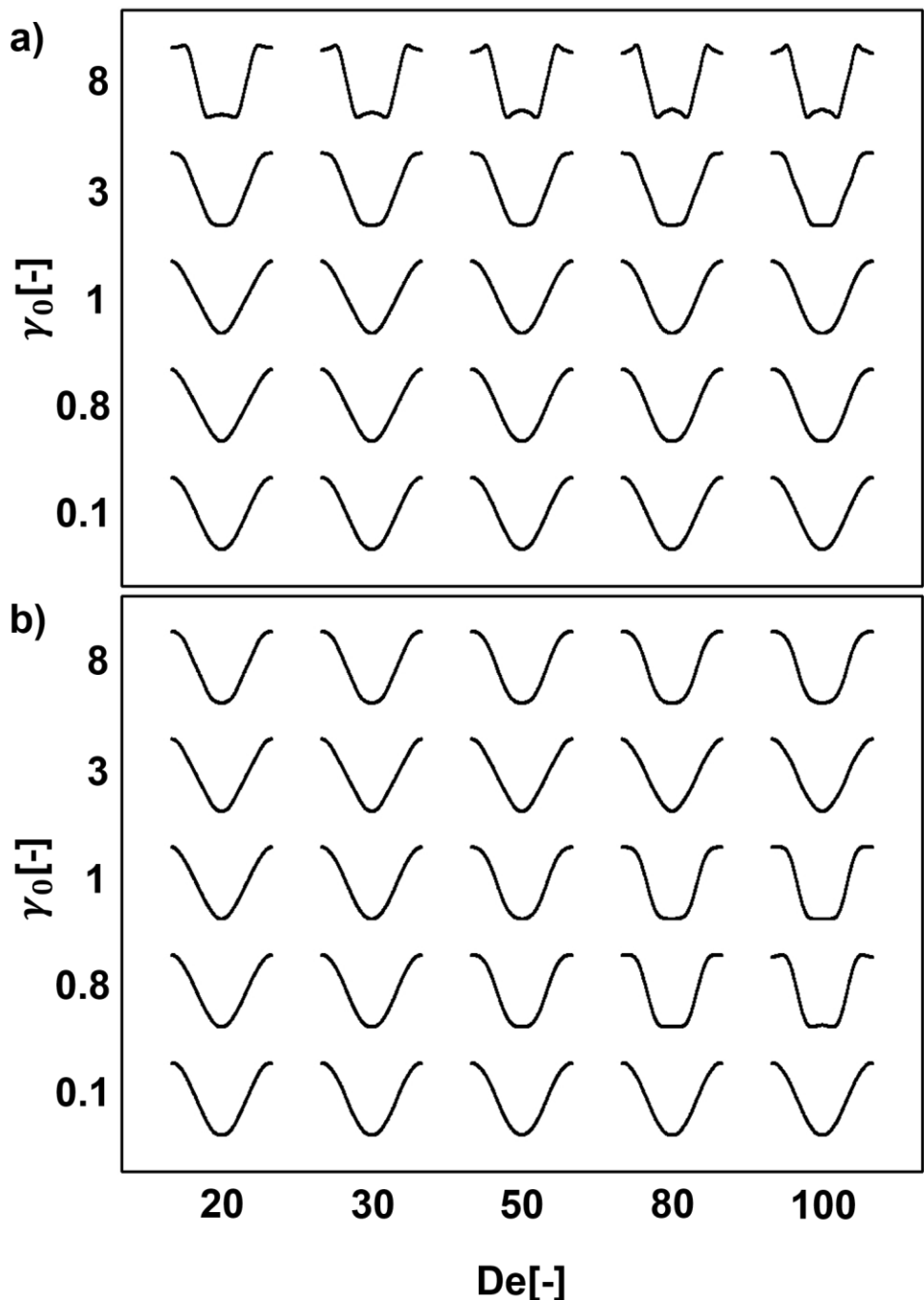


Fig. 3A-3 Normalized viscous stress with time in Pipkin space for a) soft and b) hard sphere systems at $\Gamma/\Gamma_{freezing} = 0.61$.

Appendix 3B

The difference in the maximum and minimum of excess entropy is plotted in Fig. 3B-1 and depth and width at different $\Gamma/\Gamma_{freezing}$ are plotted in Fig. 3B-2 for double peaks appearance condition. Here, PF is used, $De = 80$, and $\Gamma/\Gamma_{freezing} = 0.61, 0.71$ and 0.81 .

As $\Gamma/\Gamma_{freezing}$ increases, the difference in excess entropy decrease and it affects the γ_0 range of double peaks appearance and the value of depth. $\Gamma/\Gamma_{freezing}$ study also supports that double peaks are observed in systems when the structural difference between the maximum- and minimum-ordered states is large.

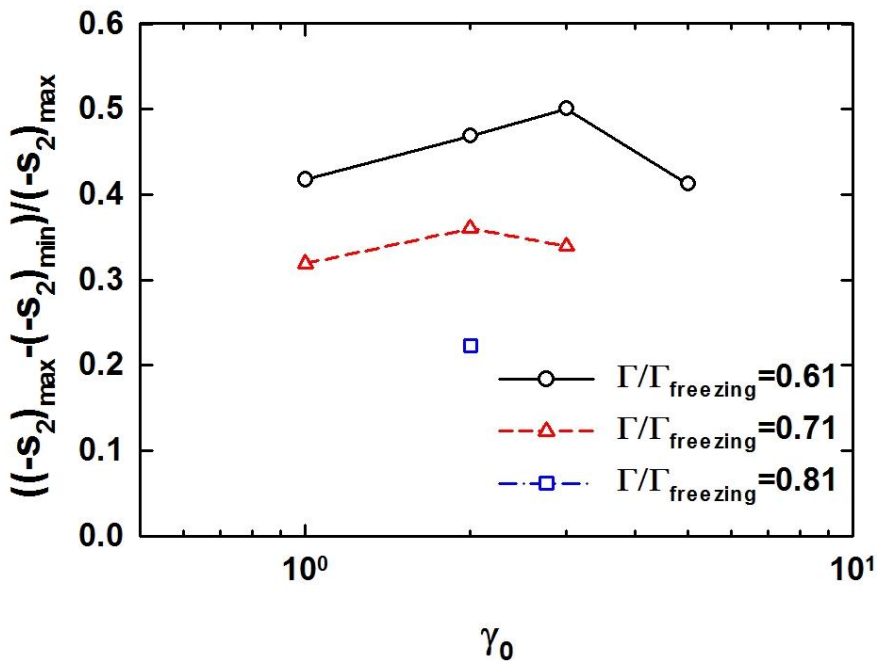


Fig. 3B-1 The difference in the maximum and minimum of excess entropy as a function of γ_0 at $\Gamma/\Gamma_{freezing} = 0.61, 0.71$ and 0.81 .

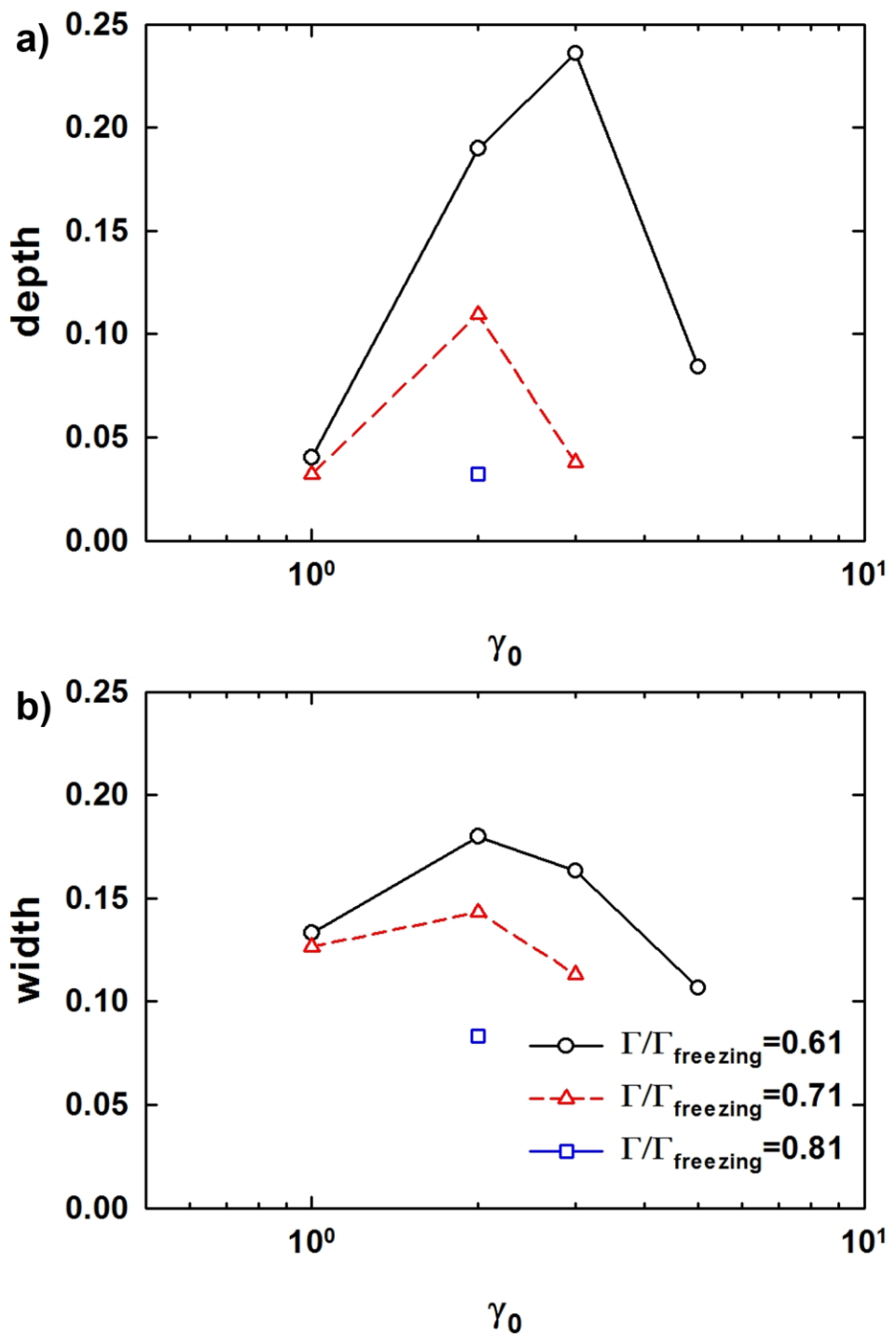


Fig. 3B-2 Double peaks a) depth and b) width at $De = 80$ as a function of γ_0 for PF at $\Gamma/\Gamma_{freezing} = 0.61, 0.71$ and 0.81 .

IV. Path-dependent work and stored energy in LAOS flow

4.1 Motivation and objectives

As mentioned in section 1.2.2, analysis methods for LAOS can be classified as analyzing in strain or strain rate domain and in the time domain. Analyzing oscillatory shear stress has been conducted over a decade. As many studies were carried out, the advantage and weaknesses of each method are also revealed. In stress decomposition method, which is a representative method for strain or strain rate domain, as shown in the previous chapter, its validity is argued due to discordance between stress and structure. In Fourier transform (FT) rheology, which is a representative method in time domain, the parameters from FT have no physical significance as FT simply decomposes stress signal. Moreover, the parameters from FT can be expanded infinitely, which requires a decision whether n^{th} order can affect the results or not.

In this chapter, firstly, we want to suggest a physics-based method for analyzing oscillatory shear stress by adopting the concept of energy. To do that, the inner area of Lissajous curves is related to work and stored energy. Second, to consider higher harmonics of the nonlinear regime with a simple method, only the integral of the area as time proceeds is accounted. Finally,

we try to relate rheological behavior and oscillatory shear stress with energy by applying this method to various model stress and simulation results.

4.2 Work and stored energy under oscillatory shear

Let us define strain and strain rate as $x = \gamma = \gamma_0 \sin \omega t$, $y = \dot{\gamma}/\omega = \gamma_0 \cos \omega t$ [Cho et al. (2005)]. It is well-known that the inner area of elastic Lissajous ($x - \sigma$ Lissajous) is related to work and the first harmonic loss modulus G_1'' [Ganeriwala and Rotz (1987), Dealy and Wissbrun (1990)]. The work generated during the time interval from t_1 to t_2 under oscillatory shear flow can be defined by Eq. (4-1). Here, the work done per unit volume is defined as W .

$$W = \int_{t_1}^{t_2} \sigma \dot{\gamma} dt \quad (4-1)$$

Substituting the oscillatory shear stress (Eq. (1-6)) into Eq. (4-1), W throughout one full cycle is given as follows.

$$\begin{aligned} W_{full} &= \int_0^{2\pi/\omega} \sigma \dot{\gamma} dt \\ &= \gamma_0 \omega \left(\sigma_1 \cos \delta_1 \int_0^{2\pi/\omega} \sin \omega t \cos \omega t dt + \sigma_1 \sin \delta_1 \int_0^{2\pi/\omega} \cos^2 \omega t dt \right. \\ &\quad \left. + \sigma_3 \cos \delta_3 \int_0^{2\pi/\omega} \sin 3\omega t \cos \omega t dt + \right. \\ &\quad \left. \sigma_3 \cos \delta_3 \int_0^{2\pi/\omega} \cos 3\omega t \cos \omega t dt + \dots \right) \\ &= \frac{\gamma_0 \omega \sigma_1 \sin \delta_1}{2} \int_0^{2\pi/\omega} 1 dt = \gamma_0 \sigma_1 \sin \delta_1 \pi \end{aligned} \quad (4-2)$$

When oscillatory shear stress is linear, the relation of $W_{full} = \gamma_0^2 \pi G_1''$ is

fulfilled. Therefore, the work throughout one full cycle depends only on the terms of the first harmonic such as σ_1 , δ_1 or G'_1 . When strain at t_1 and t_2 are defined as γ_1 and γ_2 respectively, the area of $x - \sigma$ Lissajous during the time interval from t_1 to t_2 ($W = \int_{\gamma_1}^{\gamma_2} \sigma dx$) is identical to W obtained from Eq. (4-2) as $dx = \dot{y}dt$. Therefore, the area of $x - \sigma$ Lissajous curve and W can be interchangeable.

Meanwhile, when $y = \dot{y}/\omega = \gamma_0 \cos \omega t$ is defined, the inner area of viscous Lissajous ($y - \sigma$ Lissajous) is related to the first harmonic storage modulus G'_1 and this area is called stored energy [Ganeriwala and Rotz (1987)]. The stored energy during the time interval from t_1 to t_2 is given by Eq. (4-3). Here, the stored energy per unit volume is defined as E .

$$E = \int_{t_1}^{t_2} \sigma \gamma \omega dt \quad (4-3)$$

When substituting the oscillatory shear stress (Eq. (1-6)) into Eq. (4-3), E throughout one cycle is given by Eq. (4-4).

$$\begin{aligned} E_{full} &= \int_0^{2\pi/\omega} \sigma \gamma \omega dt \\ &= \gamma_0 \omega \left(\begin{array}{l} \sigma_1 \cos \delta_1 \int_0^{2\pi/\omega} \sin^2 \omega t dt + \sigma_1 \sin \delta_1 \int_0^{2\pi/\omega} \cos \omega t \sin \omega t dt \\ + \sigma_3 \cos \delta_3 \int_0^{2\pi/\omega} \sin 3\omega t \sin \omega t dt + \\ \sigma_3 \cos \delta_3 \int_0^{2\pi/\omega} \cos 3\omega t \sin \omega t dt + \dots \end{array} \right) \\ &= \frac{\gamma_0 \omega \sigma_1 \cos \delta_1}{2} \int_0^{2\pi/\omega} 1 dt = \gamma_0 \sigma_1 \cos \delta_1 \pi \end{aligned} \quad (4-4)$$

When the stress is linear, the relation of $E_{full} = \gamma_0^2 \pi G'_1$ is fulfilled. Similar to W , E throughout one full cycle depends only on the first harmonic. When

strain rate at t_1 and t_2 are defined as $\dot{\gamma}_1$ and $\dot{\gamma}_2$ respectively, the area of $y - \sigma$ Lissajous during the time interval from t_1 to t_2 ($E = \int_{\dot{\gamma}_1}^{\dot{\gamma}_2} -\sigma dy$) is identical to E from Eq. (4-4) as $dy = -\gamma \omega dt$. Therefore, the area of $y - \sigma$ Lissajous curve and E can be interchangeable.

In the case of perfectly elastic solid ($\sigma = G\gamma = G\gamma_0 \sin \omega t$, where G is elastic modulus), the inner area of $x - \sigma$ Lissajous is zero and that of $y - \sigma$ Lissajous is $G\gamma_0^2 \pi$. In the case of purely viscous liquid ($\sigma = \eta\dot{\gamma} = \eta\gamma_0 \omega \cos \omega t$, where η is viscosity), the inner area of $x - \sigma$ Lissajous is $\eta\gamma_0^2 \omega \pi$ and that of $y - \sigma$ Lissajous is zero. As the inner area of $x - \sigma$ Lissajous is zero for a perfectly elastic solid, is related to viscosity for a purely viscous liquid, and is related to G''_1 for the viscoelastic fluid, it can be thought that the area or W has a viscous character of the material. Likewise, as the inner area of $y - \sigma$ Lissajous is zero for a purely viscous liquid, is related to elastic modulus for perfectly elastic solid, and is related to G'_1 for the viscoelastic fluid, it can be thought that the area or E has an elastic character of the material. Therefore, throughout one cycle, W represents the viscous characteristic and E represents the elastic characteristic of the material.

As the integration of higher order terms except for $\cos^2 \omega t$ (Eq. 4-2) or $\sin^2 \omega t$ (Eq. 4-4) term is always zero after one cycle, theoretically, inner areas in $x - \sigma$ and $y - \sigma$ plot even in nonlinear regime is identical to those in the linear regime. Therefore, higher order terms in oscillatory shear stress do not affect the inner area or W (or E) throughout one cycle.

4.3 Work and stored energy of model stress

To investigate this characteristics further, a model stress (Eq. (4-5)), which has up to the third harmonic, is analyzed as an illustration. Here, σ_3 is set $0.2\sigma_1$ and δ_1 is fixed to $\pi/3$, for simplicity.

$$\sigma = \sigma_1 \left[\left(\sqrt{3} \sin \omega t / 2 + \cos \omega t / 2 \right) + 0.2 (\sin 3\omega t \cos \delta_3 + \cos 3\omega t \sin \delta_3) \right] \quad (4-5)$$

The shape change of $x - \sigma$ and $y - \sigma$ Lissajous curves with varying δ_3 is given in Fig. 4-1.

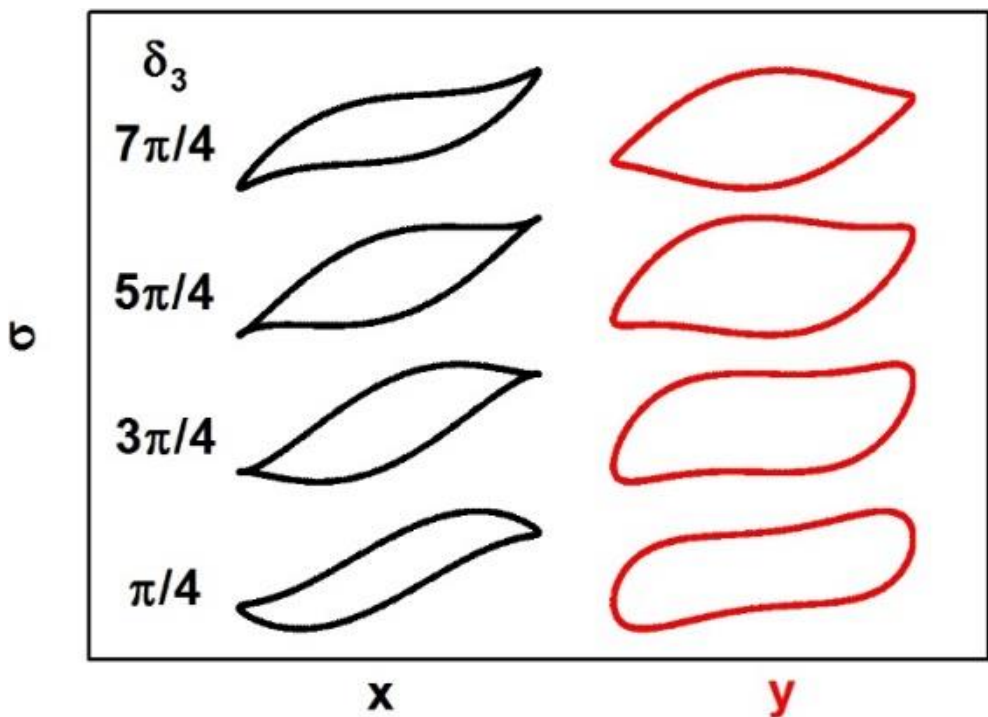


Fig. 4-1 The shape change of $x(\gamma) - \sigma$ and $y(\dot{\gamma}/\omega) - \sigma$ Lissajous with varying δ_3 in Eq. (4-5).

As shown in Fig. 4-1, the stress shape in Lissajous depends on δ_3 . However, the inner areas of the Lissajous curve (Eq. (4-2)), (Eq. (4-4)) are not dependent upon δ_3 because σ_1 and δ_1 are fixed. Therefore, it is not enough to merely check the results at time $2\pi/\omega$ where one cycle is completed and the effect of higher order terms is vanished. As an alternative, the area change in Lissajous curve needs to be concerned as time proceeds to elucidate the effect of higher order terms in nonlinear stress and to understand the effect of elastic and viscous contributions.

To confirm the effect of higher order terms, stress models with varying higher harmonics are analyzed. W and E during the cycle are calculated and analyzed. At first, to investigate the effect of higher order terms in phase angle, a model stress (Eq. (4-6)) is used and δ_3 is varied. Then, the area change of $x - \sigma$ and $y - \sigma$ Lissajous is probed as time proceeds.

$$\sigma = \sigma_1 \left[(\sin \omega t \cos \delta_1 + \cos \omega t \sin \delta_1) + k (\sin 3\omega t \cos \delta_3 + \cos 3\omega t \sin \delta_3) \right] \quad (4-6)$$

Here, δ_1 and k are fixed as $\pi/6$ and 0.5, respectively. The effects of δ_3 on the area of $x - \sigma$ and $y - \sigma$ Lissajous is shown in Fig. 4-2, which plots accumulated $W (\int_0^t \sigma \dot{\gamma} dt)$ or $E (\int_0^t \sigma \gamma \omega dt)$ as time proceeds. W , E , W_{full} , and E_{full} indicate the area of $x - \sigma$ Lissajous during the cycle, the area of $y - \sigma$ Lissajous during the cycle, the W throughout one full cycle as in equation (Eq. (4-2)), and the E throughout one full cycle as in equation (Eq. (4-4)), respectively. W_{full} and E_{full} are $\gamma_0^2 \pi G_1''$ and $\gamma_0^2 \pi G_1'$, respectively,

regardless of higher order terms. The ordinate W or E is normalized by W_{full} or E_{full} , and $t/(2\pi/\omega) = 1$ indicates the time when one cycle is completed.

W and E show different paths during the cycle depending on δ_3 . However, they are independent of δ_3 at the point of half cycle and one full cycle. This result proves that higher harmonic terms have no effect on the area of Lissajous throughout one complete cycle. Rather, they affect only on the work and energy during the cycle. As δ_3 increases, in $x - \sigma$ Lissajous, the degree of fluctuation decreases. On the other hand, in $y - \sigma$ Lissajous, the reverse is observed. As confirmed in the Eq. (4A-3) and (4A-7) of Appendix 4A, it is enough to investigate only the first half cycle.

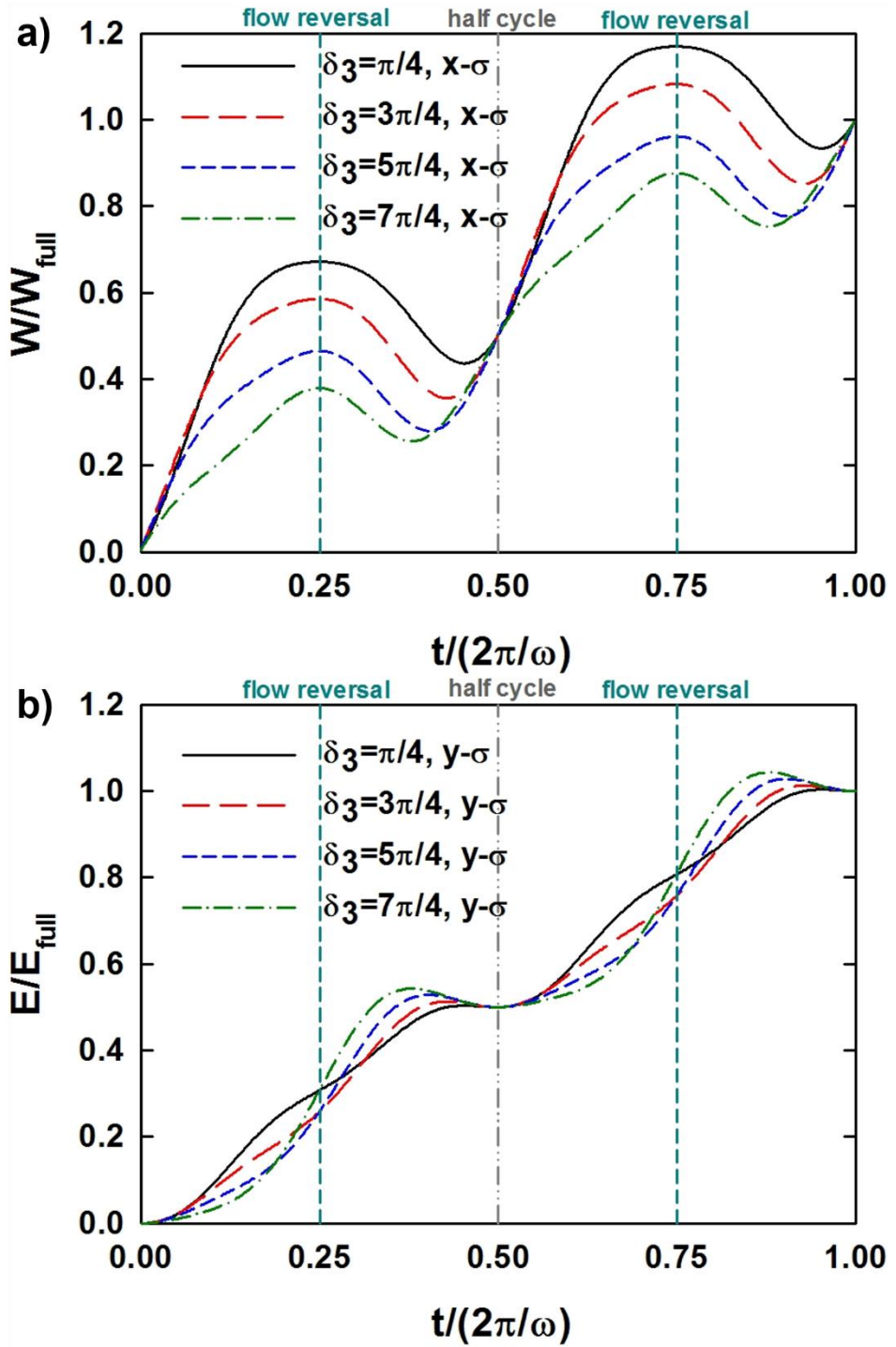


Fig. 4-2 Areas of a) $x(\gamma) - \sigma$ Lissajous, b) $y(\dot{\gamma}/\omega) - \sigma$ Lissajous vs. time as δ_3 changes.

In Fig. 4-3, the value of k , which is the ratio of σ_3 to σ_1 , is also varied. Here, δ_1 and δ_3 are fixed as $\pi/6$ and 0π , respectively. Same with previous results, the areas of $x - \sigma$ and $y - \sigma$ Lissajous throughout one cycle are independent of k . However, the W and E followed different paths during the cycle depending on δ_3 . The fluctuation of W and E was observed even in the linear regime when $k = 0$ as reported previously [Giacomin et al. (2012)].

Based on above model tests, it is confirmed that the area of the Lissajous curve throughout one full cycle and W_{full} and E_{full} depend only on γ_0 , σ_1 , and δ_1 . The third harmonics terms (σ_3 , δ_3) have an effect on W and E during the cycle, but not at the point of half or one full cycle. Likewise, the higher harmonics terms (larger than 3) have an effect on W and E during the cycle, not at the point of half or one cycle. As the work is path dependent, it is concluded that it is required to probe the paths of W and E during the cycle to properly analyze the nonlinear stress which includes higher order terms. Now we will apply this concept to some constitutive equations.

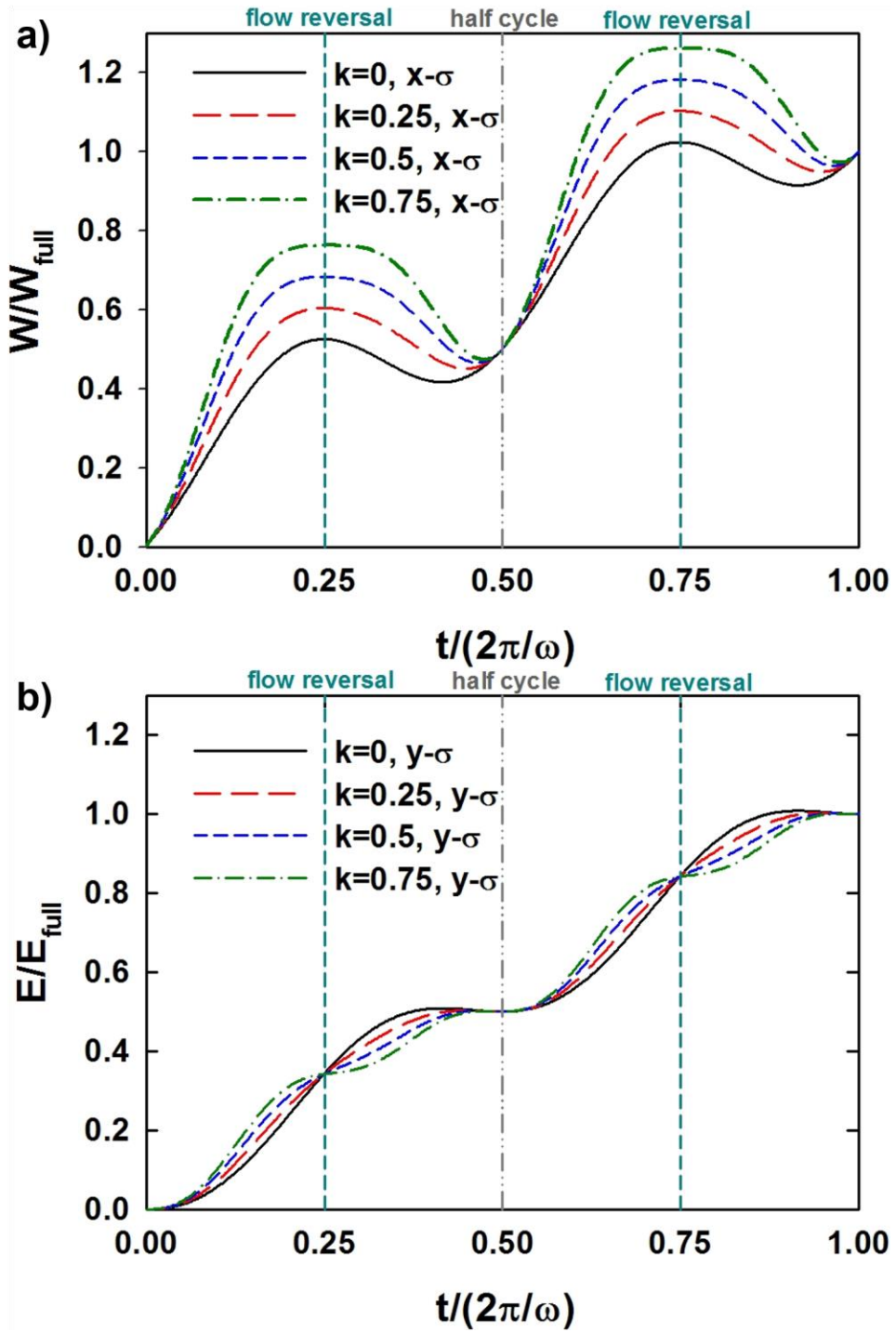


Fig. 4-3 Areas of a) $x(\gamma) - \sigma$ Lissajous, b) $y(\dot{\gamma}/\omega) - \sigma$ Lissajous vs. time as k changes.

4.4 Application to constitutive equations

4.4.1 Purely viscous liquid and perfectly elastic solid

First, purely viscous liquid and perfectly elastic solid are considered [Ewoldt *et al.* (2008)]. The stress of a purely viscous liquid is related only to strain rate, and the stress of a perfectly elastic solid is related only to strain. Purely viscous liquid can be modeled as in Eq. (4-7).

$$\sigma = g(\dot{\gamma})\dot{\gamma}, g(\dot{\gamma}) = \eta_0 \pm \eta_\beta \left(\frac{\dot{\gamma}}{\dot{\gamma}^*} \right)^2 \quad (4-7)$$

Here, $g(\dot{\gamma})$ is the nonlinear viscous coefficient and $\dot{\gamma}^*$ is a critical strain rate where the nonlinear effect begins to occur. When the sign of Eq. (4-7) is positive, it predicts shear thickening, and it predicts shear thinning when the sign is negative. In this study, η_0 is $1 \text{ Pa} \cdot \text{s}$ and $\dot{\gamma}^*$ is 1 s^{-1} , for simplicity. η_β is $0.5 \text{ Pa} \cdot \text{s}$ for shear thickening and η_β is $-0.1 \text{ Pa} \cdot \text{s}$ for shear thinning.

Similar to the purely viscous model, perfectly elastic models is expressed as follows.

$$\sigma = f(\gamma)\gamma, f(\gamma) = G_0 \pm G_\beta \left(\frac{\gamma}{\gamma^*} \right)^2 \quad (4-8)$$

Here, $f(\gamma)$ is the nonlinear elastic coefficient and γ^* is the critical strain where the nonlinear effect begins to occur. When the sign of Eq. (4-8) is positive, it predicts strain stiffening, and it predicts strain softening when the sign is negative. Similarly, G_0 is 1 Pa and γ^* is 1 for both cases. G_β is

0.5 Pa for strain stiffening and G_β is -0.1 Pa for strain softening. The parameters are the same and correspond to the purely viscous model.

In this section, a total cycle is divided into 24 sections with the same time interval. And W or E at each section is normalized by W_{full} or E_{full} . For example, in Fig. 4-4, the n value of ordinate corresponds to W or E during the time interval, $(n-1)/24$ cycle $< t/(2\pi/\omega) < n/24$ cycle, normalized by W_{full} or E_{full} . As W and E after half cycle are the same as the one before half cycle, only the results before half cycle are provided.

Fig. 4-4 shows the normalized W at each section for the purely viscous liquid. Here, a half cycle is divided into two parts based on the point where strain is $0.5\gamma_0$ (2/24 cycle, 10/24 cycle). One is low strain area ($0/24$ cycle $< t/(2\pi/\omega) < 2/24$ cycle, $10/24$ cycle $< t/(2\pi/\omega) < 12/24$ cycle; $n = 1, 2, 11, 12$) and the other is high strain area ($2/24$ cycle $< t/(2\pi/\omega) < 10/24$ cycle; $n = 3 \sim 10$). Here, the low strain area is labeled as A, and the high strain area is labeled as B.

In all cases, symmetry is observed with respect to the point of flow reversal (FR). For purely viscous thickening liquid, as γ_0 increases, W in section A increases and W in B decreases. For purely viscous thinning liquid, as γ_0 increases, W in section A decreases and W in B increases. And this trend does not change with a different parameter set.

When relating W to the amplitude of strain rate, normalized W in section B decreases with the increase in γ_0 for shear thickening liquid. And normalized W in section A increases with the increase in γ_0 . The structure that induces shear thickening seems to interrupt the flow when the strain rate is high, which makes the work in section A increase. In this case, normalized W near FR decreases. Therefore, shear thickening in purely viscous liquid appears when W in the nonlinear regime is larger than that in the linear regime in the high strain rate region (section A).

On the contrary, for shear thinning liquid, as γ_0 increases, normalized W in low strain rate area (section B) increases, and normalized W in high strain rate area (section A) decreases. In this case, the structure hardly interrupts the flow when strain rate is high. Thus, shear thinning in purely viscous liquid appears when W in the nonlinear regime is smaller than that in the linear regime in high strain rate region (section A). This implies that the change of W during the cycle can be related to the characteristic which is involved with structure.

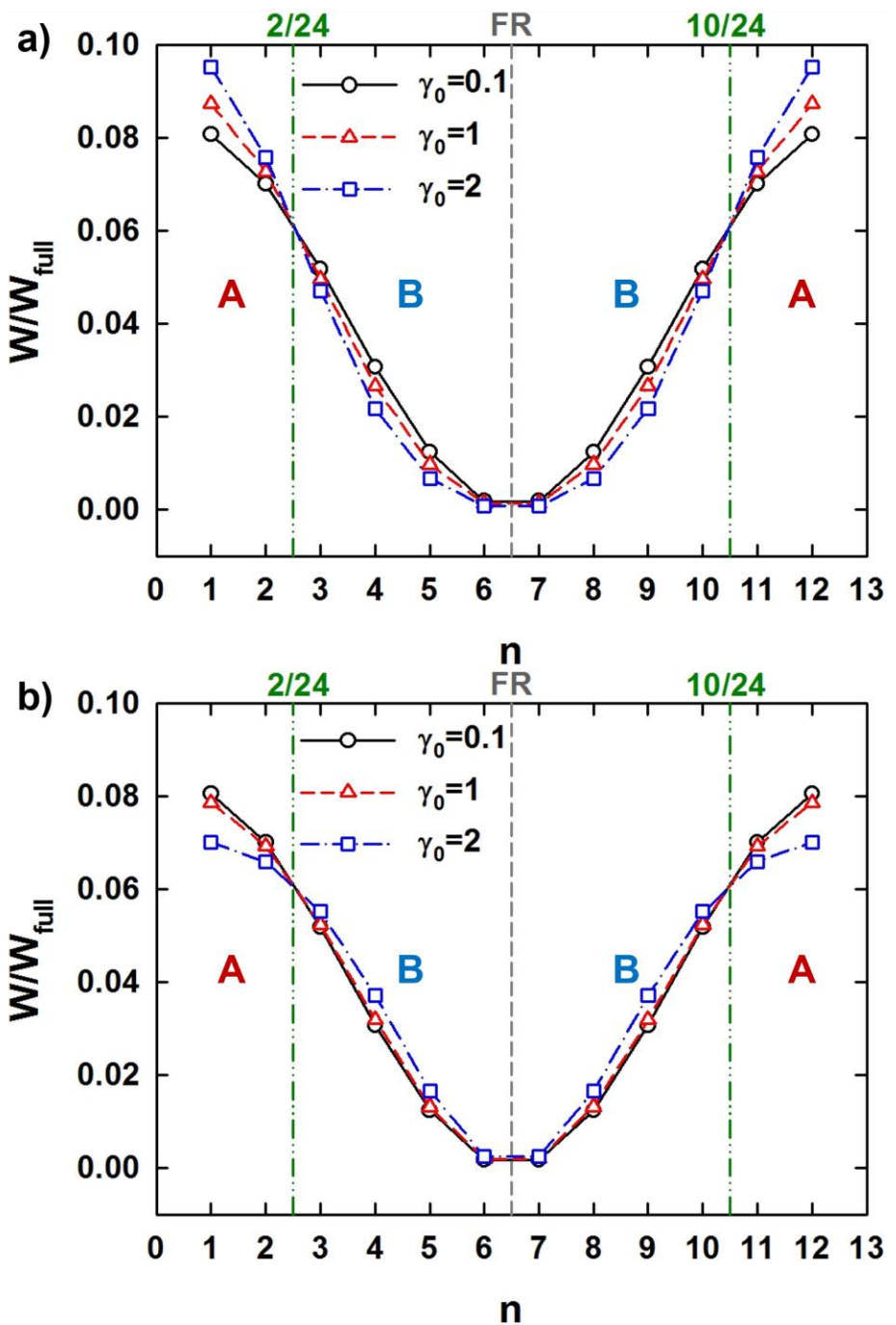


Fig. 4-4 Normalized W at each section in half cycle for a) shear thickening, b) shear thinning liquid. n in the horizontal axis means the time interval ($n-1)/24$ cycle $< t/(2\pi/\omega) < n/24$ cycle.

Fig. 4-5 shows normalized E for the perfectly elastic solid. Here, a half cycle is divided into two parts based on the point where strain rate is $0.5\gamma_0\omega$ (4/24 cycle, 8/24 cycle). One is high strain rate area ($0/24 \text{ cycle} < t/(2\pi/\omega) < 4/24 \text{ cycle}$, $8/24 \text{ cycle} < t/(2\pi/\omega) < 12/24 \text{ cycle}$; $n = 1 \sim 4, 9 \sim 12$) and the other is low strain rate area ($4/24 \text{ cycle} < t/(2\pi/\omega) < 8/24 \text{ cycle}$; $n = 5 \sim 8$). High strain rate area is labeled as A', and low strain rate area is labeled as B'.

As in W , a symmetry is observed with respect to flow reversal (FR). For perfectly elastic stiffening solid, E in section A' decreases and E in section B' increases as γ_0 increases. For perfectly elastic softening solid, however, E in section A' increases and E in section B' decreases with the increase in γ_0 . Similar to the purely viscous liquid, this trend does not change with a different parameter set. Therefore, strain stiffening in perfectly elastic solid appears when stored energy in the nonlinear regime is larger than that in the linear regime in the high strain region (section B'). And strain softening in perfectly elastic solid appears when the stored energy in the nonlinear regime is smaller than that in the linear regime in the high strain region (section B'). Both W and E show the possibility that the systems with different rheological properties can be analyzed in terms of work and stored energy. This method is unique and useful in that the oscillatory shear stress can be analyzed by using the concept of work and energy.

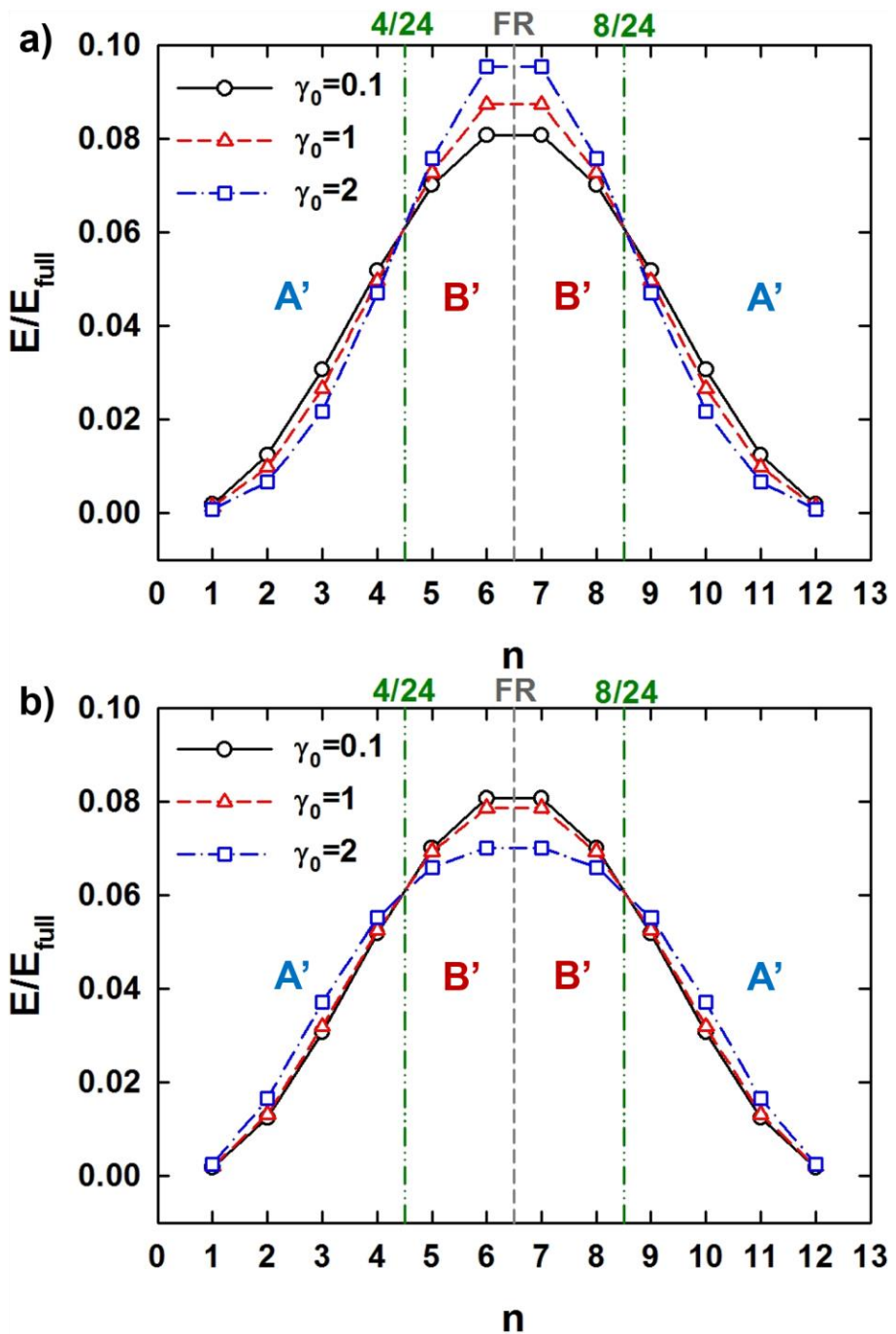


Fig. 4-5 Normalized E at each section in half cycle for a) strain stiffening, b) strain softening solid. n in the horizontal axis means the time interval $(n-1)/24$ cycle $< t/(2\pi/\omega) < n/24$ cycle.

4.4.2 Giesekus model

Giesekus model can be expressed as follows [Bird *et al.* (1987)].

$$\begin{aligned}\boldsymbol{\sigma} &= \boldsymbol{\sigma}_s + \boldsymbol{\sigma}_p, \\ \boldsymbol{\sigma}_s &= \eta_s \dot{\gamma}, \\ \boldsymbol{\sigma}_p + \lambda_1 \boldsymbol{\sigma}_{p(1)} + \alpha \frac{\lambda_1}{\eta_p} \{ \boldsymbol{\sigma}_p \cdot \boldsymbol{\sigma}_p \} &= \eta_p \dot{\gamma}. \end{aligned}\tag{4-9}$$

Here, σ_s , η_s , σ_p , λ_1 , $\sigma_{p(1)}$, α , and η_p are the solvent stress tensor, solvent viscosity, polymer stress tensor, relaxation time, upper convected time derivative of polymer stress tensor, mobility factor, and polymer viscosity, respectively. In this study, η_s , λ_1 , η_p , and α are 0.01 Pa·s, 1 s, 10 Pa·s, and 0.3, respectively. ω ranges from 0.1 to 10 [Ewoldt *et al.* (2008), Rogers and Lettinga (2012)]. Deborah number is defined as $De = \lambda_1 \omega$, and De is the same as ω in this case.

Similar to Fig. 4-4 and 4-5, W and E in each section are traced in Fig. 4-6 for three different γ_0 when ω equals one. Different from pure materials, for viscoelastic fluid, the symmetry with respect to FR disappears. Normalized W before FR ($n = 1\sim 6$) decreases as γ_0 increases, while it increases after FR ($n = 7\sim 12$). Normalized E from 1 to 7 increases and that from 8 to 12 decreases as γ_0 increases.

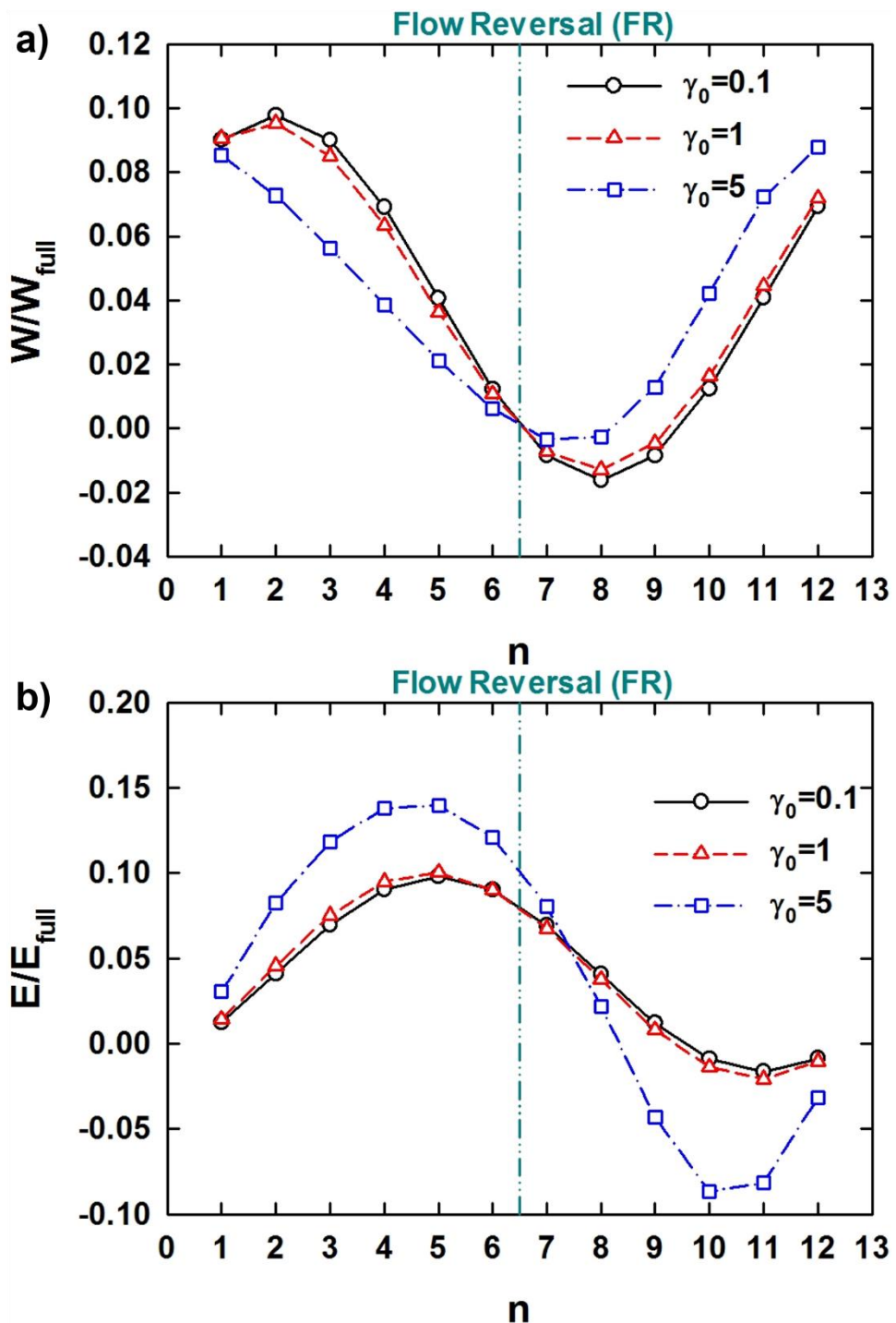


Fig. 4-6 a) Normalized W , b) normalized E at $\omega=1$. n in the horizontal axis means the time interval $(n-1)/24$ cycle $< t/(2\pi/\omega) < n/24$ cycle.

The effect of ω at small strain amplitude was also investigated. Fig. 4-7 shows W and E for three different ω . When $\omega (= De)$ is small (0.1s^{-1}), normalized W before and after FR is nearly symmetric with respect to FR as in the purely viscous liquid. However, as ω increases, the symmetry disappears. In purely viscous liquid, W of $0 < t/(2\pi/\omega) < \text{FR}$ and W of $\text{FR} < t/(2\pi/\omega) < \text{half cycle}$ have the same value and sign. On the contrary, in perfectly elastic solid, W of $0 < t/(2\pi/\omega) < \text{FR}$ and W of $\text{FR} < t/(2\pi/\omega) < \text{half cycle}$ have the same value and opposite sign (not shown in the figure). These results indicate that viscous character affects the symmetry with respect to FR and elastic character contributes to asymmetry in W . Therefore, it is thought that the extent of asymmetry in W with respect to FR is related to the degree of elasticity of a material. In Fig. 4-7a), the extent of asymmetry with respect to FR grows with the increase in ω because the system becomes more elastic.

When $\omega (= De)$ is large (10s^{-1}), normalized E before and after FR becomes nearly symmetric too with respect to FR as in the perfectly elastic material. However, as ω decreases, the symmetry disappears. Thus, elastic character contributes to symmetry with respect to FR, and viscous character contributes to asymmetry in the case of E . It is thought that the extent of asymmetry in E with respect to FR is related to the viscous character of the material. In Fig. 4-7b), the extent of asymmetry with respect to FR grows because the system becomes more viscous as ω decreases.

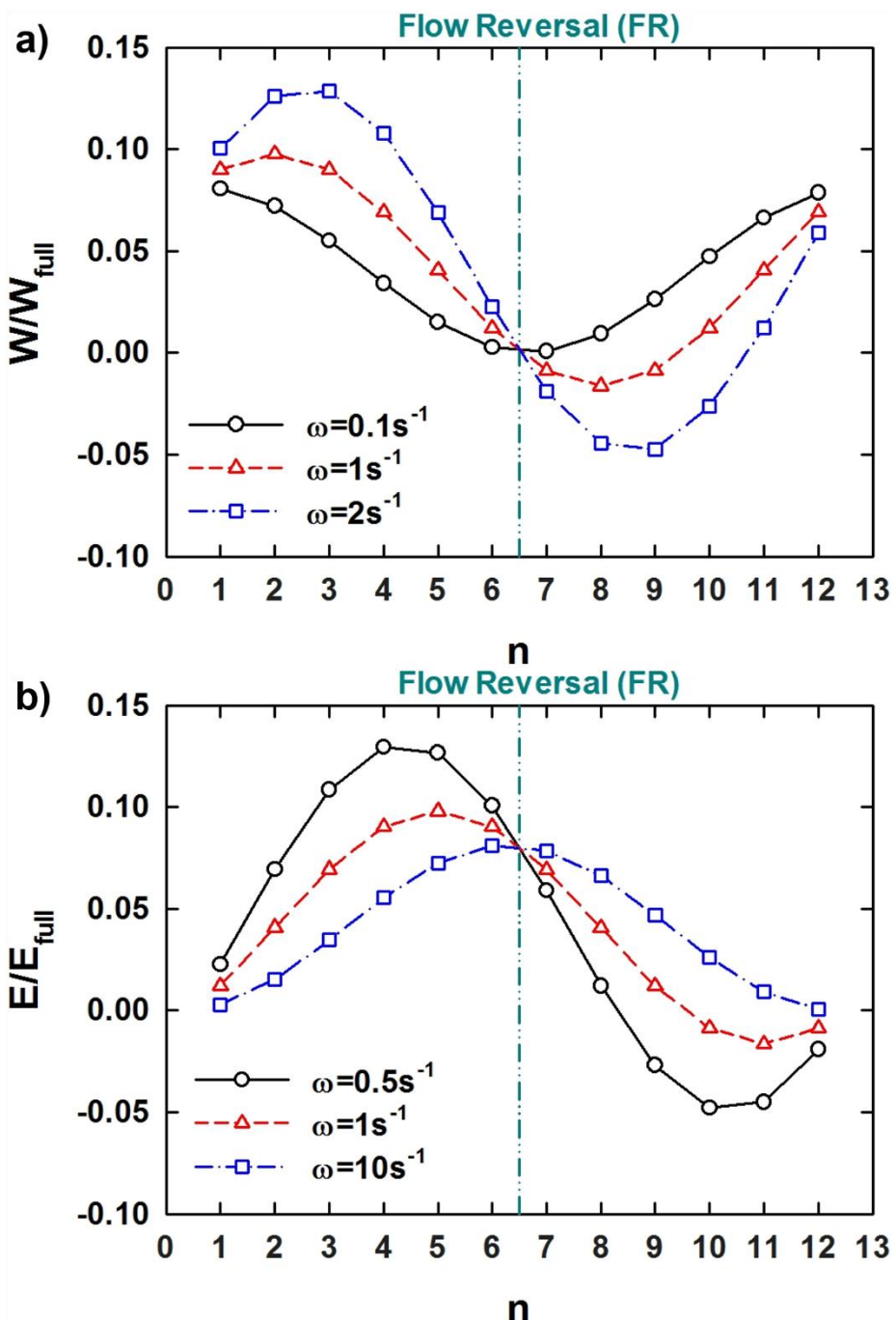


Fig. 4-7 a) Normalized W , b) normalized E at $\gamma_0=0.01$, which is included in the linear region. n in the horizontal axis means the time interval $(n-1)/24$ cycle $< t/(2\pi/\omega) < n/24$ cycle.

We now focus more on the extent of asymmetry. For this purpose, the sum of W or E before FR ($0 < t/(2\pi/\omega) < \text{FR}$) and after FR ($\text{FR} < t/(2\pi/\omega) < \text{half cycle}$) needs to be investigated. Here, the sum of W or E during the time interval $0 < t/(2\pi/\omega) < \text{FR}$ is defined as W_{FR} or E_{FR} . Fig 4-8. shows W_{FR} and E_{FR} normalized by W_{full} and E_{full} as a function of γ_0 at $\omega=0.5, 1, 2$. For reference, normalized W_{FR} and E_{FR} for the pure material are 0.25 due to the symmetry across the FR point.

Unlike the pure material, as γ_0 increases, W_{FR}/W_{full} shows a constant value followed by a decrease, and E_{FR}/E_{full} shows a constant value followed by an increase. As ω increases, W_{FR}/W_{full} becomes larger and E_{FR}/E_{full} becomes smaller. At small γ_0 , W_{FR}/W_{full} is larger than 0.25, which means W before FR ($0 < t/(2\pi/\omega) < \text{FR}$) is larger than W after FR ($\text{FR} < t/(2\pi/\omega) < \text{half cycle}$). As γ_0 increases, W_{FR}/W_{full} approaches 0.25, which means that W before FR and W after FR become comparable in the perspective of work. In other words, when γ_0 is large, due to the fast flow field, the structure is rearranged quickly to the inverse direction after FR, thus, the difference in two sections is scarcely observed.

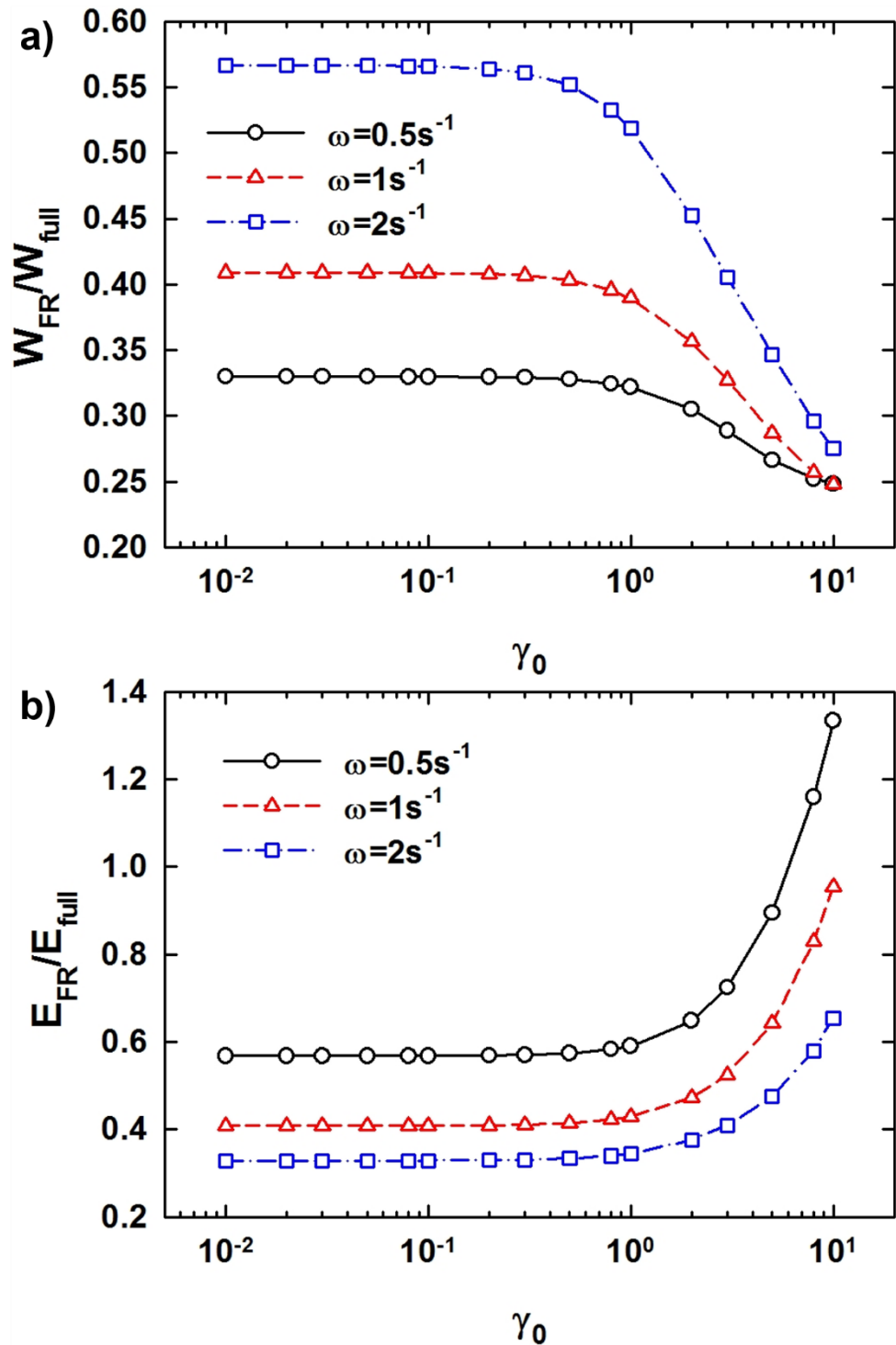


Fig. 4-8 a) W_{FR}/W_{full} , b) E_{FR}/E_{full} as a function of γ_0 at three ω .

Under oscillatory shear, W_{FR}/W_{full} and E_{FR}/E_{full} are given as Eq. (4A-4) and (4A-8) in Appendix 4A. In the linear regime with the first harmonic term only, $W_{FR}/W_{full} = \tan\delta_1/(2\pi) + 0.25$, and $E_{FR}/E_{full} = 1/(2\tan\delta_1\pi) + 0.25$. Thus, in the linear regime, W_{FR}/W_{full} and E_{FR}/E_{full} depend only on δ_1 . When $\tan\delta_1$ is near zero, the system is elastic, and when the value of $\tan\delta_1$ is very large, the system is viscous. Therefore, as ω increases, which means that the system becomes more elastic, W_{FR}/W_{full} increases and E_{FR}/E_{full} decreases in the linear regime.

Next, W_{FR}/W_{full} and E_{FR}/E_{full} in the nonlinear regime are investigated further. As verified in Eq. (4A-4), W_{FR}/W_{full} reflects the ratio of the elastic terms ($\sigma_n \cos\delta_n$) in the total stress and the first harmonic viscous term ($\sigma_1 \sin\delta_1$). As shown in Fig. 4-8, the system becomes more elastic and W_{FR}/W_{full} becomes larger with the increase in ω in the nonlinear regime. And W_{FR}/W_{full} decreases as γ_0 increases, because the contribution of the first harmonic viscous term in the total stress becomes significant.

Likewise, as explained in Eq. (4A-8), E_{FR}/E_{full} reflects the ratio of the viscous terms ($\sigma_n \sin\delta_n$) in the total stress and the first harmonic elastic term ($\sigma_1 \cos\delta_1$). Thus, when ω increases, the viscous contribution becomes smaller and so does E_{FR}/E_{full} in nonlinear regime. As γ_0 increases, E_{FR}/E_{full} increases because the effect of viscous terms of the total stress becomes significant. Therefore, W_{FR}/W_{full} and E_{FR}/E_{full} can reflect viscous and elastic contributions in total shear stress for any material. And

the γ_0 at which W_{FR}/W_{full} or E_{FR}/E_{full} deviates from constant is the point at which linear and nonlinear regime are separated.

In this section, the Giesekus model was analyzed in terms of W and E . For viscoelastic fluids, W and E during the cycle are asymmetric and the degree of asymmetry is related to the elastic and viscous characteristics of the material. In the nonlinear regime, W_{FR}/W_{full} and E_{FR}/E_{full} reflect the ratio of the elastic terms of the total stress and the viscous term of fundamental ω , and the ratio of the viscous terms in the total stress and the elastic term of fundamental ω , respectively. Based on this observation, it is concluded that the elastic and viscous characteristics can be explained in the perspective of work or energy even for the viscoelastic material, by using W and E at each section or W_{FR}/W_{full} and E_{FR}/E_{full} .

4.4.3 Bingham model

Finally, Bingham model that shows yield behavior is analyzed. This model is expressed by introducing recoverable strain concept as follows [Yoshimura and Prud'homme (1987)]:

$$\begin{aligned}\tau &= G\gamma_E \quad (|\gamma_E| < \gamma_y) \\ \tau &= G\gamma_E + \mu\dot{\gamma} \quad (|\gamma_E| = \gamma_y)\end{aligned}\quad (4-10)$$

Here, τ , G , μ , γ_E , $\dot{\gamma}$, and γ_y are the stress, elastic modulus, Bingham (plastic) viscosity, elastic (recoverable) strain, strain rate, and yield strain, respectively. G , μ , and γ_y are set as 1 Pa, 1 Pa·s, and 1, respectively, following previous paper [Rogers and Lettinga (2012)]. Yield stress (τ_y) has the relationship with γ_y as $\tau_y = G\gamma_y$ and yield stress is 1 Pa in this study. Similar to the previous paper, stress regime is divided into two sections, and work and stored energy are analyzed as functions of γ_0 .

Fig. 4-9 is $x - \sigma$ and $y - \sigma$ Lissajous plot for $\gamma_0=1, 5$, and 10 . Here, the vertical axis is the stress normalized by σ_0 . The horizontal axis of $x - \sigma$ Lissajous is the strain normalized by γ_0 , and that of $y - \sigma$ is the strain rate normalized by its amplitude ($\gamma_0\omega$). As time proceeds, in $x - \sigma$ Lissajous, the stress evolves to the clockwise direction, and in $y - \sigma$ Lissajous, it proceeds to the counter-clockwise direction. The filled symbol indicates the point of FR and the open symbol for $\gamma_0 = 5, 10$ is a yielding point, which shows a jump at each γ_0 .

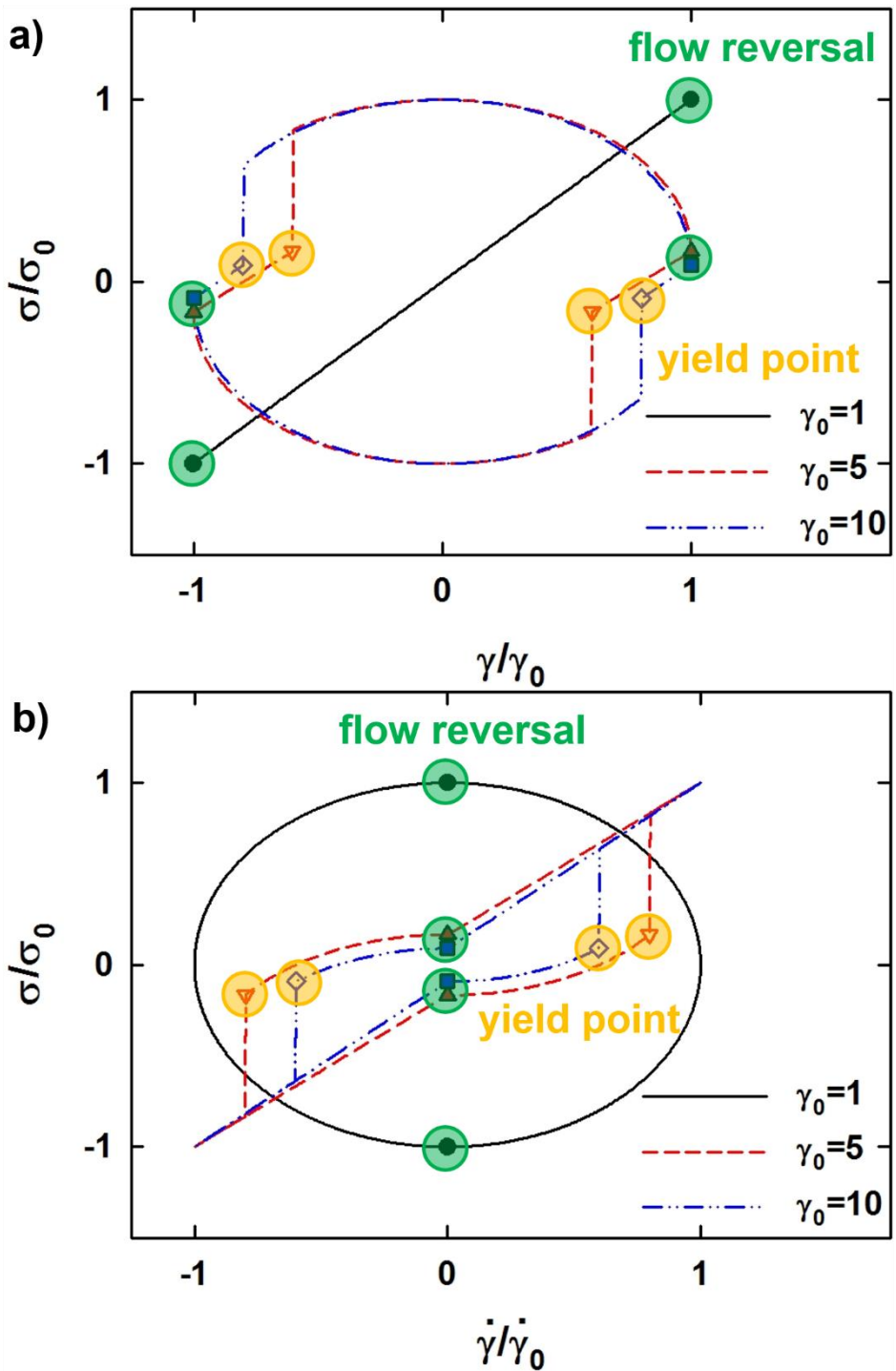


Fig. 4-9 a) $x(\gamma) - \sigma$, b) $y(\dot{\gamma}/\omega) - \sigma$ Lissajous plot of Bingham model as a function of γ_0 .

When γ_0 is less than one, as γ is always smaller than yield strain, the stress reacts elastically as cleared in Eq. (4-10). In this case, the yield is not observed, and there is no dissipated energy. For γ_0 larger than one, the stress reacts elastically after FR and it shows a viscous characteristic when the stress is larger than τ_y . In Fig. 4-9, the region from filled to open symbol corresponds to the elastic behavior and the rest of the region to viscous behavior. The first region is named as elastic σ part, and the other as viscous σ part. It is to be noted that they are a different concept from elastic and viscous stress in stress decomposition [Cho *et al.* (2005)].

When γ_0 is one, the shape of $x - \sigma$ Lissajous is a line and that of $y - \sigma$ Lissajous is an oval. When γ_0 is larger than one, in the elastic σ part in $x - \sigma$ Lissajous, the stress forms a line where its slope is modulus. On the other hand, in the viscous σ part, where the stress is larger than yield stress (1Pa), the stress behaves like a purely viscous liquid. In $y - \sigma$ Lissajous, the stress shows a curve in the elastic σ part while the viscous σ part shows a line, in which the slope is the Bingham viscosity.

Normalized W and E are given in Fig. 4-10 as the cycle proceeds. When γ_0 is one, W_{full} is zero because the stress is totally elastic, and W cannot be normalized. W of this condition is not included in Fig. 4-10a). The vertical lines with the tag of ' $\gamma_0 = 5$ yield' or ' $\gamma_0 = 10$ yield' indicate yield points, where the jump occurs, and the stress characteristic is changed from elastic to viscous. In other words, the region from FR to yield point at each γ_0 is the elastic σ part and the rest is the viscous σ part.

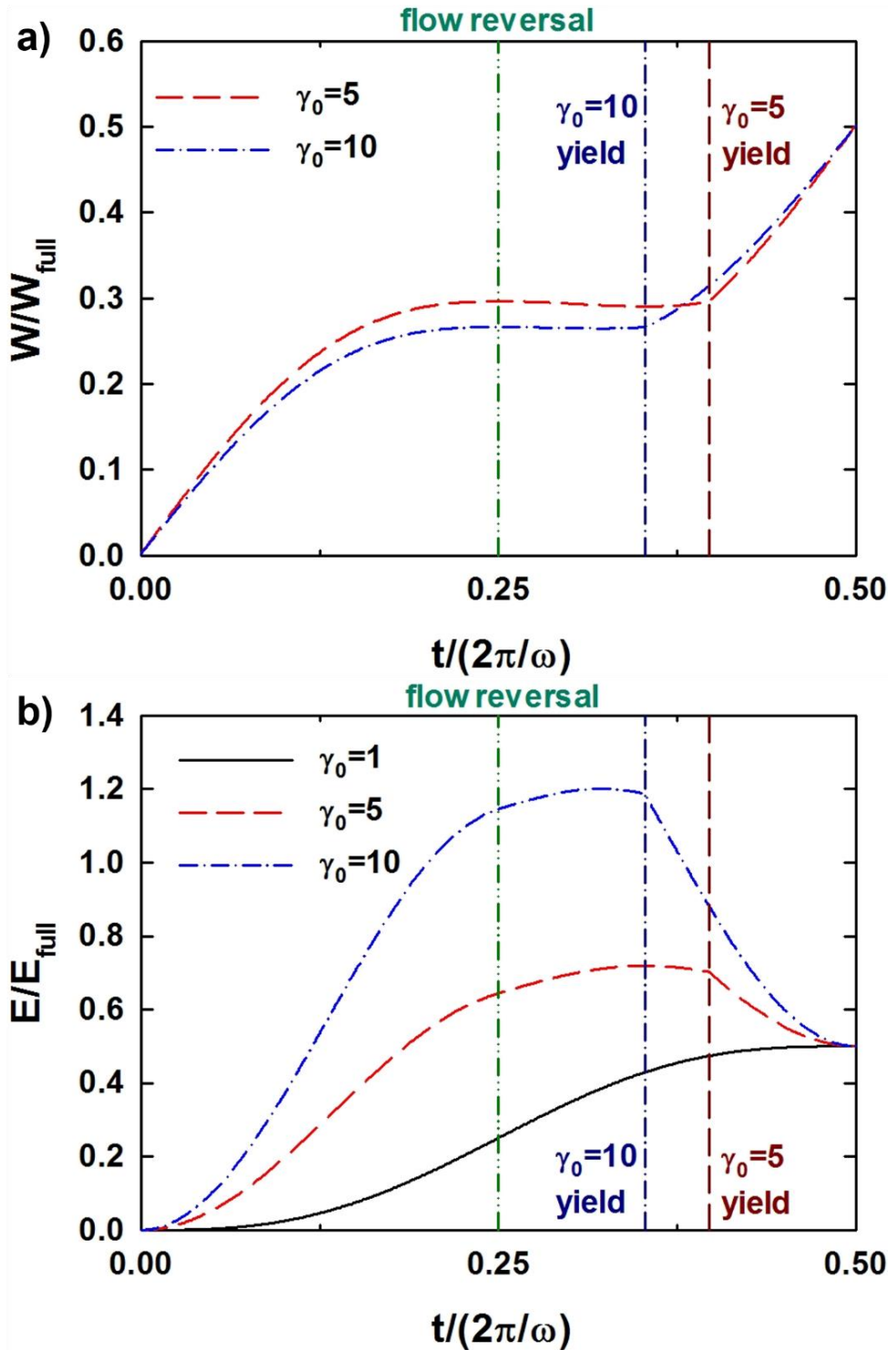


Fig. 4-10 a) W/W_{full} , b) E/E_{full} of Bingham model as time proceeds.

Normalized W and E do not change much in the elastic σ part (from FR to yield point), and the slope changes discontinuously at the yield point. Normalized W and E in the elastic and viscous σ parts as a function of γ_0 are plotted separately in Fig. 4-11. The subscripts *ela* and *vis* mean W or E in the elastic and viscous σ parts respectively. As the only half cycle is covered, the sum of W/W_{full} and E/E_{full} in the elastic and viscous σ parts is always 0.5.

For totally elastic case ($\gamma_0 = 1$), only elastic σ part contributes to E . Normalized E in the elastic and viscous σ parts are 0.5 and 0, respectively. When there exists yield ($\gamma_0 > 1$), W in the elastic σ part, where the stress is below τ_y , is zero, and W in the viscous σ part, where the stress exceeds τ_y , is 0.5. It means that W in the elastic σ part barely contributes to W during the whole cycle. This is related to the fact that the work done by the totally elastic model is always zero throughout one full cycle. As γ_0 increases, E in the elastic σ part decreases, and E in the viscous σ part increases. This may be interpreted such that viscous character becomes dominant as γ_0 increases. Unlike W in the elastic σ part, E in the viscous σ part is not zero and shows even larger contribution than E in the elastic σ part. In this sense, although E throughout one full cycle was named as stored energy [Ganeriwala and Rotz (1987)], it does not fully represent the elastic character and it is necessary to further discuss the meaning of E .

In this section, W and E of the yielding system have been separately analyzed by dividing the whole cycle into the elastic and viscous σ part. W of

each part matches the work for pure materials, whereas E of each part is intriguing compared to the stored energy for pure materials. Although the stress from the yielding system can be analyzed in terms of W or E , its significance needs to be studied further.

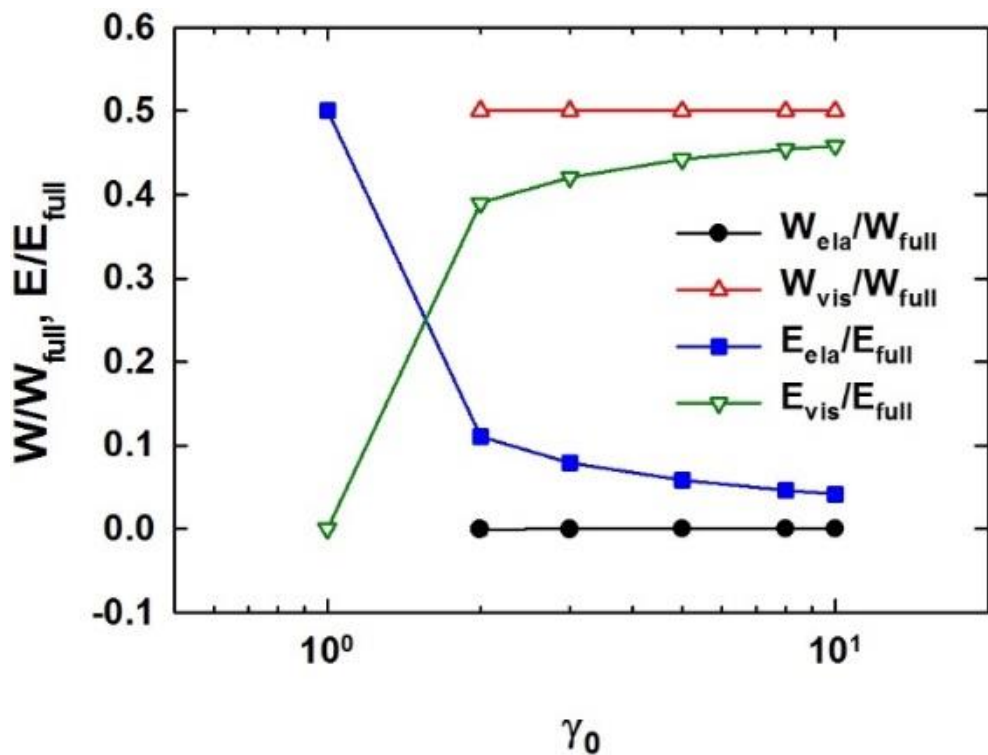


Fig. 4-11 Normalized W and E in the elastic and viscous σ parts as a function of γ_0 .

4.5 Application to BD simulation

This concept is also applied to oscillatory shear stress from Brownian dynamics simulation. By using PF method, hard sphere systems are described. In this section, $De = 20$ and $De = 80$ at $\Gamma/\Gamma_{freezing} = 0.61$ are analyzed. Fig. 4-12 shows strain sweep results for $De = 20, 80$. At $De = 20$, strain thinning behavior is observed, and at $De = 80$, weak strain overshoot behavior is observed and overshoot peak is shown at $\gamma_0 = 2$. γ_0 regime is divided by this overshoot peak. $0.8 < \gamma_0 < 2$ is before overshoot peak regime (in $0.8 < \gamma_0 < 2$, G'' increases) and $2 < \gamma_0 < 5$ is after overshoot peak regime (G'' at $\gamma_0 = 5$ is smaller than G'' at $\gamma_0 = 0.8$). For simplicity, before overshoot peak and after overshoot peak regime are denoted as INC and DEC regime, respectively.

Here, as G'' curve of two De are significantly different, W , which is closely related to G'' or viscous characteristic of material, is analyzed intensively. As suspension system is viscoelastic fluid, W is not symmetric with respect to FR. Thus, section A and B need to be subdivided into two sections. $0/24$ cycle $< t/(2\pi/\omega) < 2/24$ cycle, $2/24$ cycle $< t/(2\pi/\omega) < 6/24$ cycle, $6/24$ cycle $< t/(2\pi/\omega) < 10/24$ cycle, and $10/24$ cycle $< t/(2\pi/\omega) < 12/24$ cycle are defined as section A1, B1, B2, and A2, respectively. Similar to the sum of W during the time $0/24$ cycle $< t/(2\pi/\omega) < 6/24$ cycle (FR) being defined as W_{FR} , the sum of W during the each section is defined as W_{A1} , W_{B1} , W_{B2} , and W_{A2} , respectively.

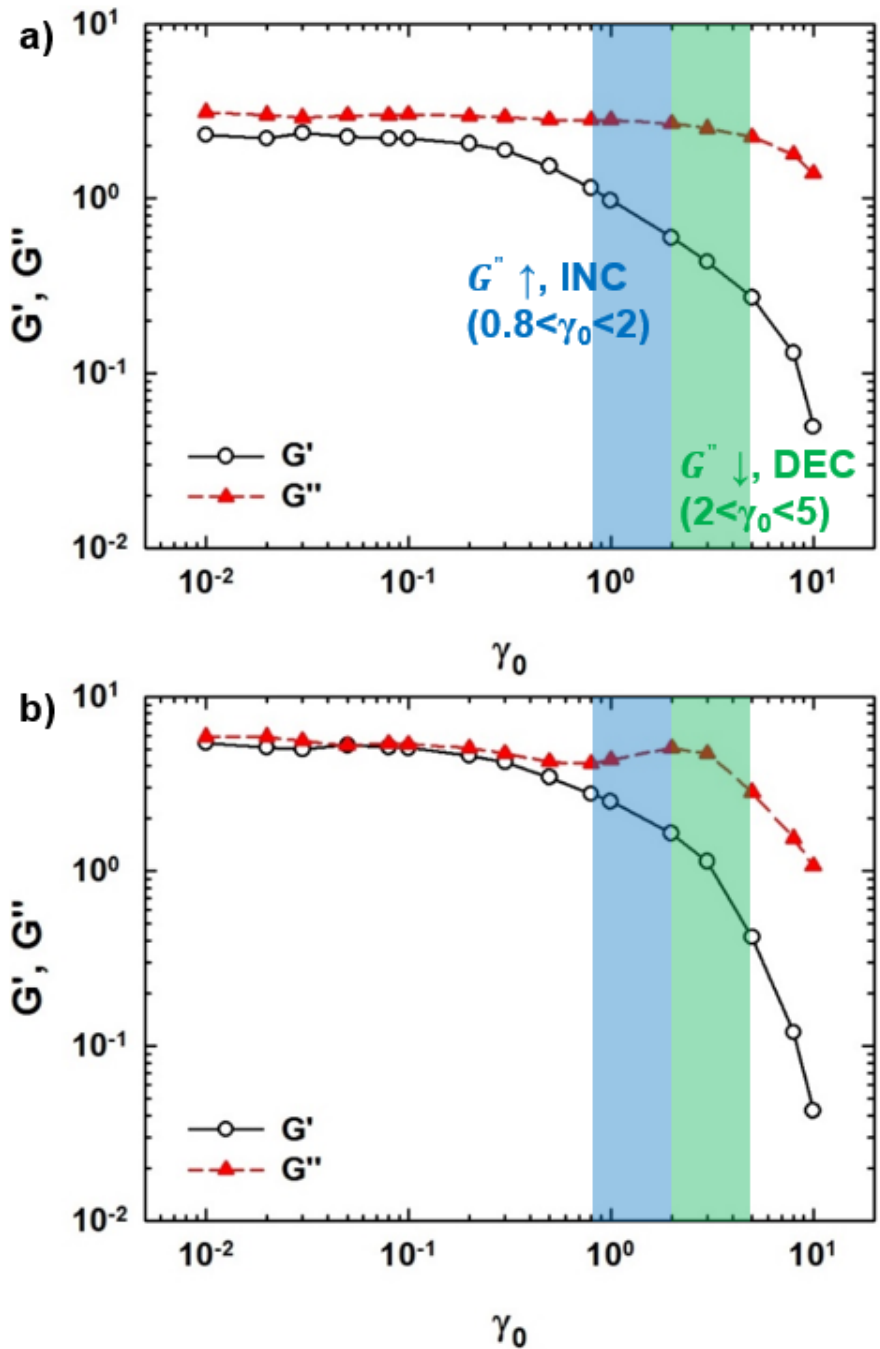


Fig. 4-12 Strain sweep results of a) $De = 20$, b) $De = 80$ for PF at $\Gamma/\Gamma_{freezing} = 0.61$. When $De = 20$, strain thinning is shown, and when $De = 80$ weak strain overshoot is shown.

In Fig. 4-13, results of W_{A1} , W_{B1} , and W_{FR} normalized by W_{full} are plotted as a function of γ_0 at two De. In Fig. 4-14, W_{B2} , W_{A2} , and $W_{A2} + W_{B2}$ are shown. When γ_0 is small (for $De = 20$, $\gamma_0 \leq 0.2$; for $De = 80$, $\gamma_0 \leq 0.3$), results are independent of γ_0 or the change of values is not significant. In this linear regime, W_{FR}/W_{full} is higher when $De = 80$, whose result corresponds with Fig 4-8 a) from Giesekus model. As γ_0 increases, W_{A1} , W_{B1} , and W_{FR} start to decrease while W_{B2} and W_{A2} increase.

It is notable that although the increasing or decreasing tendencies of other terms are similar between two De regardless of γ_0 , those of W_{A1}/W_{full} are totally different in INC regime. At $De = 20$, where overshoot peak does not appear, W_{A1}/W_{full} decreases at an almost same rate in both INC and DEC regimes. On the contrary, at $De = 80$, where overshoot peak appears, W_{A1}/W_{full} increases in INC regime followed by a decrease in DEC regime. It means that there is a possibility for work proportion of section A1 to whole work has an important role in inducing strain overshoot behavior.

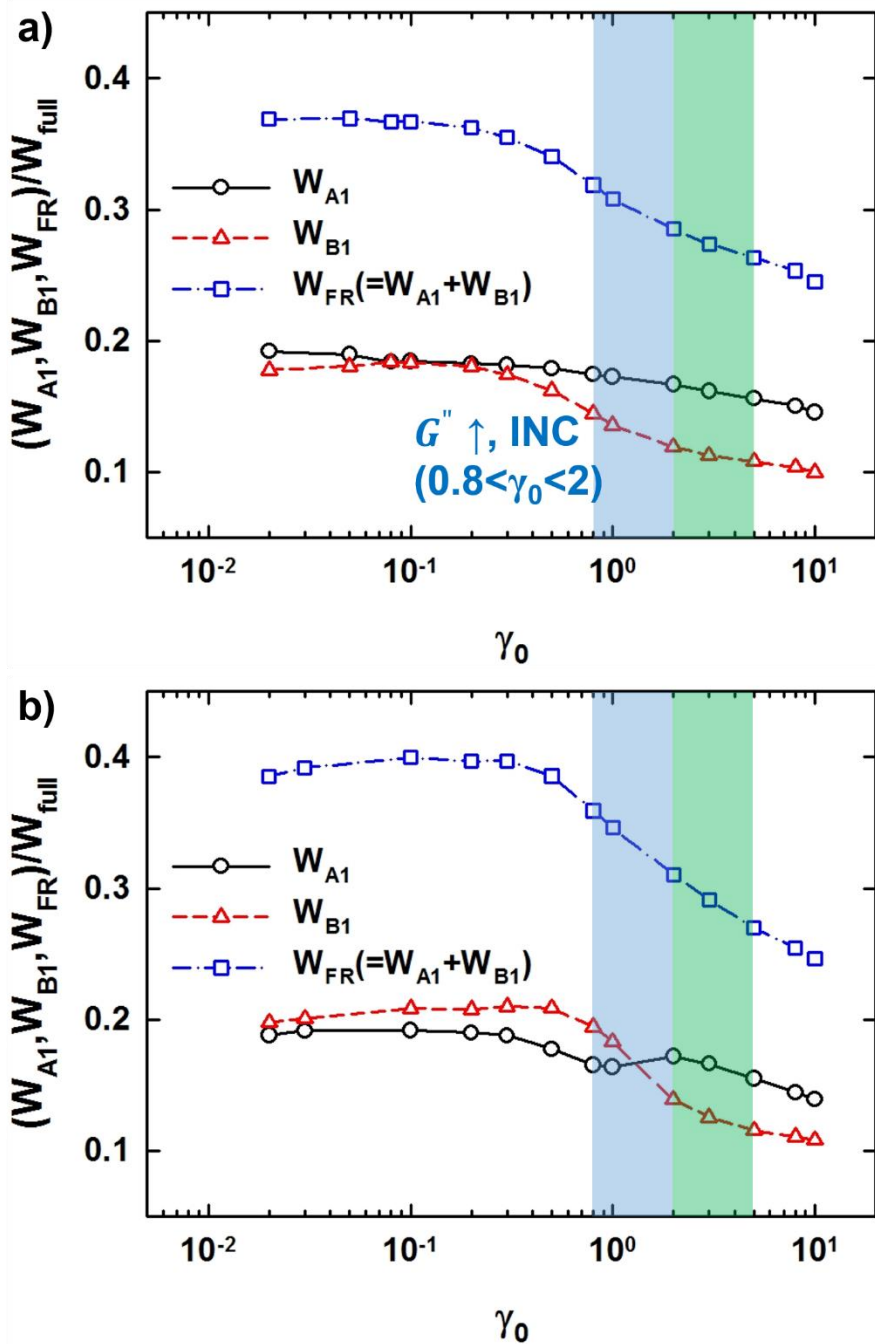


Fig. 4-13 Normalized a) W_{A1} , W_{B1} , and W_{FR} by W_{full} at $De = 20$, b) W_{A1} , W_{B1} , and W_{FR} by W_{full} at $De = 80$ at $De = 80$ as a function of γ_0 for PF at $\Gamma/\Gamma_{freezing} = 0.61$.

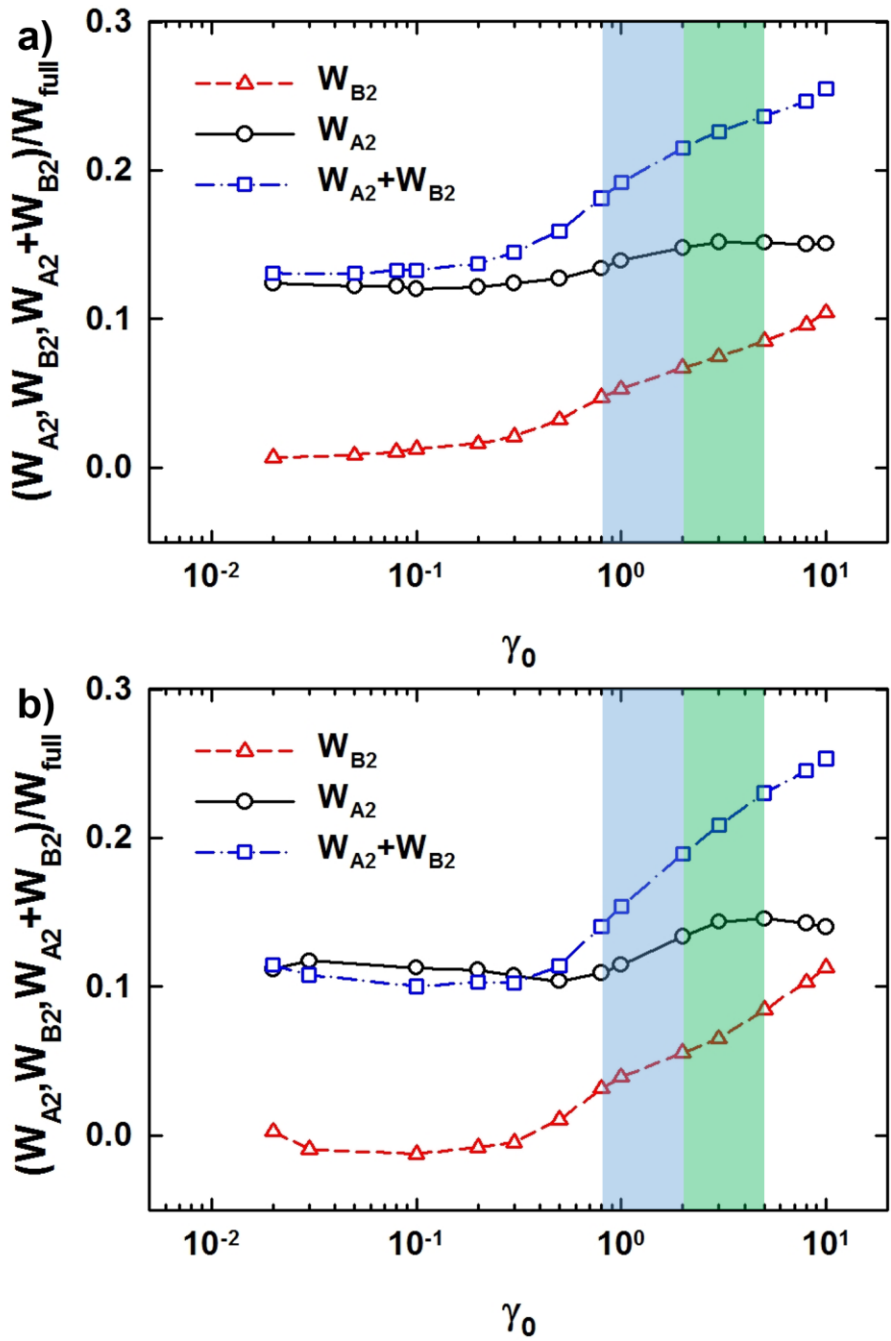


Fig. 4-14 Normalized a) W_{B2} , W_{A2} , and $W_{A2} + W_{B2}$ at $De = 20$, b) W_{B2} , W_{A2} , and $W_{A2} + W_{B2}$ by W_{full} at $De = 80$ as a function of γ_0 for PF at $\Gamma/\Gamma_{freezing} = 0.61$.

For understanding intuitively subdivided W , $x - \sigma$ Lissajous curves of γ_0 ranging from 0.8 to 5 are plotted in Fig. 4.15. All stresses are normalized by their maxima. Area of section A1, which can be interchangeable with W_{A1} , is indicated by red areas. The area of section A1 does not vary much with increasing γ_0 at $De = 20$. In contrast, the area of section A1 increases clearly in INC regime ($0.8 < \gamma_0 < 2$), and it does not vary much in DEC regime ($2 < \gamma_0 < 5$). This results inferred that the trend difference in area change at subsection may be the main factor that makes difference in rheological behavior.

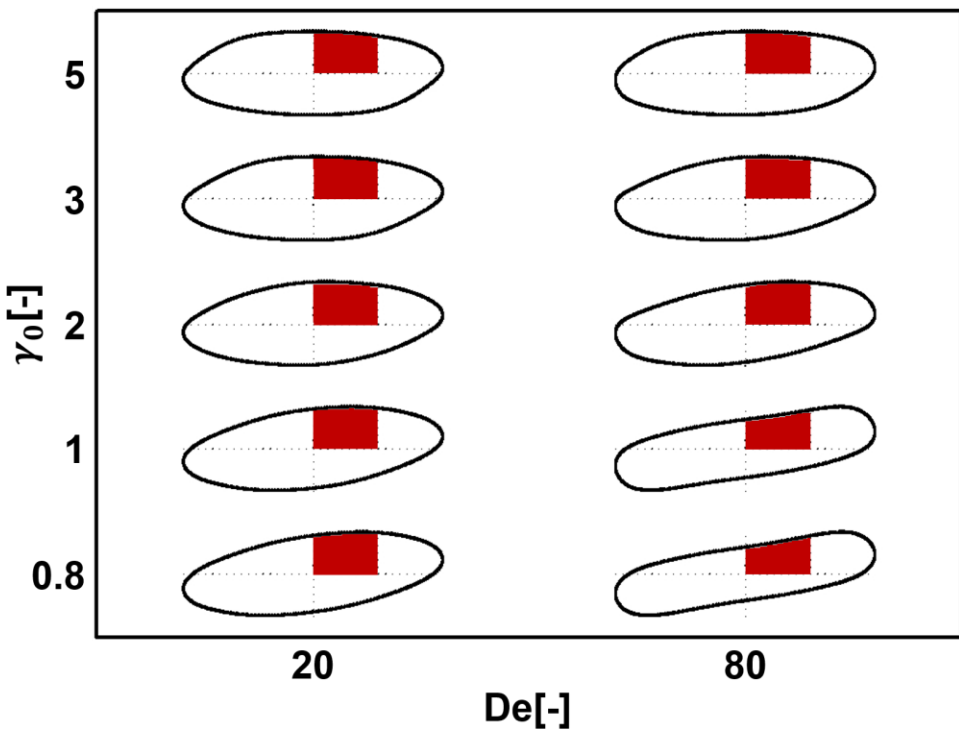


Fig. 4-15 $x - \sigma$ Lissajous curves for PF at $De = 20$ and 80 , $\Gamma/\Gamma_{freezing} = 0.61$. The red section indicates section A1.

To relate work with structure, the average of normalized excess entropy at two De in section A1 is plotted as a function of γ_0 in Fig. 4-16. Excess entropy is normalized by maximum excess entropy in the whole cycle. When this value is high, it means that the extent of particles alignment in section A1 is similar to maximum alignment of the whole cycle.

When $\gamma_0 < 0.8$, the average excess entropy at both De = 20 and 80 decreases, and the decrement is much higher at De = 80. This means that when comparing the maximum ordered state, alignment of particles decreases as γ_0 increases and discrepancy between the structure in section A1 and maximum alignment structure is higher at De = 80.

In INC regime ($0.8 < \gamma_0 < 2$), the maximum structural difference in two De is observed at $\gamma_0 = 2$, and the increment is much higher at De = 80. As γ_0 increases, more aligned structures are formed in section A1 and this realignment is much more significant at De = 80. This structural change makes stress increases in section A1 (Fig. 4-15, De = 80), which leads to overshoot behavior of G'' . However, increments of excess entropy and stress at De = 20 do not stand out, and G'' maintains their value in this regime.

In DEC regime ($2 < \gamma_0 < 5$), the difference in average excess entropy reduced, which leads to similar stress shape in section A1 and the appearance of same rheological behavior at two De (G'' decreases).

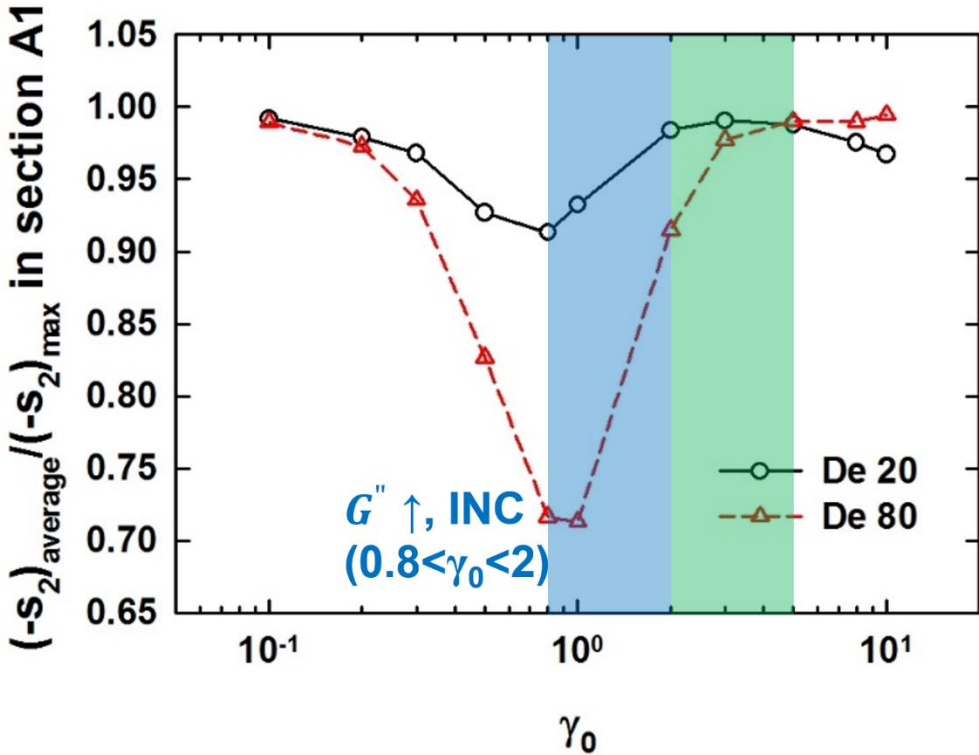


Fig. 4-16 The normalized average excess entropy as a function of γ_0 for PF at $De = 20$ and 80 , $\Gamma/\Gamma_{freezing} = 0.61$.

In this section, tracking W and E method is applied to oscillatory stress from Brownian dynamics simulation. W is analyzed and compared by subdividing them into 4 sections to compare systems with different G'' characteristics. The relationship between the appearance of different rheological behavior and subdivided W is intensively studied. The unusual change in subdivided W corresponds to overshoot of G'' regime is found and the relationship between rheological behavior and stress or particle structure are explained. Through these processes, we expect that this analyzing method could point

out which part of the cycle is energetically important for the appearance of certain rheological behavior.

4.6 Conclusions

Throughout the one full cycle, the inner area of elastic Lissajous ($\gamma - \sigma$), which is related to work (W), has a relevance to the viscous property of a material, whereas the inner area of viscous Lissajous ($\dot{\gamma}/\omega - \sigma$), which is related to stored energy (E), has a relevance to the elastic property of a material. The inner area of Lissajous depends only on δ_1 and σ_1 and it is independent of higher harmonics. In contrast, the effect of higher harmonics is clearly manifested in the path of W or E during the cycle. As the work and stored energy are path dependent, it is necessary to track W and E during the cycle to analyze nonlinear stress properly.

To analyze W and E during the cycle quantitatively, time domain was divided into small regimes, and W and E were calculated in each regime. This approach was applied to perfectly elastic solid, viscous liquid, viscoelastic fluid, and the fluid with yield stress.

For pure materials, W and E always show symmetry with respect to flow reversal. Pure material with different rheological properties can be classified (whether thinning or thickening, softening and stiffening) by investigating the change in W and E in nonlinear regime.

For viscoelastic materials, the extent of asymmetry with respect to FR becomes larger as elastic character becomes more significant in W . The extent of asymmetry in E becomes larger as viscous character grows. W_{FR} and E_{FR} depend only on δ_1 in linear regime. In nonlinear condition, W_{FR} and E_{FR} reflect the ratio of the elastic terms of total stress and the viscous term of fundamental ω , and the ratio of the viscous terms of total stress and the elastic term of fundamental ω , respectively.

For yielding materials, total stress was divided into the elastic and viscous part, and both W and E in each part was obtained separately. Normalized W in the elastic stress part is zero, which corresponds to W of the perfectly elastic solid. However, normalized E in the viscous stress part is larger than that of the elastic stress part, and the meaning of E during the cycle is not clear yet.

For particle simulation, systems with different rheological properties are analyzed and compared by using a concept of work. Normalized W in section A1 increases in the γ_0 regime that shows weak strain overshoot whereas it decreases for regime that shows strain thinning. It means that systems with different rheological properties can be explained by using a concept of energy.

This approach has an advantage in analyzing nonlinear oscillatory shear stress in the perspective of work and energy without mathematically intriguing higher harmonics. The difference in materials with different rheological properties and the extent of elastic/viscous characteristics can be explained in terms of work and energy.

Appendix 4A

Nonlinear oscillatory shear stress in Fourier series form can be expressed as Eq. (1-6). W for this stress from time zero to t can be rearranged as in Eq. (4A-1).

$$W = \frac{\gamma_0 \sigma_1 \omega \sin \delta_1}{2} t + \sum_{n=1}^{\infty} \frac{\gamma_0}{2n} \left[\sigma_{2n-1} \sin(n\omega t + \delta_{2n-1}) + \sigma_{2n+1} \sin(n\omega t + \delta_{2n+1}) \right] \sin n\omega t \quad (4A-1)$$

It is notable that W can be divided into the first term in the right hand side, which increases linearly with time, and the second term which is oscillating. When time is $2\pi/\omega$ (full cycle) or π/ω (half cycle), only the first term in the right hand side remains as $\sin n\omega t$ is always zero, and the effect of higher order terms disappears.

Let arbitrary time point before half cycle be t . W from time zero to t is same as equation (4A-1), and it is denoted as W_t . W from time zero to $t+\frac{\pi}{\omega}$ is given as below.

$$W_{t+\frac{\pi}{\omega}} = \frac{\gamma_0 \sigma_1 \omega \sin \delta_1}{2} t + \frac{\gamma_0 \sigma_1 \sin \delta_1 \pi}{2} + \sum_{n=1}^{\infty} \frac{\gamma_0}{2n} \left[\sigma_{2n-1} \sin(n\omega t + \delta_{2n-1}) + \sigma_{2n+1} \sin(n\omega t + \delta_{2n+1}) \right] \sin n\omega t \quad (4A-2)$$

Then,

$$\frac{W_{t+\frac{\pi}{\omega}} - W_t}{W_{\text{full}}} = 0.5 \quad (4A-3)$$

As the work after half cycle is the same as the one before half cycle plus

0.5, it is always enough to investigate the work before half cycle.

The ratio of W until first flow reversal (W_{FR}) and W throughout one full cycle (W_{full}) is given as below:

$$\begin{aligned}\frac{W_{FR}}{W_{full}} &= \frac{1}{4} + \frac{1}{6\sigma_1 \sin \delta_1 \pi} \left(3\sigma_1 \cos \delta_1 + 3\sigma_3 \cos \delta_3 + \dots \right) \\ &= \frac{1}{4} + \frac{1}{2 \tan \delta_1 \pi} + \frac{1}{2\sigma_1 \sin \delta_1 \pi} \left(\sigma_3 \cos \delta_3 + \frac{\sigma_5}{3} \cos \delta_5 + \dots \right) \quad (4A-4)\end{aligned}$$

If there is no contribution of higher order terms, W_{FR}/W_{full} is always larger than 0.25 as $\tan \delta_1$ is always positive. As normalized W until the half cycle is 0.5, the work before flow reversal is larger than the work after flow reversal in linear viscoelastic limit. When $\tan \delta_1$ is small, which means the material is nearly elastic, W_{FR}/W_{full} can be large. This result indicates that W_{FR}/W_{full} is affected by the elastic contribution too even though W throughout one full cycle is related only to the viscous characteristic. When there exist higher order contributions, W_{FR}/W_{full} is related to $\cos \delta_n$ except the first term (1/4). By checking how much W_{FR}/W_{full} deviate from 0.25, the ratio of the elastic contribution in the total stress and viscous contribution of the first harmonic can be understood.

Similarly,

$$E = \frac{\gamma_0 \sigma_1 \omega \cos \delta_1}{2} t - \sum_{n=1}^{\infty} \frac{\gamma_0}{2n} \left[\begin{array}{l} \sigma_{2n-1} \cos(n\omega t + \delta_{2n-1}) \\ -\sigma_{2n+1} \cos(n\omega t + \delta_{2n+1}) \end{array} \right] \sin n\omega t \quad (4A-5)$$

$$E_{t+\frac{\pi}{\omega}} = \frac{\gamma_0 \sigma_1 \omega \cos \delta_1}{2} t + \frac{\gamma_0 \sigma_1 \cos \delta_1 \pi}{2} - \sum_{n=1}^{\infty} \frac{\gamma_0}{2n} \begin{bmatrix} \sigma_{2n-1} \cos(n\omega t + \delta_{2n-1}) \\ -\sigma_{2n+1} \cos(n\omega t + \delta_{2n+1}) \end{bmatrix} \sin n\omega t \quad (4A-6)$$

$$\frac{E_{t+\frac{\pi}{\omega}} - E_t}{E_{full}} = 0.5 \quad (4A-7)$$

$$\begin{aligned} \frac{E_{FR}}{E_{full}} &= \frac{1}{4} + \frac{1}{6\sigma_1 \cos \delta_1 \pi} \begin{pmatrix} 3\sigma_1 \sin \delta_1 - 3\sigma_3 \sin \delta_3 \\ +\sigma_5 \sin \delta_5 - \sigma_7 \sin \delta_7 + \dots \end{pmatrix} \\ &= \frac{1}{4} + \frac{\tan \delta_1}{2\pi} + \frac{1}{2\sigma_1 \cos \delta_1 \pi} \begin{pmatrix} -\sigma_3 \sin \delta_3 + \frac{\sigma_5}{3} \sin \delta_5 \\ -\frac{\sigma_7}{3} \sin \delta_7 + \dots \end{pmatrix} \end{aligned} \quad (4A-8)$$

When there is no contribution of higher order terms, E_{FR}/E_{full} is always larger than 0.25, which means that E before flow reversal is larger than E after flow reversal in linear viscoelastic limit. When $\tan \delta_1$ is large, which means the material is nearly viscous, E_{FR}/E_{full} can be large as well. This result indicates that E_{FR}/E_{full} is affected by the viscous contribution too even though E throughout one full cycle is related only to the elastic characteristic. When there exist higher order contributions, E_{FR}/E_{full} is related to $\cos \delta_n$ except the first term (1/4). By checking how much E_{FR}/E_{full} deviate from 0.25, the ratio of the viscous characteristic in total stress and the elastic characteristic of the first harmonic can be understood.

V. Conclusions

This thesis deals with analysis methods for nonlinear shear stress under large amplitude oscillatory shear (LAOS) flow. Although LAOS is widely used and there exist a few analysis methods for LAOS, their interpretation or physical meaning was not fully understood. For stress decomposition, which analyzes stress in the strain or strain rate domain, the validity of this method is not clear. For Fourier transform (FT), which analyzes stress in the time domain, physical meaning of calculated parameters are questioned. Thus, this thesis intensively studies the methods for analyzing nonlinear oscillatory shear stress to interpret and understand them properly.

In chapter 3, stress decomposition method was analyzed intensively. This method was applied to oscillatory stresses of hard and soft sphere systems, which are obtained by particle dynamics simulations. Double peaks, which are experimentally observed only in the elastic stress of hard sphere systems, were also observed only in the hard sphere systems in the simulation. To find out the structural origin of double peaks, the structure of the particulate system was analyzed in terms of the softness of the particles and strain amplitude, which determine the presence of double peaks. As previously reported, relating elastic stress and structure one-by-one at each time was difficult. Rather, by considering the structure and stress of the whole cycle, the structural origin of double peaks could be suggested. Double peaks were

observed in systems where the structural difference between maximum ordered state and minimum ordered state of the whole cycle was large. In this chapter, the new interpretation method of stress decomposition, which uses symmetric characteristic, was suggested.

In chapter 4, a new method for analyzing oscillatory shear stress was suggested. For this purpose, the concept of work and stored energy, which has rarely been considered in the past, was adopted. Especially, work and stored energy during the cycle, not at the end of one full cycle, were concentrated in this new method. To analyze oscillatory shear stress quantitatively, the whole cycle was divided into several sections, and the work or stored energy of subdivided sections was calculated separately. From the work and stored energy of model nonlinear stress, it was proved that such a tracking is important for analyzing nonlinear stress properly. By applying this method to various constitutive equations and from the results of Brownian dynamics simulation, work and stored energy could be correlated with rheological property, oscillatory stress, and particle structure. By these approaches, a possibility was shown that the systems with different rheological behavior could be characterized by energy during the cycle. In this chapter, a new analyzing method which uses energy concept was suggested.

Analysis of nonlinear oscillatory shear stress is still not fully understood. This thesis provides a new insight on the analysis of nonlinear oscillatory shear stress in the perspective of symmetry (chapter 3) and energy (chapter

4). This study establishes a stepping stone for further understanding of the nonlinear oscillatory shear stress in the perspective of symmetry and energy.

Bibliography

In alphabetical order by first author,

Agrawal R, Kofke DA (1995) Thermodynamic and structural properties of model systems at solid-fluid coexistence I . Fcc and bcc soft spheres. Mol

Phys 85:23-42

Ahirwal D, Filipe S, Neuhaus I, Busch M, Schlatter G, Wilhelm M (2014) Large amplitude oscillatory shear and uniaxial extensional rheology of blends from linear and long-chain branched polyethylene and polypropylene. J Rheol 58:635-658

Besseling TH, Hermes M, Fortini A, Dijkstra M, Imhof A, van Blaaderen A (2012) Oscillatory shear-induced 3D crystalline order in colloidal hard-sphere fluids. Soft Matter 8:6931-6939

Bird RB, Armstrong RC, Hassager O (1987) Dynamics of polymeric liquids: volume 1 fluid mechanics. Wiley, New York

Braňka AC, Heyes DM (2006) Thermodynamic properties of inverse power fluids. Phys Rev E 74:1-11

Cho KS, Hyun K, Ahn KH, Lee SJ (2005) A geometrical interpretation of large amplitude oscillatory shear response. J Rheol 49:747-758

- Dealy JM, Wissbrun KF (1990) Melt rheology and its role in plastic processing: theory and applications. Van Nostrand Reinhold, New York
- Ding Y, Mittal J (2015) Equilibrium and nonequilibrium dynamics of soft sphere fluids. *Soft Matter* 11:5274-5281
- Dzugutov M (2006) A universal scaling law for atomic diffusion in condensed matter. *Nat* 381:137-139
- Ewoldt RH, Hosoi AE, McKinley GH (2008) New measures for characterizing nonlinear viscoelasticity in large amplitude oscillatory shear. *J Rheol* 52:1427-1458
- Ewoldt RH, Bharadwaj NA (2013) Low-dimensional intrinsic material functions for nonlinear viscoelasticity. *Rheol Acta* 52:201-219
- Foss DR, Brady JF (2000a) Brownian dynamics simulation of hard-sphere colloidal dispersions. *J Rheol* 44:629-651
- Foss DR, Brady JF (2000b) Structure, diffusion and rheology of Brownian suspensions by Stokesian dynamics simulation. *J Fluid Mech* 407:167-200
- Fuchs M, Ballauff M (2005) Flow curves of dense colloidal dispersions: Schematic model analysis of the shear-dependent viscosity near the colloidal glass transition. *J Chem Phys* 122:1-6
- Ganeriwala SN, Rotz CA (1987) Fourier transform mechanical analysis for determining the nonlinear viscoelastic properties of polymers. *Polym Eng Sci* 27:165-178

Giacomin AJ, Dealy JM (1993) Large amplitude oscillatory shear. Chapman & Hall, London

Giacomin AJ, Bird RB, Aumnate C, Mertz AM, Schmalzer AM, Mix AW (2012) Viscous heating in large-amplitude oscillatory shear flow. *Phy Fluids* 24:1-33

Giacomin AJ, Bird RB, Baek HM (2013) Temperature rise in large-amplitude oscillatory shear flow from shear stress measurements. *Ind Eng Chem Res* 52:2008-2017

Gompper G, Ihle T, Kroll DM, Winkler RG (2009) Multi-particle collision dynamics: A particle-based mesoscale simulation approach to the hydrodynamics of complex fluids. *Adv Polym Sci* 221:1-87

Goudoulas TB, Germann N (2017) Phase transition kinetics and rheology of gelatin-alginate mixtures. *Food Hydrocoll* 66:49-60

Grand AL, Petekidis G (2008) Effects of particle softness on the rheology and yielding of colloidal glasses. *Rheol Acta* 47:579-590

Heyes DM, Melrose JR (1993) Brownian dynamics simulations of model hard-sphere suspensions. *J Non-Newton Fluid Mech* 46:1-28

Heyes DM, Brańka AC (2005) Mechanical, rheological and transport properties of soft particle fluids. *Mol Simul* 31:945-959

Heyes DM, Brańka AC (2008) Self-diffusion coefficients and shear viscosity of inverse power fluids: from hard- to soft-spheres. *Phys Chem Chem Phys* 10:4036-4044

Huang G, Zhang H, Liu Y, Chang H, Zhang H, Song H, Xu D, Shi T (2017) Strain hardening behavior of Poly(vinyl alcohol)/borate hydrogels. *Macromol* 50:2124-2135

Hyun K, Kim SH, Ahn KH, Lee SJ (2002) Large amplitude oscillatory shear as a way to classify the complex fluids. *J Non-Newtonian Fluid Mech* 107: 51-65

Hyun K, Nam JG, Wilhelm M, Ahn KH, Lee SJ (2003) Nonlinear response of complex fluids under LAOS (large amplitude oscillatory shear) flow. *Korea-Aust Rheol J* 15:97-105

Hyun K, Nam JG, Wilhelm M, Ahn KH, Lee SJ (2006) Large amplitude oscillatory shear behavior of PEO-PPO-PEO triblock copolymer solutions. *Rheol Acta* 45:239-249

Hyun K, Wilhelm M (2009) Establishing a new mechanical nonlinear coefficient Q from FT-rheology: First investigation of entangled linear and comb polymer model systems. *Macromol* 42:411-422

Hyun K, Wilhelm M, Klein CO, Cho KS, Nam JG, Ahn KH, Lee SJ, Ewoldt RH, McKinley GH (2011) A review of nonlinear oscillatory shear tests: Analysis and application of large amplitude oscillatory shear (LAOS). *Prog Polym Sci* 36:1697-1753

Khandavalli S, Hendricks J, Clasen C, Rothstein JP (2016) A comparison of linear and branched wormlike micelles using large amplitude oscillatory shear and orthogonal superposition rheology. *J Rheol* 60:1331-1346

Koumakis N, Brady JF, Petekidis G (2013) Complex oscillatory yielding of model hard-sphere glasses. *Phys Rev Lett* 110:1-5

Koumakis N, Brady JF, Petekidis G (2016) Amorphous and ordered states of concentrated hard spheres under oscillatory shear. *J Non-Newton Fluid Mech* 233:119-132

Koumakis N, Pamvouxoglou A, Poulos AS, Petekidis G (2012) Direct comparison of the rheology of model hard and soft particle glasses. *Soft Matter* 8:4271-4284

Lange E, Caballero JB, Puertas AM, Fuchs M (2009) Comparison of structure and transport properties of concentrated hard and soft sphere fluids. *J Chem Phys* 130:1-8

Larson RG (1999) The structure and rheology of complex fluids. Oxford University Press, New York

Lee SH, Song HY, Hyun K, Lee JH (2015) Nonlinearity from FT-rheology for liquid crystal 8CB under large amplitude oscillatory shear (LAOS) flow. *J Rheol* 59:1-19.

Lee YK, Nam J, Hyun K, Ahn KH, Lee SJ (2015) Rheology and microstructure of non-Brownian suspensions in the liquid and crystal coexistence region: Strain stiffening in large amplitude oscillatory shear. Soft Matter 11:4061-4074

Lees AW, Edwards SF (1972) The computer study of transport processes under extreme conditions. J Phys C: Solid State Phys 5:1921-1928

Lin NYC, Goyal S, Cheng X, Zia RN, Escobedo FA, Cohen I (2013) Far-from-equilibrium sheared colloidal liquids: Disentangling relaxation, advection, and shear-induced diffusion. Phys Rev E 88:1-10

Mason TG, Weitz DA (1995) Elasticity of compressed emulsions. Phys Rev Letter 75:2051-2054

Mason TG, Lacasse M-D, Grest GS, Levine D, Bibette J, Weitz DA (1997) Osmotic pressure and viscoelastic shear moduli of concentrated emulsions. Phys Rev E 56:3150-3166

Matsumoto T, Segawa Y, Warashina Y, Onogi S (1973) Nonlinear behavior of viscoelastic materials. II. The method of analysis and temperature dependence of nonlinear viscoelastic functions. Trans Soc Rheol 17:47-62

McMullan JM, Wagner NJ (2009) Directed self-assembly of suspensions by large amplitude oscillatory shear flow. J Rheol 53:575-588

Mermet-Guyennet MRB, Gianfelice De Castro J, Habibi M, Martzel N, Denn MM, Bonn D (2015) LAOS: The strain softening/strain hardening paradox. *J Rheol* 59:21-32

Mitchell PJ, Heyes DM, Melrose JR (1995) Brownian-dynamics simulations of model stabilized colloidal dispersions under shear. *J Chem Soc, Faraday Trans* 91:1975-1989

Nam JG, Ahn KH, Lee SJ, Hyun K (2011) Strain stiffening of non-colloidal hard sphere suspensions dispersed in Newtonian fluid near liquid-and-crystal coexistence region. *Rheol Acta* 50:925-936

Nazockdast E, Morris JF (2012) Effect of repulsive interactions on structure and rheology of sheared colloidal dispersions. *Soft Matter* 8:4223-4234

Neidhöfer T, Wilhelm M, Debbaut B (2003) Fourier-transform rheology experiments and finite-element simulations on linear polystyrene solutions. *J Rheol* 47:1351-1371

Park JD, Ahn KH, Lee SJ (2015) Structural change and dynamics of colloidal gels under oscillatory shear flow. *Soft Matter* 11:9262-9272

Pearson DS, Rochefort WE (1982) Behavior of concentrated polystyrene solutions in large-amplitude oscillating shear fields. *J Polym Sci Part A-2 Polym Phys* 20:83-98

Petekidis G, Vlassopoulos D, Pusey PN (2003) Yielding and flow of colloidal glasses. *Faraday Discuss* 123:287-302

Pieprzyk S, Heyes DM, Bran'ka AC (2014) Thermodynamic properties and entropy scaling law for diffusivity in soft spheres. *Phys Rev E* 90:1-16

Poulos AS, Stellbrink J, Petekidis G (2013) Flow of concentrated solutions of starlike micelles under large-amplitude oscillatory shear. *Rheol Acta* 52:785-800

Poulos AS, Renou F, Jacob AR, Koumakis N, Petekidis G (2015) Large amplitude oscillatory shear (LAOS) in model colloidal suspensions and glasses: frequency dependence. *Rheol Acta* 54:715-724

Ptaszek P (2015) A geometrical interpretation of large amplitude oscillatory shear (LAOS) in application to fresh food foams. *J Food Eng* 146:53-61

Rogers SA, Lettinga MP (2012) A sequence of physical processes determined and quantified in large-amplitude oscillatory shear (LAOS): Application to theoretical nonlinear models. *J Rheol* 56:1-25

Salehiyan R, Song HY, Hyun K (2015) Nonlinear behavior of PP/PS blends with and without clay under large amplitude oscillatory shear (LAOS) flow. *Korea Aust Rheol J* 27:95-103

Senff H, Richtering W (1999) Rheology of a temperature sensitive core-shell latex. *Langmuir* 15:102-106

Siebenbürger M, Fuchs M, Winter H, Ballauff M (2009) Viscoelasticity and shear flow of concentrated, noncrystallizing colloidal suspensions: Comparison with mode-coupling theory. *J Rheol* 53:707-726

Sim HG, Ahn KH, Lee SJ (2003) Large amplitude oscillatory shear behavior of complex fluids investigated by a network model: a guideline for classification. *J Non-Newtonian Fluid Mech* 112:237-250

Truskett TM, Torquato S, Debenedetti PG (2000) Towards a quantification of disorder in materials: Distinguishing equilibrium and glassy sphere packings. *Phys Rev E* 62:993-1001

Wang G, Swan JW (2016) Large amplitude oscillatory shear of hard-sphere colloidal dispersions: Brownian dynamics simulation and Fourier-transform rheology. *J Rheol* 60:1041-1053

Wilhelm M, Maring D, Spiess HW (1998) Fourier-transform rheology. *Rheol Acta* 37:399-405

Wilhelm M, Reinheimer P, Ortseifer M (1999) High sensitivity Fourier-transform rheology. *Rheol Acta* 38:349-356

Wilhelm M (2002) Fourier-transform rheology. *Macromol Mater Eng* 287:83-105

Yoshimura AS, Prud'homme RK (1987) Response of an elastic Bingham fluid to oscillatory shear. *Rheol Acta* 26:428-436

국문 초록

대변형 진동 전단 유동 실험은 복잡 유체의 특성을 알아보기 위해 널리 적용된다. 대변형 진동 전단 유동 조건에서의 응력을 분석하기 위하여 시간 축이나 변형률과 변형률 속도 축으로 분석하는 방법이 많이 제시되어 있으나 이들의 해석 방법이나, 물리적 의미는 완전히 이해되어 있지는 않다. 예를 들어, 분석 방법 중 하나인 응력 분해 법은 응력과 구조 특성의 불일치성 때문에 아직 논쟁 중에 있다. 이 학위 논문의 목적 중 하나는, 응력 분해 법의 적절한 해석 방안을 모색하는 것이다.

응력 분해 법은 진동 유동의 수학적인 대칭성을 이용하여 전체 진동 응력을 탄성과 점성 응력으로 나누어서 분석하는 방법이다. 이 학위 논문에서는 응력 분해 법을 구형 강체와 구형 연체를 모사하는 브라운 동역학 시뮬레이션을 통하여 얻은 진동 전단 응력에 적용하였다. 구형 강체를 사용한 실험에서만 나타나는 탄성 응력에서의 이중 피크는 시뮬레이션에서도 구형 강체를 모사할 때만 나타나게 된다.

이중 피크의 구조적 원인을 살펴보기 위하여, 이중 피크 생성 유무가 다르도록 입자의 강도와 변형률의 크기를 바꾼 입자계들의 구조를 서로 비교 분석하였다. 구형 강체와 구형 연체를 비교하였을 때, 두 시스템은

크게 다른 구조를 보인다. 반면, 구형 강체의 경우에는 구조와 탄성 응력은 서로 일대일 대응이 되지 않는다. 심도 있는 분석을 통하여 구조와 탄성 응력을 서로 연관시키기 위해서는 각 시점에서의 둘을 연관 짓기 보다는 하나의 전체 사이클 하에서 둘을 연관 지어야 함을 알 수 있었다. 그리고 시뮬레이션 상에서 이중 피크를 생성시키는 구조적 특성을 제시해 보았다.

이 학위 논문의 또 다른 목적은 진동 전단 유동을 분석하는 새로운 방법을 제시해 보는 것이다. 이 목적을 이루기 위하여, 이전에는 많이 고려되지 않았던 일과 저장 에너지의 개념을 적용하였다. 하나의 사이클에 대한 변형률-응력 Lissajous 곡선의 내부 넓이는 일 또는 물질의 점성 특성과 관련되어 있으며, 변형률 속도-응력 Lissajous 곡선의 내부 넓이는 저장 에너지 또는 물질의 탄성 능력과 관련되어 있음을 이미 알려져 있다. 이러한 관계는 비선형 응력에서도 만족을 하며, 그에 따라 지금까지는 하나의 사이클에 대한 Lissajous 곡선의 내부 넓이만 관심을 받았다.

하지만 비선형 응력을 정확히 분석하기 위해서는 한 사이클 전체에서의 일과 에너지뿐만 아니라 사이클 도중의 일과 에너지를 고려해야 하므로, 진동 유동 중의 일과 에너지를 다양한 시스템에 대하여 추적해 보았다. 첫 번째로, 이 개념을 서로 다른 유변학적 거동을 보이는 완전 탄성 고체와 순수 점성 액체에 적용해 보았다. 이들 유체는 전체 사이클을

여러 개의 부분으로 나눈 영역에서의 일과 에너지의 변화를 살펴봄으로써 서로 구분할 수 있었다. 이 개념을 점탄성 유체와 Bingham 유체에도 적용하였다. 이러한 유체에서는 유동의 방향이 바뀌는 지점을 기준으로 나타나는 일과 에너지의 대칭성이 나타나지 않는다. 따라서 이런 유체에서는 비대칭성의 정도를 고려해야 한다. 브라운 동역학 시뮬레이션을 통해 얻은 진동 응력에도 동일한 방법을 이용하여 분석해 보았다. 이 분석에서 일은 유변학적 특성, 진동 응력, 그리고 구조와 연관 지을 수 있었다. 이러한 분석들을 통해서 서로 다른 유변학적인 특성을 보이는 시스템을 사이를 도중의 일과 에너지를 이용하여 분석할 수 있다는 가능성을 보였다.

이 학위 논문은 비선형 진동 전단 응력을 분석하는데 새로운 통찰력을 제시하는 것이다. 이 연구는 대칭성과 에너지의 관점으로 비선형 진동 전단 응력을 더 깊이 이해하는데 확장 가능한 기반을 마련했다는 점에서 의미 있는 연구라 할 수 있다.

주요어: 대변형 진동 전단 유동, 구형 강체, 구형 연체, 브라운 동역학 시뮬레이션, 응력 분해 법, 일, 저장 에너지

학번: 2010-20993